Nanostructured Thin Films Prepared by Planetary Ball Milling: Fabrication, Characterization and Applications

by

Raju Sapkota
B.Eng. (Hons)., De Montfort University, Leicester, England. 2012
M.Sc., De Montfort University, Leicester, England. 2014

A Dissertation Submitted in Partial Fulfillment
of the Requirements for the Degree of

DOCTOR OF PHILOSOPHY

in the Department of Electrical and Computer Engineering

University of Victoria

Supervisory Committee

Nanostructured Thin Films Prepared by Planetary Ball Milling: Fabrication, Characterization and Applications

by

Raju Sapkota

B.Eng. (Hons)., De Montfort University, Leicester, England. 2012

M.Sc., De Montfort University, Leicester, England. 2014

Supervisory Committee

Dr. Christo Papadopoulos, (Department of Electrical and Computer Engineering)

Supervisor

Dr. Tao Lu, (Department of Electrical and Computer Engineering)

Departmental Member

Dr. Alexandre G. Brolo, (Department of Chemistry)

Outside Member

Abstract

Supervisory Committee

Dr. Christo Papadopoulos, (Department of Electrical and Computer Engineering)

Supervisor

Dr. Tao Lu, (Department of Electrical and Computer Engineering)

Departmental Member

Dr. Alexandre G. Brolo, (Department of Chemistry)

Outside Member

Planetary ball milling (PBM) is a well-known technique for efficient size reduction and homogenization of materials that has been used for many decades in various engineering and industrial processes. More recently, it has emerged as a unique top-down nanofabrication approach for nanomaterials based on nanoscale grinding. However, its potential application in nanostructured thin film fabrication has not been fully explored, as only a limited number of studies have been carried out. In this work, the effects of different grinding parameters (speed, time and solvents) were used to create previously unstudied nanoscale grinding conditions for nanostructured thin film materials via PBM with distinct and novel properties: Nanoparticles of silicon, titanium disilicide ($TiSi_2$) and zinc oxide (ZnO) ground in different solvents (deionized (DI) water/ ethylene glycol (EG)/isopropyl alcohol) resulted in colloidal suspensions (or nanoinks) that could be used to coat various substrates (wafers, glass, flexible substrates, etc.) via drop casting, doctor blading or dip coating. Thin film properties such as wettability, electrical conductivity and gas sensing behavior are studied. The fabricated thin film coating properties could be tuned depending on the combination of starting powder materials, grinding parameters and resulting nanoparticle size/geometry: The influence of surface chemistry, solvent type, particle geometry, surface roughness and defects was shown to alter the conductivity and surface wettability of the resultant films. Thus, thin films formed using PBM nanoinks allow varied and tunable properties for advanced multi-functional coatings and devices.

To demonstrate the feasibility of PBM nanoinks for thin film device applications, ZnO nanoinks were used to create chemiresistive gas sensors that operate at room temperature. By varying grinding parameters (speed, time and solvent) thin film sensors with differing particle sizes and porosity were produced and tested with air/oxygen against hydrogen, argon and methane target gas species, in addition to relative humidity. Grinding speeds of up to 1000 rpm produced particle sizes and RMS thin film roughness below 100 nm, as measured by atomic force microscopy and scanning electron microscopy. Raman spectroscopy, photoluminescence and x-ray analysis confirmed the purity and structure of resulting films. The peak gas sensor response was found for grinding parameters of 400 rpm (average particle size 275 nm) and 30 minutes (average particle size 225 nm) in EG and DI water, respectively, which could be correlated to an increased film porosity and an enhanced electron concentration resulting from adsorption/desorption of oxygen ions on the surface of ZnO nanoparticles. Similarly, gas response and dynamic behavior were found to improve as the operating temperature was increased between 100 and 150 ˚C. These results demonstrate the use of low-cost PBM nanoinks to optimize the active materials for solution-processed thin film gas/humidity sensors that can operate at room temperature for use in environmental, medical, food packaging, laboratory, and industrial applications.

Overall, the nanogrinding technique can produce large amounts of nanoparticle suspension with variable particle sizes for creating thin films with tunable properties. By adjusting grinding parameters, the nanoparticle shape/size and properties can be varied resulting in nanoparticle inks for inexpensive coatings on various substrates and for use in different applications.

Table of Contents

Chapter 1

Chapter 2

Chapter 3

Chapter 4

Chapter 5

List of Tables

List of Figures

List of Symbols

0D	Zero-dimensional
1D	One-dimensional
2D	Two-dimensional
3D	Three-dimensional
AAO	Anodic aluminum oxide
AFM	Atomic force microscope
BPB	Bromophenol dye
CA	Contact angle
CMOS	Complementary metal-oxide semiconductor
CNTs	Carbon nanotubes
CPU	Central processing unit
CVD	Chemical vapor deposition
DC	Direct current
DFT	Density-functional theory
DI	Deionized water
DOS	Density of states
DSA	Directed self-assembly
EBL	Electron-beam lithography
EDX	Energy-dispersive X-ray
EG	Ethylene glycol
FD-SOI	Fully depleted silicon on insulator
FET	Field effect transistor
FIBL	Focused ion beam lithography
GPU	Graphic processing unit
HEBM	High energy ball milling
IBM	International Business Machine

ICs	Integrated circuits
ITO	Indium tin oxide
LIB	Lithium-ion batteries
LOD	Limit of detection
MEMS	Micro-electromechanical systems
MB	Methylene blue
MFC	Mass flow controller
MOS	Metal-oxide-semiconductor
MOSFET	Metal-oxide-semiconductor field effect transistor
NGL	Next-generation lithography
NS	Nanostructure
NT	Nanotubes
NW	Nanowires
PBM	Planetary ball milling
PL	Photoluminescence
PVD	Physical vapor deposition
QD	Quantum dot
RFID	Radio-frequency identification
RH	Relative humidity
RMS	Root mean square
RRAM	Resistive random-access memory
RTDs	Resonant tunneling devices
SAM	Self-assembled monolayer
SCEs	Short channel effects
SCS	Semiconductor characterization system
SEM	Scanning electron microscope
SETs	Single electron transistors
SMU	Source measure unit

STM	Stunning tunneling microscope
TFT	Thin film transistor
TMDCs	Transition-metal dichalcogenides
UV	Ultraviolet light
VLSI	Very large-scale integration

Acknowledgements

I would like to express my gratitude to my supervisor Dr. Chris Papadopoulos for his guidance and support throughout this work. I am grateful to him for giving an opportunity to work in the nanofabrication research lab. This research would not have been possible without his constant suggestions and discussions.

I would like to greatly thank my dissertation committee: Dr. Tao Lu and Dr. Alexandre. G. Brolo for devoting their valuable time and expertise in reviewing the dissertation and giving me valuable advice.

I would also like to thank all my research colleagues (Anusha, Sahil, Tanay and Max) and friends for ensuring me to work in very pleasant and comfortable environment.

Above all, I am also grateful to Sita (my wife), Saurav and Sulav (my sons), my sisters and my in-laws for their patience and support. Thank you to everyone for constant encouragement during my research tenure.

Dedication

To the soul of my late Parents; **Mani Ratna Jaishi** (Father) and **Deu Rupa Jaishi** (Mother). I pray “***33 Koti Devata***” to look after their departed soul. “***May the soul achieve Moksha***”.

Chapter 1

1. Introduction and Background

1.1. Motivation

The extensive development of electronic devices and their usages after the 20th century has drastically changed our world. These electronic technologies, such as computers, telecommunications, cell phones, memory devices and tablets, have simplified modern life across the globe. This section will discuss some of the remarkable breakthroughs of the electronics evolution on device performance and miniaturization. Also, obstacles that occur during the device miniaturization process and their effect on the device performance will be discussed. The chapter will explain the necessity of new techniques, materials and approaches for fabricating future devices, such as integrated circuits (ICs), transistors, memory devices and sensors.

After the invention of two-element vacuum tube, vacuum triode and first solid-state transistors, electronic device fabrication took an astonishing pace [1,2]. However, problems with their macroscopic size, reliability and electrical power consumption are drawbacks of those devices. Later, a monolithic 2D (two-dimensional) integrated circuit was discovered, where all the circuit components were electrically connected on single piece of semiconductor and yielded a practical and reliable method of manufacturing Jack Kilby's and Robert Noyce's integrated circuits [3,4].

Subsequent IC device miniaturization led to rapid innovation after the introduction of Moore's Law in 1965 [5]. According to this observational law [5], the transistor numbers on an integrated circuit approximately double every two years with a corresponding reduction in cost **(*Figure 1. 1*)**

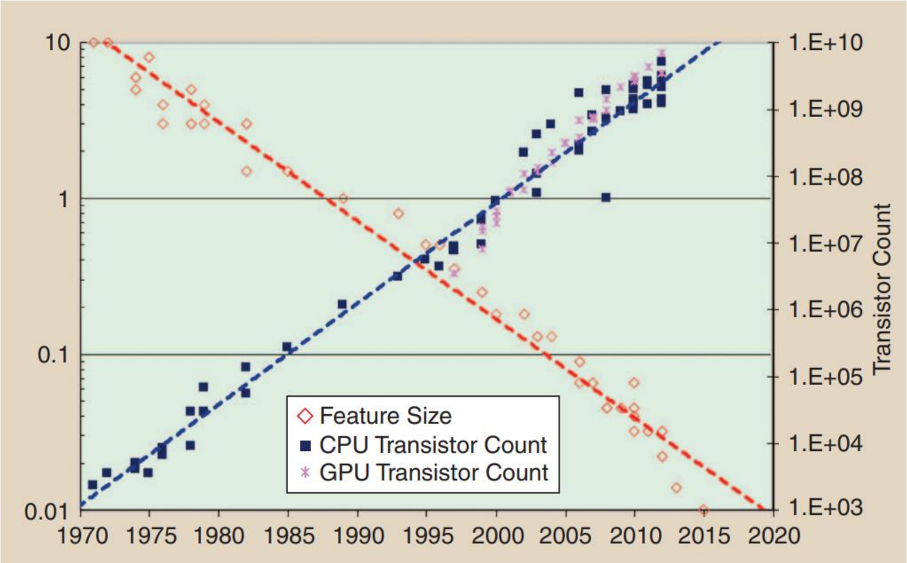

Figure 1. 1. Silicon process technology trend showing the exponential growth in the CPU/GPU transistor count and the decrease in feature size as a function of time. The left side Y-axis shows the feature size in micrometers and the right Y-axis is the transistor count (Adapted from [6]).

The electronics advancement between 1970 and 2019, allowed the components size to be reduced from approximately 10 µm to 10 nm. Reduction in the device sizes is possible due to the usage of the various small dimensional semiconductor components (such as a diode, transistor, field-effect transistors (FET), junction gate field-effect transistors (JFET), MOSFET and ICs). The continuous improvement in IC technology promotes the development of very-large-scale integration (VLSI) technology. Advancements in these devices allowed a further decrease in the cost for the mass production of personal computers for offices and homes. Since then, the advances in silicon technology have led to complementary metal-oxide-semiconductor (CMOS) technology. In this technology, the gate length is minimized, ultimately reducing the overall transistor size. For example, strained silicon technology was used for shrinking the channel length size to 90 nm (gate length 37/65 nm). Successively, the strained silicon technology turned out to be effective in scaling down to 45 nm (gate length 22/37 nm); but the use of a thin SiO_2 layer on 45 nm technology caused an increase in the leakage current [7]. Therefore, alternative high-k (dielectric constant) dielectric materials (HfO_2, ZrO_2, Al_2O_3) replaced SiO_2, beginning in 2007, which can prevent the tunneling leakage effect while improving performance [7]. However, when the channel length further depletes down to 32 nm, numerous other issues, such as current leakage, static power and significant reliability challenges occurred after fabrication. Hence, to overcome these effects, distinct competitive device structures, such as fully depleted silicon on insulator (FD-SOI) and fin field-effect transistor (FinFET), were fabricated to replace the traditional bulk CMOS, starting in 2012. The FD-SOI represents a planar technology by distributing an ultra-thin film of an insulator (buried oxide) on top of a silicon substrate and forming a very thin undoped silicon layer in the transistor channel. In this way, compared with bulk CMOS, it will have an ideal electrostatic component and can overcome leakage current [8,9]. Likewise, in FinFETs, the gate layout gets wrapped around the channel to control the channel current. This structure with additional gates is often called a multi-gate MOSFET, or tri-gate FET, and leads to improved coupling of the gate to the transistor channel, resulting in faster transistors and lower power dissipation.

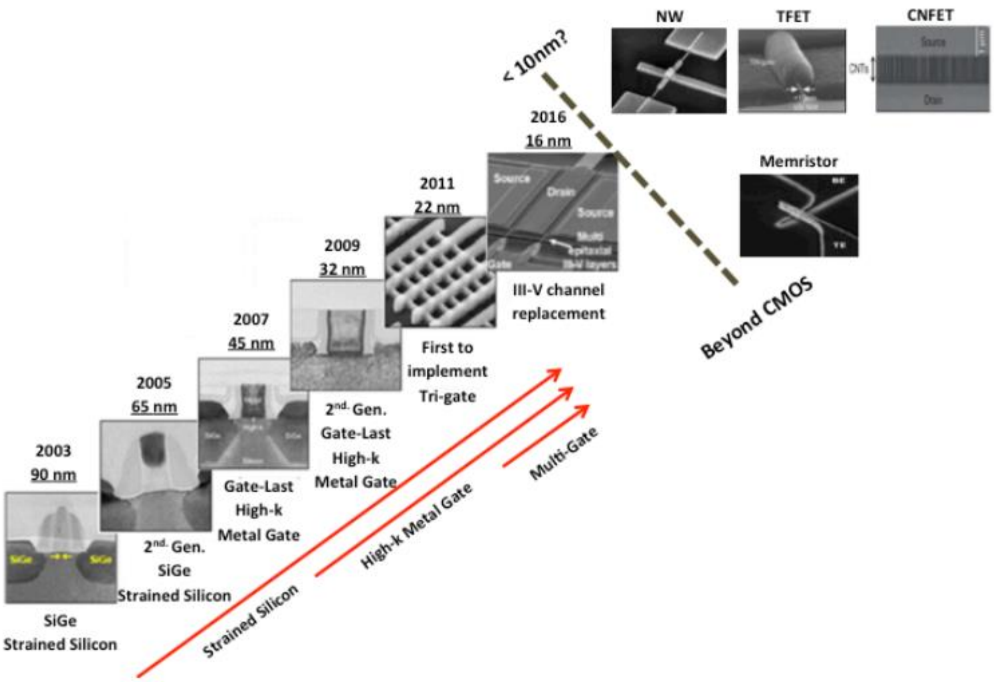

Figure 1.2. Technological roadmap of scaling in recent times and into the future (Adapted from [9]).

In general, scaling down the gate length makes the same circuits smaller, cheaper, faster and consume less power. However, scaling down can still cause many problems. For instance, a very short gate length can affect the whole design of the device due to so-called short-channel effects that alter device behaviour. Also, various obstacles may arise, such as overheating, static and dynamic power consumption, increased oxide electric field and a rise in leakage gate-current [7]. To address all these challenges, modern nanoelectronics were developed, that can presumably overcome the issues that arise from former CMOS technologies [10]. Researchers believe nanoelectronics technology can resolve two major expectations: physical size limitations and astounding costs incurred in manufacturing integrated circuits. In addition, modern nanoelectronics allows the expansion of integrated circuits beyond the limits of the latest transistors [10].

In the field of nanoelectronics, the continuous development of nanotechnology and the continual miniaturization of ICs, will ultimately lead to quantum-mechanical effects becoming dominant. These quantum effects on nanoelectronics devices can be divided into two sub-areas: Solid-state nanoelectronics devices and molecular electronic devices [11].

Solid-state nanoelectronics devices can be classified as single electron transistors (SET) and resonant tunneling diodes (RTD). The basic structure of SET comprises, the drain, source, gate and island. Unlike MOSFET, for electronic conduction, a single electron only contributes to the SET device. SET works on the basis of Coulomb blockade where gate insulator controls the flow of electrons moving from source to drain [12]. Likewise, RTD are generally sandwich structure devices, consisting of two thin barrier layers (wide band gap-AlAs) and a well (low band gap-GaAs) in between. The execution of RTD is determined by the electron tunneling, which occurs when the energy is equal to the resultant resonance energy of the barrier. The typical *I-V* characteristics of RTD (as shown in ***Figure 1. 3)*** is determined by the negative differential resistance (NDR) behavior.

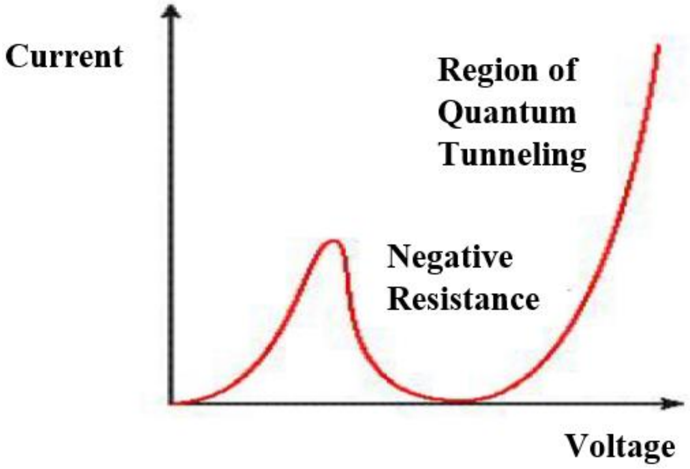

Figure 1. 3. Typical *I-V* characteristic of RTDs devices (Adapted from [13]).

On the other hand, the basic concept of creating any molecular device is to embed a few molecules or even a single molecule between two electrodes to form an electrode-molecule-electrode nano connection. Some examples of molecular electronic devices are molecular diodes, molecular memories, molecular wires, molecular switches and molecular FETs.

Research and development are ongoing to find suitable nanodevices with the best performance, reliability and stability. In the past decade, the conversion of planar structures to non-planar structures (three-dimensional structures such as double-gate transistors and tri-gate transistors) has dramatically improved short-channel performance and scalability [14]. Additionally, combining other novel electronic materials with silicon has improved the transistors' speed and energy efficiency. For instance, the merged tri-gate CMOS transistor (architecture with strained silicon channel, high-k gate dielectric, the metal gate electrode, and double epitaxially grown with raised source and drain) shows an excellent short channel characteristic and high drive current performance [15]. However, as downscaling continues, various non-ideal factors such as short channel effects (SCEs), poor electrostatic integrity and large device variability have emerged. Nevertheless, these advanced conventional bulk FinFET and FD-SOI are still evolving; they showed enhanced performance that overcomes non-ideal factors [16]. An example of FinFET device is shown in ***Figure 1.4***. Also, these devices are now extensively used for mass production from 22 nm to 10 nm node and are progressing towards the 5 and 3 nm nodes [17,18], including gate-all-around devices and 3D integration, wherein the channel is an elevated sheet or ribbon surrounded by the gate on all sides.

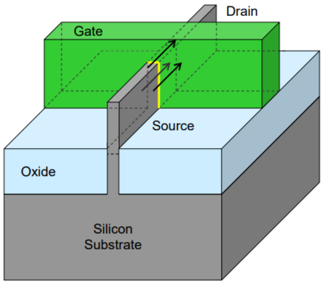

Figure 1.4. 3-D Tri-Gate transistors from conducting channels on three sides of a vertical fin structure, providing "fully depleted" operation (Adapted from [19]).

The different nanostructured materials, such as quantum dot (QD), nanowire/nanotubes (NW/NT) and thin films, have shown remarkable improvement in device scaling and are now gaining significant attention for use in integrated nanoscale electronics. Examples of such nanostructured materials are single-layer graphene FETs [20], transition metal dichalcogenides (TMDCs) and classes of 2D IV-IV and III-V compounds [21]. Since traditional IC scaling is approaching its physical limit, various other nanostructured materials are continually being explored to integrate on future devices. Thus, the device integration of different nanostructured materials (QD, NW and thin films) is underway, including ***(Figure 1.5)*** by using quantum dots/nanowires or stacking channel materials.

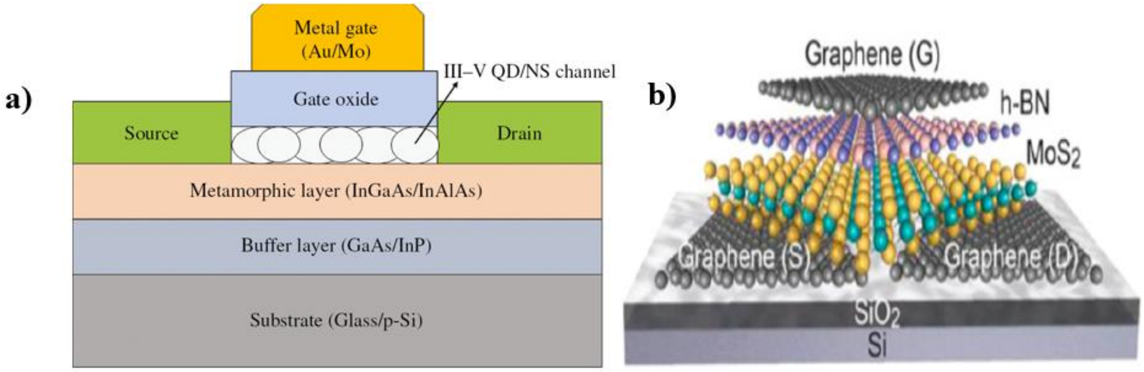

Figure 1.5. (a). Cross-sectional schematic of III-V QD/nanostructured (NS) channel based MOSFET (Adapted from [21]). (b) Schematic of advanced FET created using stacked 2D materials for all of the components, including the semiconductor, insulator and metal layers (Adapted from [20]).

1.2. Nanomaterials

This section is mainly focused on nanomaterials and their general classification based on dimensionality. Nanomaterial properties, applications and fabrication techniques are also discussed in some detail.

When physicist Richard Feynman in 1959 presented his speech, “There is a Plenty of Room at the Bottom,” it was considered the commencement of nanotechnology [22]. Later, Professor Norio Taniguchi in 1974 created the word “nanotechnology.” The breakthrough progression occurred only in 1985 with the discovery of new shapes for the molecule of carbon known as a buckyball, which is round and comprises 60 carbon atoms. Furthermore, in 1990, the IBM physicists’ team spelt out the letters “IBM” using 35 individual xenon atoms achieved significant progress. The ongoing research in nanotechnology covers various fields with dimensions less than one-tenth of a micrometer. Likewise, the rapid downscaling of the material to nanosize enhances unique properties that make nanomaterials prevalent in today’s electronic devices.

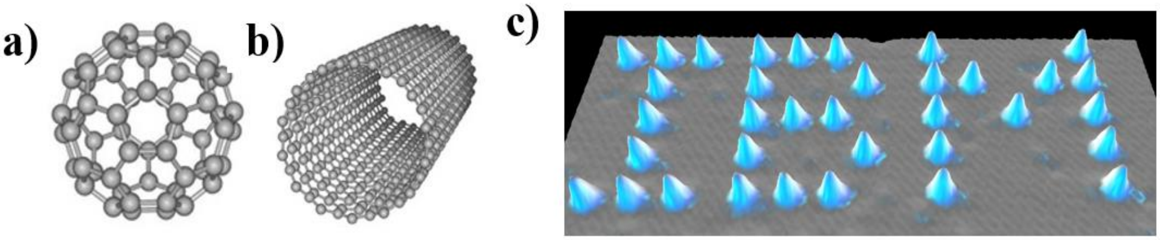

Figure 1.6. (a) Fullerence-C_{60} (b) Carbon nanotube (c) 35 Xenon atoms in the shape of “IBM” positioned on nickel crystal (Adapted from [23]).

Based on the grain size, materials occur in different forms, such as nanoparticles, ultra-micro size particles and nanophase materials, where the grain sizes are on the order of a few nanometers [24]. Specifically, materials with a length scale of about 1 to 100 nanometers (nm) on any dimension are nanomaterials. They can be metals, ceramics, polymeric or composite materials. In addition to that, nanomaterials are also available in amorphous or crystalline form. In the following section, nanomaterial classification, properties, fabrication techniques and application are covered.

1.2.1. Classification of Nanostructure materials

The classification of material depends on the number of dimensions outside the nanoscale (<100 nm) range: zero-dimensional (OD), one-dimensional (1D), two-dimensional (2D) and three-dimensional (3D). For zero-dimensional nanomaterials, all the dimensions reside within the nanoscale (no dimensions are higher than 100 nm), examples: nanoparticles and atomic clusters.

Similarly, in the one–dimensional nanomaterials, one of the dimensions lies outside the nanoscale range, and its typical examples are nanotubes, nanorods and nanowires. Likewise, in two–dimensional nanomaterials, two dimensions exceed the limit of the nanometer scale, taking nanoplates, nanofilms, nanolayers and nanocoating as examples. Furthermore, in the bulk materials (bulk powder, dispersion of nanoparticles, multi-nanolayers, the bundle of nanowires and nanotubes), all three dimensions are outside the nanoscale range [25].

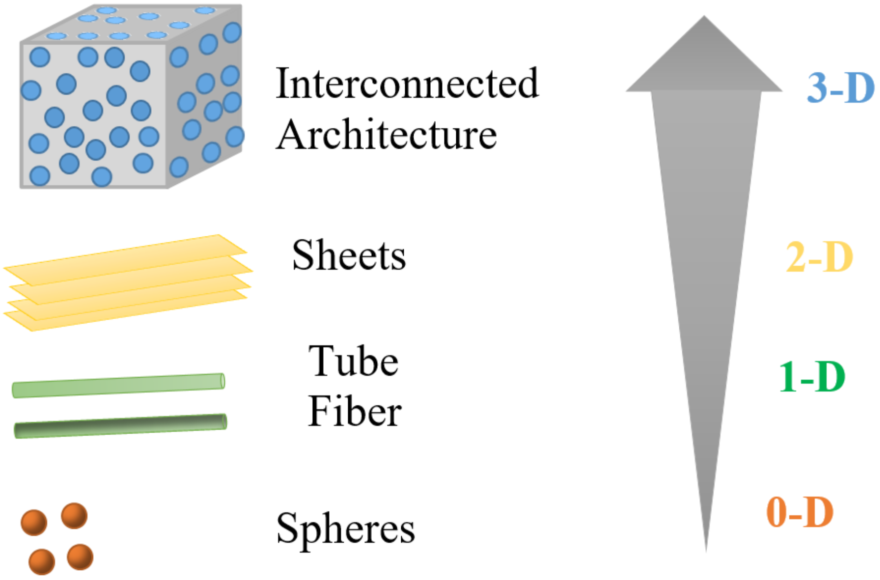

Figure 1.7. Classification of nanoscale dimensions (Adapted from [25])

1.2.2. Properties of Nanomaterials

There has been an enormous interest in nanomaterials due to their unique mechanical, electrical, magnetic, and optical properties. In contrast to large scale, or bulk, materials, at the nanoscale, the shape and size of a nanoparticle can result in a vast difference in their structural and chemical properties [26–33]. For example, in the nanosized materials the percentage of atoms at the surface of materials becomes very large, and hence, their properties chemical reactivity can dramatically increase. Thus, various novel features of nanomaterials make them one of the potential choices for creating nanoelectronics devices. Some of their unique properties are discussed in the following section.

- **Optical Properties**

The most fascinating and useful features of nanomaterials are their optical properties. Devices like optical detectors, lasers, sensors, imaging, displays, solar cells and photocatalysis are based on the optical properties of nanomaterials. The optical characteristics of nanomaterials depend on feature size, shape, surface properties, doping and interaction with the surrounding environment or other nanostructures. Generally, the optical properties of metals and semiconductor nanoparticles change due to their morphology [26,27]. ***Figure 1.8 (a)*** represents the difference in the optical performance of metal and semiconductor nanoparticles, where altering the size of cadmium selenide (CdSe) nanoparticles shows a change in the optical properties [34]. The energy level determines the change in color for different size quantum dots. The band gap emission shows red emission for the largest particles and blue emission for smallest particles. Smaller the particle size the larger is the band gap, where the valance and conduction breakdown into quantized energy levels. Similarly, a small change in metal nanoparticles' dimension can create an enormous change in their optical behavior (shifting of the surface plasmon band to longer wavelength with increase in particle size), just as observed in different samples of gold nanospheres in ***Figure 1.8 (b).*** [28].

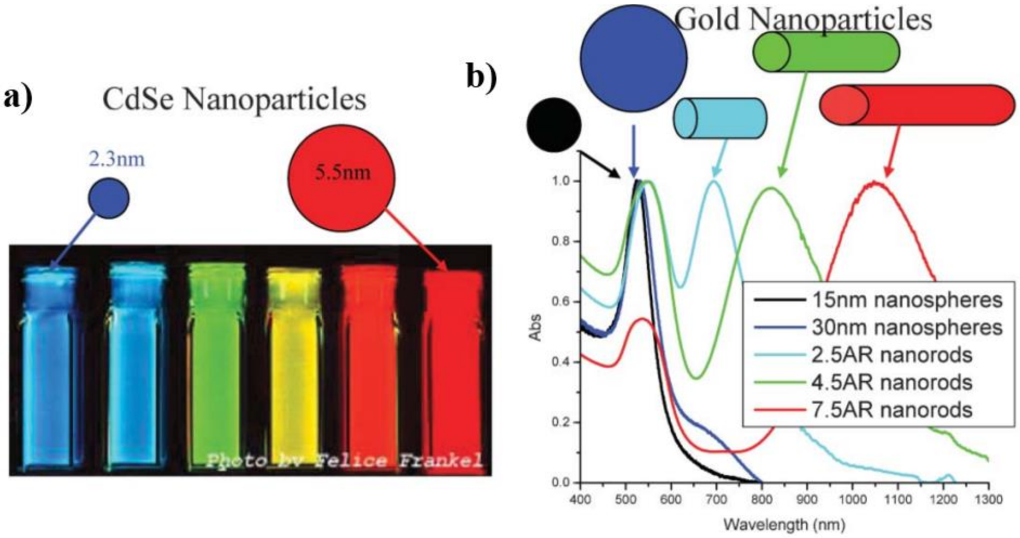

Figure 1.8. (a) Fluorescence emission of (CdSe) ZnS quantum dots of various sizes [34] (b) Absorption spectra of various sizes and shapes of gold nanoparticles. (Adapted from [28])

- **Electrical Properties**

Fundamentally, research on electrical properties of nanomaterials often focuses on the effect of surfaces on the conductivity of nanoparticles, nanotubes, nanorods, nanocomposites and nanostructures. Nanostructure size is important to the electrical properties based on different mechanisms, such as surface scattering, change in the electronic structure, quantum transport. Similarly, nanoscale structure (such as impurities, structural defects and dislocations) will also affect the conductivity of nanomaterials. For example, n-type ZnO, where electrons are main carrier charges, the conductivity is often attributed to oxygen and zinc interstitials. The oxygen vacancies in ZnO are actually +2 charged and are responsible for the unintentional n-type conductivity as well as the non-stoichiometry of ZnO [35]. The study shows that oxygen vacancies act as the dominant donor-like native defects in ZnO [35]. However, fundamental understanding of oxygen vacancies (V_o) is still very sparse in case of its electrical conductivity [36]. Also, ZnO could have either Zn interstitial or oxygen vacancy or both, which lead to excess unpaired electrons that enhances n-type conductivity On the other hand, the electrical properties of carbon nanotubes depend on how the hexagons are oriented along the axis of the tube as shown in ***Figure 1. 9***. Carbon nanotubes with the hexagons orientated in the configuration labelled armchair have electrical properties similar to metals and other two possible orientations (zigzag and chiral) of hexagons in carbon nanotubes behaves like semiconductors [37].

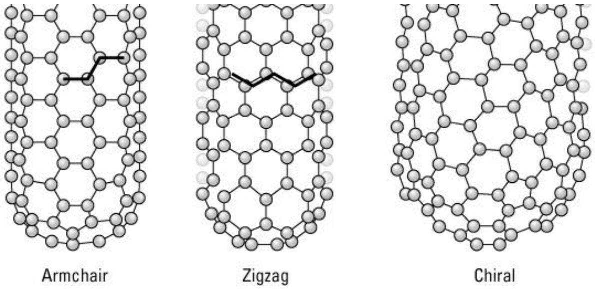

Figure 1. 9. CNT electrical properties depend on the orientation of hexagons shown for different tube types [38].

- **Structural Properties**

The structural properties of nanosized materials show some astonishing behavior, which is unique from their bulk counterpart. The structural features (such as size, shape, specific surface area, aspect ratio, morphology and structures) change at the nanoscale and show unique properties within the nanostructured materials. Indeed, the smaller the particle, the stronger the quantum size effect, in particular energy level quantization. The quantum effect is usually observed when the particle size is small to be compared to the wavelength of an electron. Other effects arise from incomplete surface bonding: bulk gold requires a high temperature of 1064 ^{0}C to melt, while 2.5 nm gold nanoparticles can melt at 300 ^{0}C. Also, when changing from bulk crystal to nanocrystals, the structure of the material is affected. The changes mainly occur in lattice parameters at the nanoscale and lead to new phases of nanostructures. An example shown in ***Figure 1.10.*** exemplifies the tuning of the morphology of ZnO possible with change in precursor concentration.

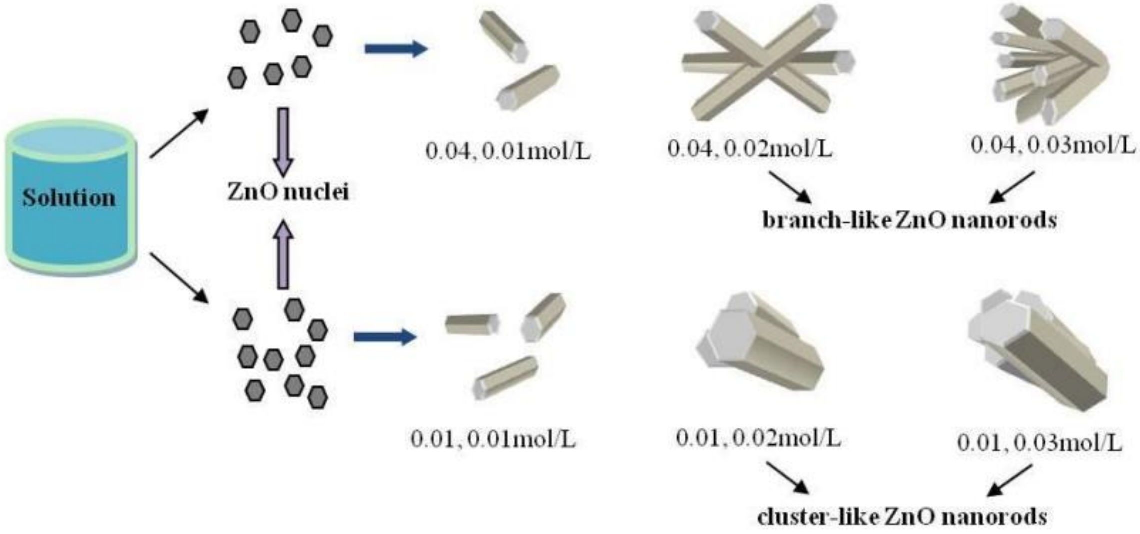

Figure 1.10. The schematic of the growth process of formation of branch-like ZnO and cluster like ZnO nanorods with different precursor concentration (Adapted from [31]).

- **Chemical Properties**

One of the main features of the chemical properties of nanomaterials is the increased surface area, which significantly enhances the chemical activity of the material. Nanomaterials are used as *catalysts* to react with harmful and toxic gases produced by industries, thereby reducing pollution. Interestingly, metals such as bulk gold are chemically inert and have poor catalytic performance. However, its nanoparticles have excellent catalytic properties. The main factors affecting the catalytic activity and selectivity are the surface structure, surface chemistry, pore size, the mobility of the active species and the migration of adsorbates on these active sites. Most importantly, the reduction in particle size creates most of the atoms on the surface, resulting in a higher surface area. This phenomenon establishes more reactant molecules adsorption on its surface, leading to higher catalytic activity [33,39]. The general mechanism of dye degradation is shown in ***Figure 1.11 (c).*** At first, electron-hole pair gets generated after absorption of photons by nanocatalyst. The photogenerated electrons and holes are transferred to the photocatalyst surface. The electron (e^-) at conduction band reduces adsorb oxygen (O_2) to superoxide radicals ($O_2^{\cdot -}$). At the same time, the hole (h^+) at valance band oxidizes water molecule to generate hydroxyl radicals ($OH^{\cdot}$), that works on MB degradation. The formed radicals initiate the redox reactions and degradation of MB into CO_2, H_2O or inorganic ions [39].

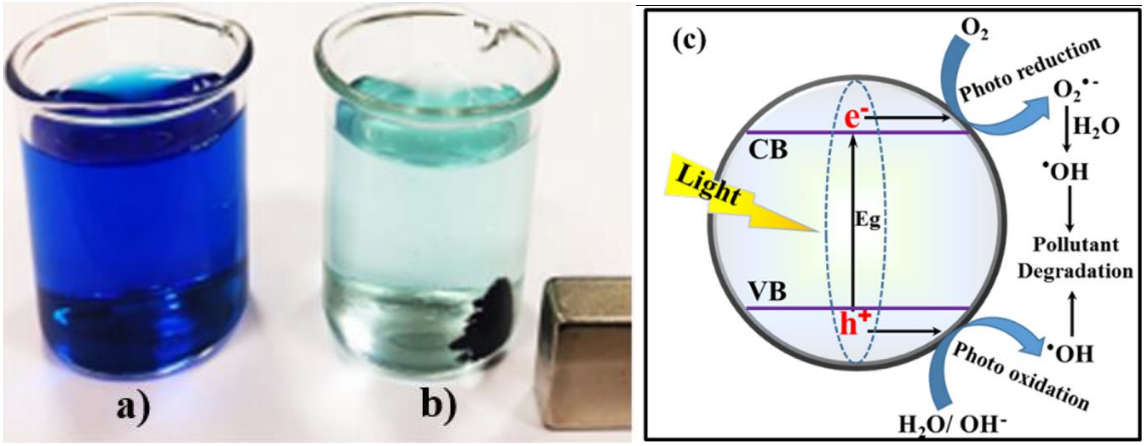

Figure 1.11. Photograph of MB aqueous solution (a) with dispersed Fe_2O_3@SiO_2 NPs before solar irradiation (b) after two hours of solar irradiation and magnetic separation using an external magnet, (c) photocatalytic mechanism. (Adapted from [39]).

- **Magnetic properties**

The surface of nanomaterials is composed of numerous atoms, and these atoms will have different magnetic coupling with neighboring atoms, resulting in unique magnetism. For example, nanoparticles of gold (Au), palladium (Pd) and platinum (Pt) show magnetism, which is different from the non-magnetic bulk. Similarly, most non-ferromagnetic bulk materials exhibit ferromagnetic-like behavior in their nanopowder form. For Pt and Pd metals, ferromagnetism originates from structural transformations related to size effects [40,41].

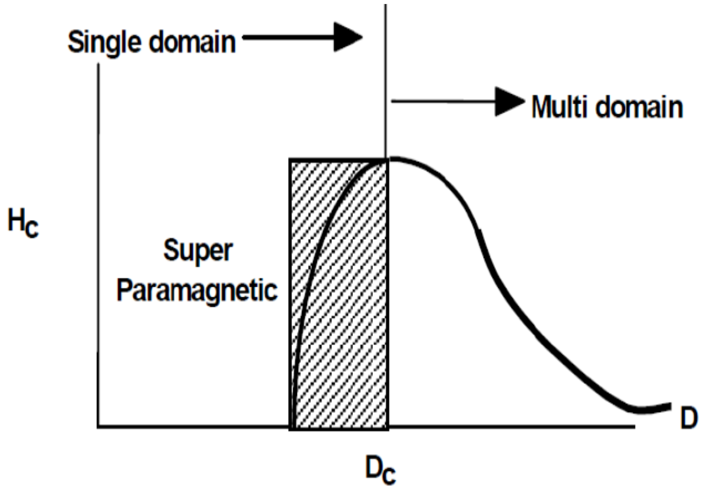

Figure 1.12. Magnetic properties of nanostructured materials [41].

1.2.3. Nanomaterials Fabrication

In general, there are two ways to synthesize nanostructured materials: top-down and bottom-up methods (shown in ***Figure 1.13***). In short, assembling basic units into a larger structure is a bottom-up approach, while making nanoparticles/fine particles from larger scale materials or bulk powders is top-down. The presentation of both techniques is in the following section.

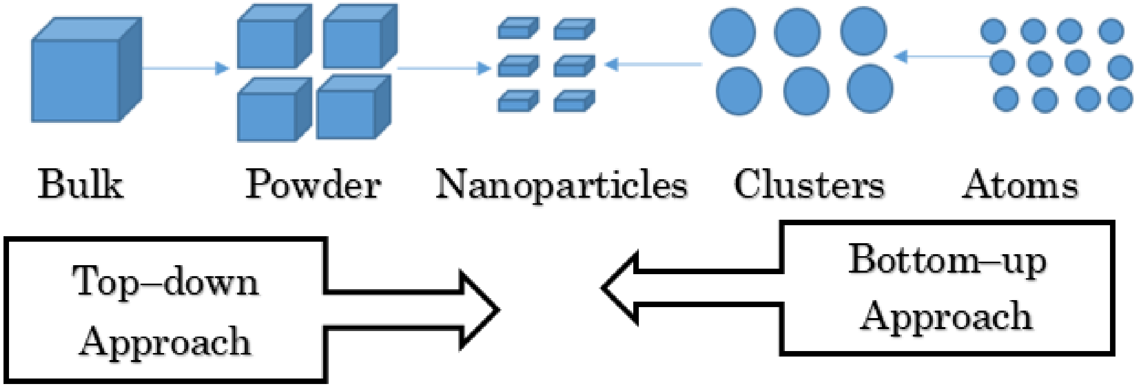

Figure 1.13. Schematic representation of building of nanostructures.

1.2.3.1. Top-down approach

These approaches use bulk (macroscopic) as an initial structure, where pulverization or grinding or controlled removal of material occur to form finer/nano-sized particles. Techniques such as milling or lithographic are used to make nano-features, and both methods will be explained in this section.

i. Lithography

Lithography is a top-down synthesis technique, which usually transfers patterns or designs to different substrates. In general, this method creates fine patterns using the physical and/or chemical processes, i.e., the physical top-down approach employs the use of electrons (electron beam lithography), photons (optical lithography) and ions (ion beam lithography), and the chemical top-down approach is the chemical reaction formed by chemical etchants or by application of heat. The common lithography process is optical lithography (shown in ***Figure 1.14***), also known as photolithography, where ultraviolet light (UV) shifts the desired design from a mask to a photoresist stuck on substrates. The radiation transmitted through the mask makes the exposed photoresist soluble/insoluble in the developer solution. After the patterns are defined, with the help of etching, the pattern gets transferred onto the substrates [42]. Overall, these techniques create fine-scale patterning of ICs.

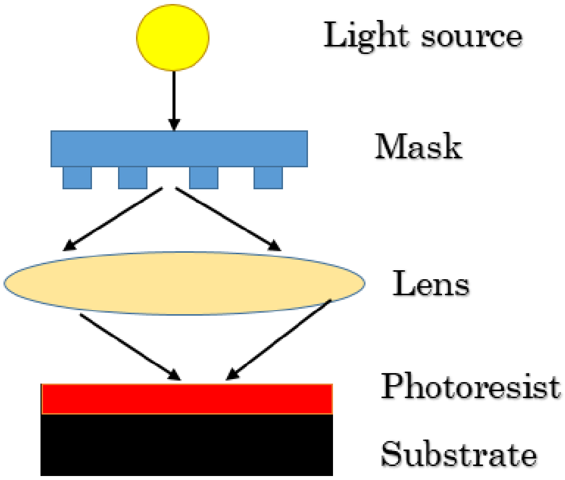

Figure 1.14. A schematic diagram of conventional projection optics system for optical lithography (Adapted from [43]).

Other promising techniques for next-generation lithography (NGL) are extreme ultraviolet lithography (EUVL), electron-beam lithography (EBL), focused ion beam lithography (FIBL) and hybrid approaches such as directed self-assembly (DSA). In brief, EUV lithography uses soft X-ray ($\lambda = 13.5$ nm) light source that can pattern beyond 10 nm node. This technique used several multilayer mirrors which acts as the ultra-reflective mirrors that guide the light to land on the wafer [44]. Similarly, EBL and FIBL are direct writing technique, which uses focused beam of electrons and ions to create patterns on the resist, respectively [44]. On the other hand, DSA techniques are combined with lithographic template patterns with lamellae-forming self-assembling material for creating miniaturized logic and SRAM patterns [45]. In particular, they have distinct benefits in achieving mass production and high resolution, replacing conventional lithography techniques

[44]. Also, these methods were used for creating new devices using nanoparticles, nanowires and nanosheets [46,47].

ii. Milling technique

In brief, grinding is carried out through a combination of friction, attrition, and impact. Attrition or milling usually means reducing the material to sizes in the low micron or even nano-size range. Moreover, the types of stress generated during the grinding are compression, shear (attrition), impact (stroke) and effect (collision). These different types of stress are shown in ***Figure 1.15***.

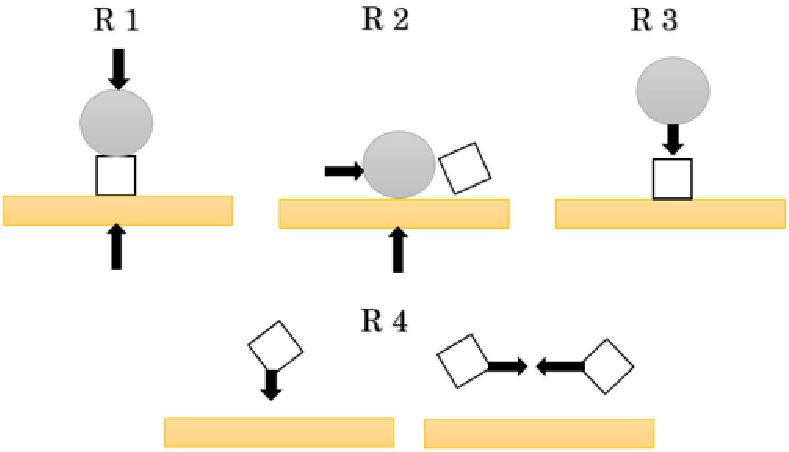

Figure 1.15. Main stress types in mills, R1 – compression, R2 – shear (attrition), R3 – impact (stroke), R4 – impact (collision), circle – mass of milling media, square – mass of material charge, rectangle – mass of mill wall (Adapted from [48]).

HEBM is commonly a top-down method used to create different types of nanomaterials (nanograins, nanocomposite, nanoalloys and nano–quasi-crystalline materials). Using this technique provides several advantages, such as scalability, versatility, and cost-effectiveness, whereas plastic deformation, cold-welding and fracture are inherent demerits of this method. Cold welding of different powder particles occurs when particles mutually penetrate each other through subsequent collisions with the grinding beads [49]. Particularly, cold welding leads to an increase in the particle size and fracture to decrease the particle size [49]. In brief, the purpose of the milling media is to reduce the particles to a more selective size and mix them to transform them into a new phase.

Usually, in the ball milling technique, pulverizations occur due to the high-energy impact of the grinding balls and partly due to the friction between grinding balls and the wall of the grinding bowl. During operation, the powder trapped in the grinding balls is crushed down into a distribution of sizes, but the nature of the powder (hard or soft) and energy transferred from the ball to the powder determines the actual shape/size of the crushed powder. In addition, the transferred energy is controlled by many parameters, such as mill type, powder type, grinding speed, grinding ball size, grinding medium (dry or wet), grinding time and temperature [50]. Thus, soft bulk particles or brittle particles can form finer nanopowder, but hard/firm materials can only change their shape/morphology [51]. However, continuous collision between milling balls and hard powder may enhance the fracturing process. Depending upon the ductility of milled materials, fracturing or cold welding can dominate, where notable cold welding become prominent on ductile powders [52]. Changing milling atmosphere or adding process control agent (PCA) can reduce the effect of cold welding [52]. On the one hand, HEBM has many advantages, such as producing fine nano-powder, grinding in both dry and wet mediums, grinding toxic materials, and having lower installation costs. On the other hand, milling can lead to some complications in particles that include imperfection of surface structure, defects (bulk) and material contamination.

Numerous coarse-grained structures are ground by this technique and can produce crystalline nanomaterials/nanopowder [53]. In most cases, the interior volume crystallographic structure of the starting material remains unchanged when the grain size reduces to an average size *d* of ca. 10 nm, the typical size reached by modern high-energy laboratory mills [53]. Milling techniques are also capable of creating new metastable phases [54]. Remarkably, some milling techniques can make nanoparticle alloys with sizes below 5 nm [54].

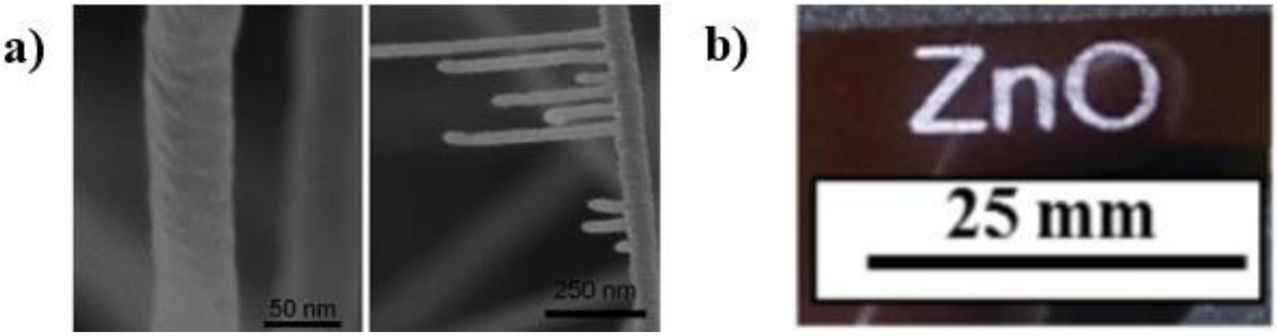

Figure 1.16. a) SEM images of ZnO nanowires (right-branches of nanowires, left – typical single nanowires). The prepared nanowires range from 20-80 nm in diameter with a length up to tens of micrometers [55]. b) ZnO pattern printed in 10 passes on silicon wafer. The ZnO ink is prepared from ball milling technique (Adapted from [56]) .

HEBM is typically used in the microelectronic and material processing industries, such as cement, pigments, paints, ceramics, dispersions, and pharmaceuticals. In brief, the ball milling technique has successfully produced nanomaterials of various sizes, such as nanopowder, nanowires and thin films, an example is shown in ***Figure 1.16 (a)*** [49,50,53,55,57–59]. Milled powders were placed in tube furnace and annealed at high temperature (1300 ^{0}C) under argon atmospheres to create nanowires [55]. Similarly, wet milled suspension was coated on various substrates to create nanostructured thin films [56,60]. The resultant milled nanostructured powder/ink could be used for large-scale utilization (example as ***Figure 1.16 (b)***), and it is also conceivable that milled nanoparticles could be used in next-generation devices [56,61–65].

1.2.3.2. Bottom-up Approach

Generally, this groups of techniques utilizes the concept of (molecular) self–assembly, in which the synthesis of nanostructured materials occurs atom-by-atom, molecule-by-molecule or cluster-by-cluster. The merit of using this method helps to produce nanomaterials with fewer defects and more desirable chemical composition in large numbers. A brief description of the most common bottom-up approaches follows.

i. Vapor phase fabrication

Normally, chemical vapor deposition (CVD) is still one of the typical vapor-phase fabrication methods used in the bottom-up approach, which has produced high purity, high-performance solid materials and coatings for nanoelectronics devices. In this deposition process, the substrate gets exposed to one or more volatile precursors that react and decompose on the substrate to form the desirable film layer, whereas the volatile–by-products are removed from the reactor with the carrier gas flow.

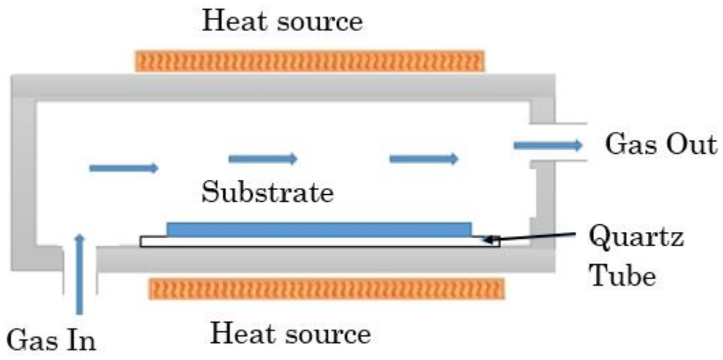

Figure 1.17. Typical chemical vapor deposition technique.

ii. Liquid phase fabrication

The common bottom-up approach of the liquid deposition technique is self-assembled monolayer (SAM). The stability of monolayer is affected when exposed to air or at high temperature. Various approaches (example: UV irradiation, or light exposure), were implemented to improve chemical stability and thermal stability of the monolayers [66,67]. In general, SAM is an organized layer consisting of amphiphilic molecules, in which the hydrophilic "head" group exhibits a strong affinity with the substrate and the hydrophobic "tail" group consists of a functional group, as shown in ***Figure 1.18***. Furthermore, they are formed from molecules either by dissolving in solution or condensing on the surface from the gas phase. Hence, being an efficient, rapid and straightforward method to create functional features at various length scales, this technique has been one of the preferred bottom-up approaches.

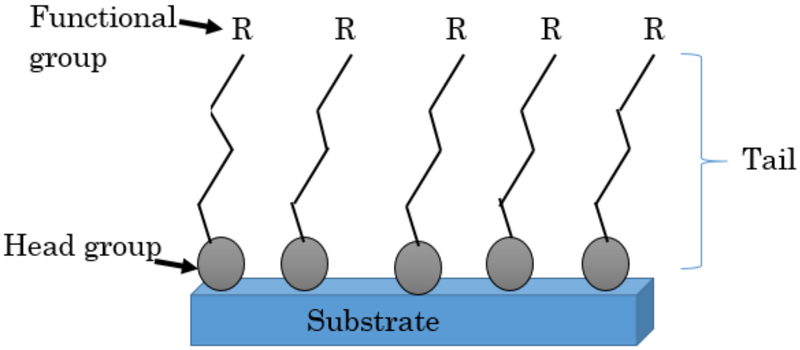

Figure 1.18. Schematic of a self-assembled monolayer.

1.2.4. Nanomaterials Applications

In addition to the applications in nanoelectronics discussed at the beginning of this chapter, nanostructured materials are used often in industry due to their unique magnetic, electrical, optical and chemical properties. Moreover, their application areas range from medical to modern engineering sectors in which common uses are fuel cells, catalysis, sensors, flexible electronics, energy storage devices and environmental remediation [68,69]. A brief explanation of each application is as follows.

i. Fuel cells:

In general, the fuel cell is an electrochemical conversion material that can directly convert the chemical energy of the fuel (anode) and oxidizer (cathode) into electrical energy. In this process, oxygen and hydrogen are formed without carbon oxide emission. Some example of fuel cells is proton exchange membrane fuel cell (PEMFC), molten carbonate fuel cell (MCFC), solid oxide fuel cell (SOFC), phosphoric acid fuel cell (PAFC) etc. Commonly, platinum (Pt) is the often used metal catalyst as an electrode material. Despite being expensive, this metal has not been replaced yet. However, there are other optional nanocatalysts, such as transition metal oxides, iron-based catalysts and carbon-based catalysts. Ultimately, the performance of a fuel cell mainly depends on the type of electrode.

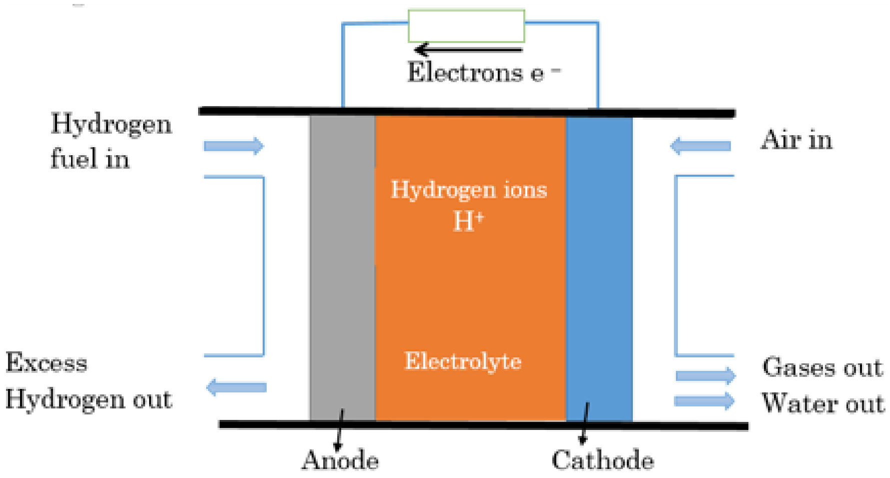

Figure 1.19. (a) Schematic diagram of hydrogen fuel cell.

ii. Catalysis

Nanomaterials have great potential and can meet the needs of future catalytic process technologies. Indeed, the smallest nanocatalysts have a higher surface area, generating more adsorption sites and enhancing catalytic reaction. Significantly, nanocatalysts in a chemical reaction can lower the activation energy and help to increase the rate of reaction by providing an alternative reaction pathway [70]. There are wide range of applications where nanocatalyst are used, such as water purification, biodiesel production, fuel cell applications, photocatalytic activity, wastewater treatment etc., [71]. Nanocatalysts can be metal-based nanocatalysts, carbon-based nanocatalysts and ceramic-based nanocatalysts [72]. An example of a photocatalytic experiment (shown in ***Figure 1.20)*** was performed using N-doped ZnO nanocomposites, where the degradation of dye in aqueous suspension was examined under sunlight radiance at ambient temperature [73].

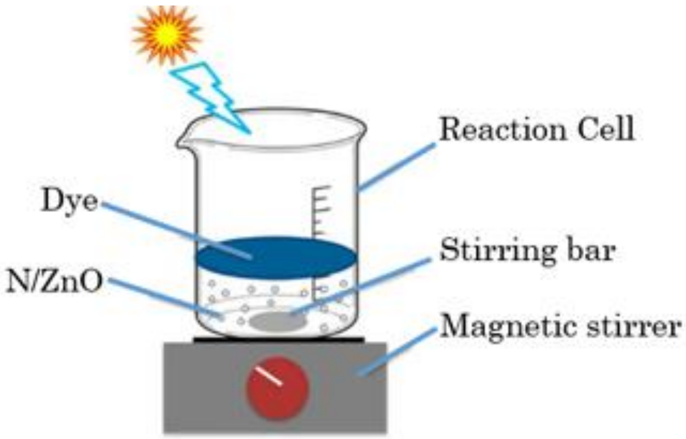

Figure 1.20. Schematic diagram of the reactor for photocatalytic degradation of dye (Adapted from [73]).

iii. Sensors

Nanosensors convert physical, chemical or biological stimuli to measurable output signals and act as sensing elements or receptors or as transducing components (e.g., electro-or chemo-mechanical actuators) or even electrodes in power systems [74]. The common nanosensor includes three elements: nanomaterials, recognition parts and signal transduction components. Large surface-to-volume ratio and facile surface functionalization, makes the surface chemistry of nanoparticles sensitive, enabling them to reach a narrow detection limit. The high gas sensing performance of metal oxide is mainly due to large surface-to-volume ratio because it allows a large, exposed surface area for gas detection. Various morphological nanostructures offer the more adsorption sites as they possess inner and outer surfaces, hence higher sensing performance is expected [75].

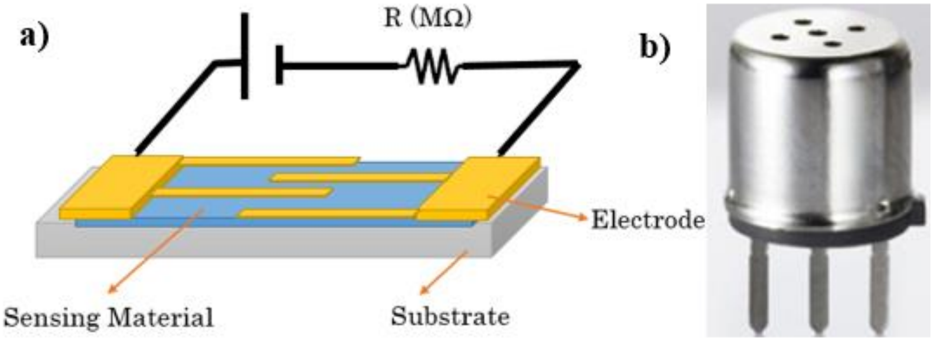

Figure 1.21. (a) Schematic view of chemiresistor sensor. The sensing material shows a change in resistance between patterned electrodes when exposed to analytes. (Adapted from [76]). (b) Metal oxide semiconductor gas sensor invented by Nissha FIS, Inc (Adapted from [77]).

iv. Flexible electronics

Generally, the typical structure of a flexible electronic device includes a substrate, backplane electronics, a front plane and encapsulation. Most importantly, the ductility of this bendable device allows all components to maintain a certain degree of bending without affecting their function [78]. Silicon materials are the driving force for manufacturing miniaturized devices that reduce costs and increase efficiency. However, the rigidity of silicon hinders its widespread use in flexible and stretchable electronic applications. Therefore, to overcome the rigidity of conventional silicon technology, research in finding alternative materials/substrates is ongoing. For example, compared with conventional silicon, nano-carbon materials such as carbon nanotubes (CNTs) and graphene have excellent elasticity and have superb electronic, photoelectric and thermal properties [79]. In addition, some other non-carbon materials, such as indium tin oxide (ITO), conductive polymers, silver or copper nanowires, are also used to make various flexible electronic devices [80].

Overall, advances in flexible electronics technology have shown the potential to provide cost-effective solutions for large-area applications such as foldable displays and TVs, smart sensors, electronic paper and transparent radio-frequency identification (RFID). In brief, manufacturing cost, lightweight, bendable, portable and low device price make it an ideal candidate for next-generation consumer products.

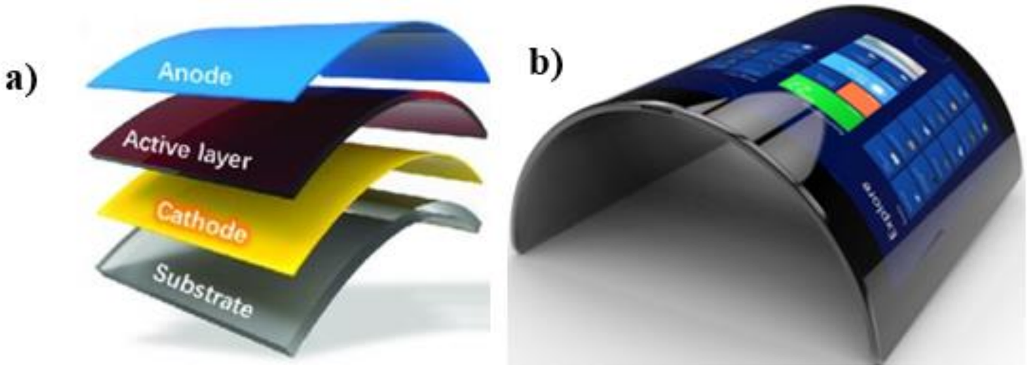

Figure 1.22. (a) Schematic diagram of flexible solar cell device (Adapted from [81]). (b) Flexible display of smartphones.

v. Energy storage devices

Ideal energy storage devices made of nanostructured materials are batteries, fuel cells, capacitors and supercapacitors [82]. Both the batteries and fuel cells rely on the conversion of chemical energy into electrical energy. In contrast, capacitors depend on the physical separation of an electrical charge across a dielectric medium (polymer film or an oxide layer). Correspondingly, supercapacitors rely on separating chemical charged species at the charged interface between the solid electrode and the electrolyte. Among all, supercapacitors can produce high power density and relatively high energy density [83]. Numerous nanomaterials, such as metal oxide, polymer-based nanoparticles and carbon-based materials, are used for creating various energy storage devices.

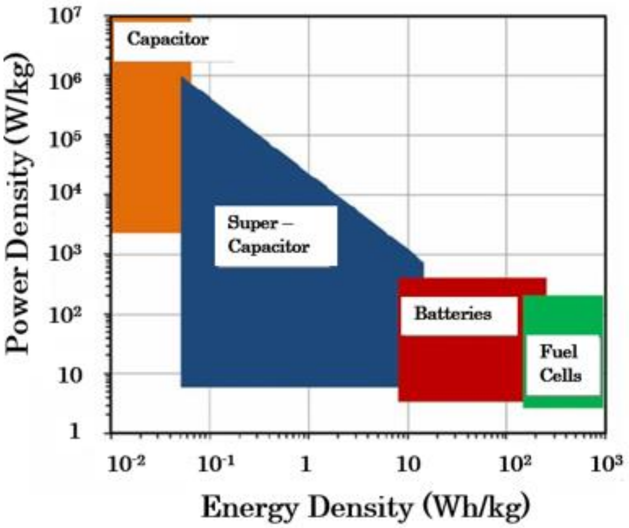

Figure 1.23. Ragone plot showing high energy and high power densities of different energy storage devices [83].

vi. Environmental remediation

Nanostructured materials have shown a promising role in monitoring pollution and acting as a remediation material in the environment. Different nano-photocatalyst like SiO_2, TiO_2 and ZnO are commonly used to remove pollutants, such as waste air/water treatment, self-cleaning materials, industrial applications and sustainable energy production [84]. For example, the enhanced chemical activity in nanoparticles shows their catalytic behavior that quickly reacts with toxic gas and prevents environmental pollution [85].

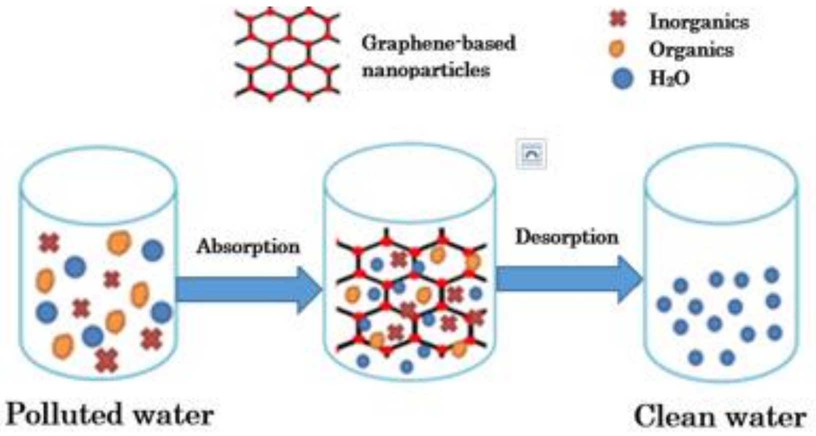

Figure 1.24. Graphene-based nanomaterials are used for removing organic and inorganic water pollutants. [85].

vii. Nanomaterials and the Environment

Although compared to the bulk, nanomaterials have numerous advantages; however, there are some potential shortcomings that cannot be neglected; they are particle instability, impurities, toxicity and recycling and disposal issues. The nanoparticles stay in tiny forms with high free energy; thus, they aggregate quickly and create agglomeration. As nanoparticles are highly reactive, they inherently react with pollutants as well. Likewise, nanomaterials' toxicity occurs due to their high surface area and enhanced surface activity. The primary concern with nanomaterials is their toxicity, and the uncertainties related to the effect of nanomaterials have not been resolved by the formulation of disposal policies [86].

As discussed in this chapter, the research and application of nanostructured materials has increased rapidly over the past few decades due to their novel physical and chemical properties, which differ from their bulk counterparts. As a result, these differences often show unique electrical, mechanical, magnetic, and optical properties. Thin film nanostructured surfaces created using nanoparticles have shown a wide range of applications such as solar cells, gas sensors, photocatalysis and piezoelectric devices [39,64,76,87]. The tunable properties of nanostructured films are made possible by controlling their morphology/particle size and interface effects. Semiconducting materials such as silicon, and other materials such as $TiSi_2$ are preferred for the development of CMOS technology. Silicon's success largely owes to its abundance, leading to the single-crystal wafers used for large production of ICs and electronic components with excellent chemical and physical properties [88–90]. Apart from that, silicon nanostructured materials are used for other various application such as, surface coatings, photonics devices and energy storage devices. Likewise, $TiSi_2$ has been one of the most vital silicides for CMOS device applications such as contacts to source/drain actives and gate regions due to their low resistivity and good thermal stability [91–94]. Lastly, ZnO has demonstrates low resistivity, non- toxicity, large exciton binding energy, different morphological nanostructures, and wide band gap [31,87,95–100]. These characteristics make ZnO a potentially outstanding choice for various applications in electronics, optoelectronics, biotechnology and sensing.

This research is focused on creating nanoparticle suspensions using the nanoscale grinding approach via PBM for Si, $TiSi_2$ and ZnO powders in processing regimes that have not previously been studied, and depositing the resulting nanoinks to fabricate nanostructured thin film coatings on various surfaces with novel tunable properties: The resultant nanostructured film properties were found to depend on the combination of grinding material, solvent and nanoparticle geometries/dimensions that depend upon the particular milling/grinding parameters used (speed, time, and solvent).

1.3. Research Objective

Overall, the primary purpose of this research is to examine the grinding parameters and determine the appropriate grinding conditions for different starting powder materials that is effective for the specific application. A schematic representation of the work is presented in ***Figure 1. 25***.

Different nanostructured bulk powders (silicon, $TiSi_2$ and ZnO) were ground in an appropriate solvent using the nanogrinding technique. The prepared colloidal suspension is later applied to create a thin film on various substrates. The nanostructured film properties (particle size, roughness, conductivity, porosity, crystallinity etc.) and applications (gas sensing) were then investigated.

Thin film wettability, conductivity, and gas response properties are experimentally measured and varied by adjusting the grinding parameters used to create the nanoparticle inks. Both hydrophilic and hydrophobic film and low and highly resistive films were successfully produced from colloidal suspension. Similarly, particle size, surface roughness, porosity and surface chemistry changed depending on grinding conditions and we observed that these effect could be used for tuning the different gas sensing properties of the thin films.

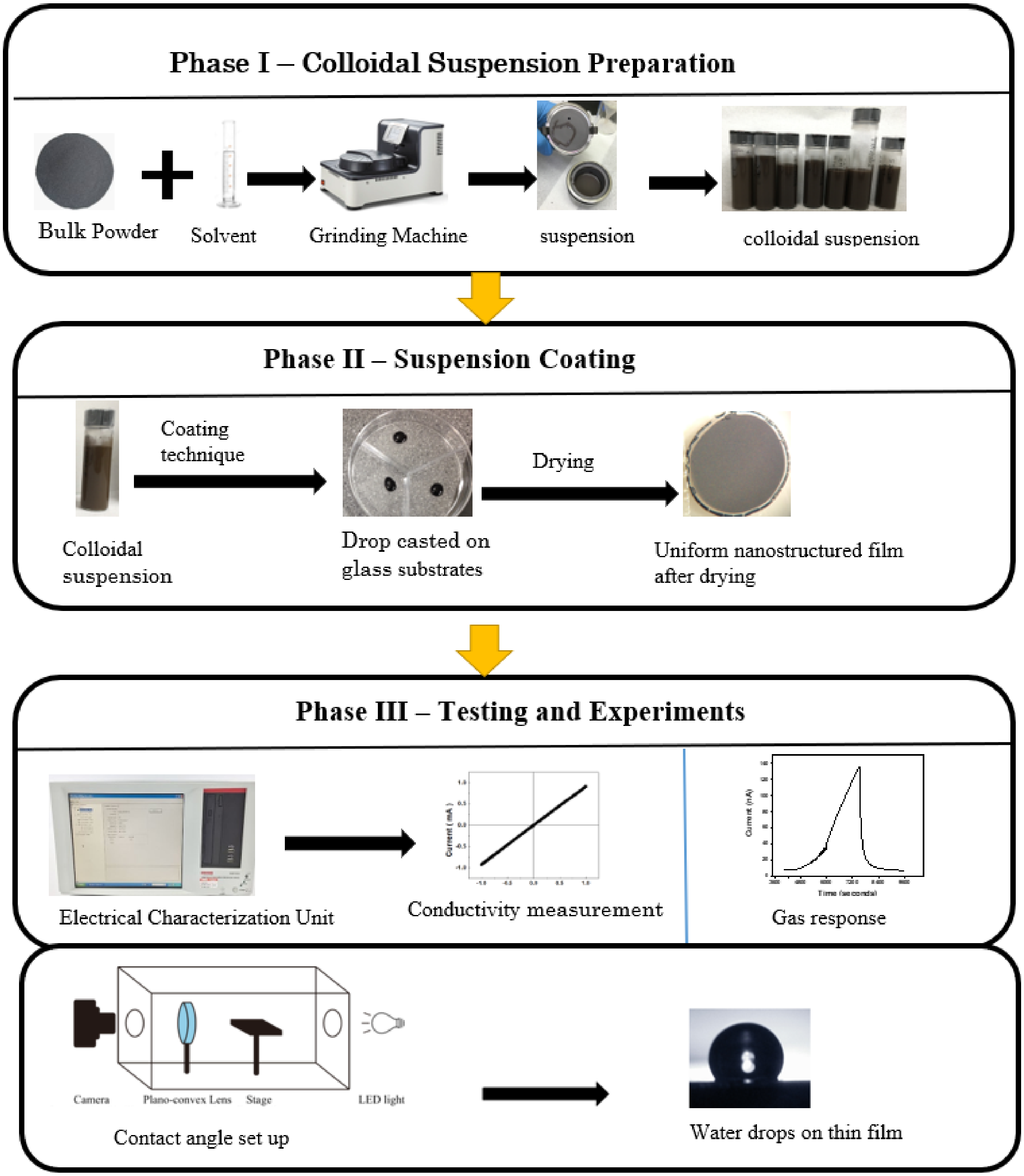

Figure 1. 25. Schematic diagram showing the different phases followed during research work. Phase I: Fine colloidal suspension preparation process; Phase II: Uniform coating of nanostructured thin film using colloidal suspension; Phase III: Characterization and experiment performed for freshly prepared nanostructured film.

1.4. Thesis Organization and Contributions

This thesis presents results on the fabrication and multifunctional behavior of thin films prepared from the colloidal grinding or PBM technique. The outline of the thesis is as follows:

The entire thesis consists of 5 chapters – The current chapter introduces general background on the evolution and development of various nanodevices and nanomaterials. Chapter 2 provides an in-depth description of the nanoscale grinding procedure for thin film preparation. Additionally, this chapter also includes different characterization and analysis techniques used for investigating the produced thin films. Chapter 3 focuses on the fabrication and experimental results of thin film structures, with results related to achieving tunable wettability and electrical properties. The tunable wettability properties are explained based on contact angle measurement, and precise electrical transport measurement of thin films demonstrate the tunable electrical resistivity behaviour. Furthermore, this chapter includes the effect of annealing conditions (time/temperature) on the wettability and electrical conductivity properties of different ground films coated on various rigid substrates. Chapter 4 introduces the gas sensor fabrication process from ZnO nanoink suspensions and investigates the gas sensing properties of the resulting nanostructured ZnO thin film devices. The sensors were exposed to different gaseous species, humidity and temperature and their response is measured. Also in this chapter, the influence of different grinding condition on the gas sensing parameters is provided. Lastly, chapter 5 summarizes the thesis and details potential extensions, including preliminary experimental work that was performed, and concludes by providing future directions for this ongoing research.

Journal Publications and Conferences Resulting from this Thesis:

[J1] R. Sapkota, P. Duan, T. Kumar, A. Venkataraman, and C. Papadopoulos, “Thin film gas sensors based on planetary ball-milled zinc oxide Nanoinks: Effect of milling parameters on sensing performance,” *Applied Sciences*, vol. 11, no. 20, p. 9676, 2021.

- Author was responsible for Conceptualization, Methodology, Investigation, and writing- original draft preparation.

[J2] R. Sapkota, J. Zou, S. Dawka, J. E. Bobak, and C. Papadopoulos, “Multi-functional thin film coatings formed via nanogrinding,” *Applied Nanoscience*, vol. 8, no. 6, pp. 1437–1444, 2018.

- Author was responsible for Conceptualization, Methodology, wettability and electrical measurement, and writing-original draft preparation.

[C1] S. Dawka, P. Duan, R. Sapkota, C. Papadopoulos, "Thin Film Photodetectors based on Zinc Oxide Nanoinks", 2022 *Electrochemical Society Spring Meeting*, Vancouver, 2022.

[C2] R. Sapkota and Chris Papadopoulos “Properties and applications of nanostructured thin films formed via nanoscale grinding”, *EMN Greece Meeting*, 2018

[C3] R. Sapkota and Chris Papadopoulos “Multi-functional Thin Film Coatings formed via Nanoscale Grinding”, Pacific *Rim Symposium on Surfaces, Coatings and Interfaces*, Hawaii, 2016.

[C4] R. Sapkota and Chris Papadopoulos “Tuning Contact Angle of Thin Film Coatings via Nanoscale Grinding”, in *Pacific Centre for Advanced Materials and Micro-structures Meeting (PCAMM)*, UBC, 2016.

Chapter 2

2. Fabrication and Experimental Setup

Sahil Dawka [101], *Xue Cai* [102] *and Jinxiang Zou assisted with some results shown in this chapter: Sahil Dawka (MEng graduate student) and Jinxiang Zou (MITACS Globalink Program) helped to prepare drop-casted nanostructured films. For the doctor blading coating technique, Pengjun Duan* [103] *(MEng graduate student) and Tanay Kumar (MITACS Globalink Program) helped create nanostructured thin films using the doctor blading technique. Pengjun Duan assisted the author with the characterization (SEM, AFM, Raman, PL, EDX) of ZnO films. The author worked on preparing thin films for wettability, conductivity and gas sensor experiments. The author also worked on measuring contact angle, electrical measurement of different nanostructured thin films.*

This chapter introduces the characteristics of the materials, grinding machine procedures, coating techniques and film treatment processes used in this work. We also briefly describe the equipment and setup for the different thin film characterization experiments and various analysis techniques for the nanostructured films.

2.1. Fabrication of nanostructured films

2.1.1. Materials

We have used silicon (Si), titanium disilicide ($TiSi_2$) and zinc oxide (ZnO) as the raw materials for grinding purposes during our research. After grinding, these materials turn into finer particles, later coated onto various substrates to examine the film properties. The description of each material is discussed below:

i. Silicon (Si)

Silicon, a group IVA element, is the most commonly occurring element on the earth after oxygen. Its crystal is in a diamond structure on a face-centered cubic crystal lattice. Each silicon atom is surrounded by four nearest-neighbor atoms forming a tetrahedron. Thus, the basis of the diamond structure comprises two atoms with coordinates (0, 0, 0) and $a_o/4$ (1, 1, 1), as seen in ***Figure 2.1.*** The silicon atom falls under Fd3m space group and has a lattice parameter of 0.543 nm [104]. Other solids that can crystallize in the diamond structure are C, Ge and Sn.

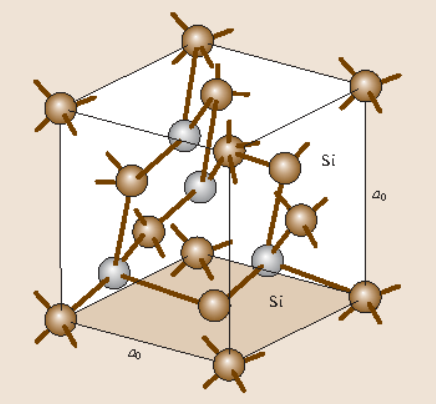

Figure 2.1. Diamond crystal Structure of Si. (Adapted from [104]).

Semiconductors absorb the light frequency range with the quantum energy equal to or larger than the width of its bandgap. In indirect band gap semiconductors such as Si, an electron cannot be excited from the top of the valance band to the bottom of the conduction band only by photon absorption. The electron' momentum undergoes a major change, which can only occur when it interacts with lattice vibrations or phonons. To conserve both momentum and energy, phonon absorption or emission must occur.

ii. Titanium Disilicide ($TiSi_2$)

Metallic silicide nanoparticles are the preferred silicide material for ICs since their growth is easily compatible with silicon processing technology. Among metal silicides, $TiSi_2$ is well known for its excellent electrical properties (high electrical conductivity) and thermal stability [105]. These properties of $TiSi_2$ have served in electrical interconnections in ICs for over two decades.

$TiSi_2$ crystal structure comprises two competing crystalline structures: C54 and C49 phase. The C54 phase is the most stable structure with low resistivity (13-20 μΩ cm), making them suitable for IC applications. Similarly, C49 appears in the metastable phase and has high resistivity (80-100 μΩ cm) [106]. At the medium thermal annealing (450 - 650^0 C) process, the metastable phase occurs, and at high temperature (> 700^0 C), the C54 phase becomes most stable [107]. The C54 phase has a face-centered orthorhombic structure (space group Fddd), arranged by ABCD stacking planes with quasihexagonal structure. Their lattice constant are a = 8.27 Å, b = 4.80 Å, c = 8.55 Å [108]. The primitive cell consists of two titanium atoms and four silicon atoms for a total volume equal to $\frac{abc}{4}$. Each Ti atom has ten Si neighbors, placed in a shell between 2.55 Å and 2.78 Å, where six are located on the same xy plane and form a hexagon with Ti site as the center, and the remaining four are arranged in a nearly tetrahedral arrangement [109]. Similarly, the second shell of the neighbor consists of four Ti atoms. Also, in the first shell of neighbor around Si atoms, five Si and five Ti atoms are distributed, and the second neighbors with four Si atoms. Therefore, in most silicon-rich silicides, Si atoms are first neighbors, and hence the Si self-diffusion by hopping is more efficient than Ti hopping [109].

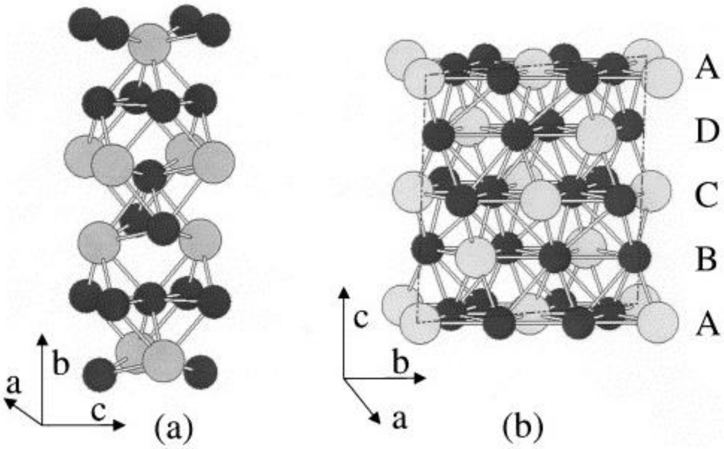

Figure 2.2. Units' cells of the two common phases of TiSi$_2$ with Ti atoms shown in light and Si atoms in dark. (a) C49 phase where the unit cell consists of four Ti atoms and eight Si atoms. (b) C54 phase where the unit cell contains 8 Ti atoms and 16 Si atoms, arranged in four planes, each plane containing hexagonal atomic sheet. (Adapted from [110]).

Similarly, C49 is a base-centered orthorhombic structure with a different stacking arrangement. The lattice parameter of this structure reported by Pearson (a = 3.62 Å, b = 13.76 Å, c = 3.6 Å), shows 6% larger volume than C54 [111]. The primitive cell of the C49 crystal structure contains two Si Sites [112]. One Si site is in the form of a two-dimensional hexagonal sheet, while other Si site for Zigzag chain. Notably, the C49 structure is heavily faulted, i.e., planes are frequently mis-stacked, thus causing an increase in its high resistivity [113]. Nevertheless, the C49 structure turns out to be less symmetric and more open than the C54 phase.

iii. Zinc Oxide (ZnO)

ZnO is an II-VI compound semiconductor with a wide band in the UV spectrum, making this material attractive for optoelectronic applications [114]. At room temperature, the direct bandgap is about 3.37 eV, and large exciton binding energy (60 meV) that allows it to be used in the electronic emission processes both at room and higher temperature, so it is considered a better material for fabricating optical devices [115]. Similarly, the hexagonal structure of ZnO consists of low symmetry and large electromechanical coupling, which show strong piezoelectric and pyroelectric properties. Likewise, native defects and impurities have advanced their gas sensing and luminescence properties [114,116].

The crystal structures of ZnO are wurtzite, zinc blende and rocksalt, as schematically shown in ***Figure 2.3*** [117]. Under ambient conditions, the thermodynamically stable phase is wurtzite symmetry. The zinc blende can only be stabilized when grown on cubic substrates whereas, high pressure is used to obtain a rocksalt structure [117].

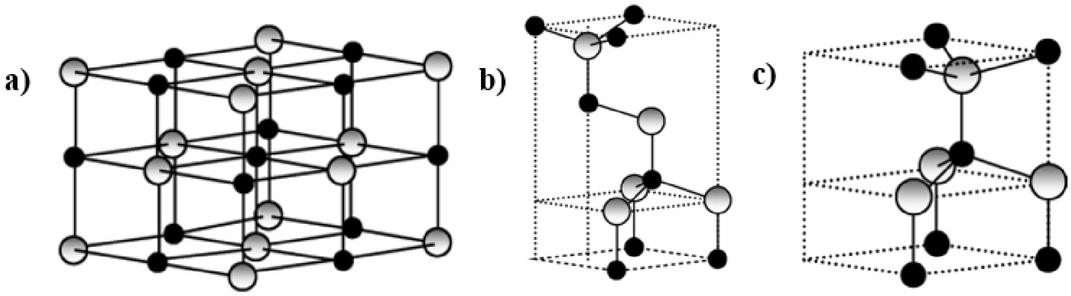

Figure 2.3. Stick and ball representation of ZnO crystal structures: (a) cubic rocksalt (b) Zinc blende and (c) Hexagonal wurtzite. Shaded grey and black spheres represents Zn and O atoms, respectively. (Adapted from [117]).

The wurtzite structure has a hexagonal unit cell (space group *P6₃mc*) with two lattice parameters *a* and *c* in the ratio of $c/a = \sqrt{8/3} = 1.633$ (in an ideal wurtzite structure) [117]. Generally, the wurtzite structure represents several alternating planes composed of tetrahedrally coordinated Zn^{2+} and O^{2-} ions and stacked alternatively along the c-axis. The tetrahedral coordination in ZnO forms a non-central symmetric structure with polar symmetry along the hexagonal axis [118]. Such structure formation on ZnO induces piezoelectricity properties and spontaneous polarization and plays a key role in crystal growth, etching and defect generation. The wurtzite structure of ZnO is present in the bulk crystal [119] and can also be fabricated easily in various nanostructured morphologies such as nanorods, nanowires, nanorings, tetrapods and nanoparticles. Most importantly, ZnO comprised abundant materials such as zinc and oxygen. Hence, it is considered the cheapest semiconductor material.

To date, several theoretical approaches have been used to calculate the band structure of Wurtzite ZnO. An example of one the approach is shown in the ***Figure 2. 4***, where the local density approximation (LDA) method is used by incorporating atomic self-interaction corrected pseudopotentials (SIC-PP), in which the Zn 3d electrons are considered to calculate the electronic structure of ZnO [120]. The results show that the valance band maxima and the lowest conduction band minima occur at the Γ point k=0, indicating that ZnO is a direct bandgap semiconductor. Also, the calculation results from the SIC-PP method show the bottom 10 bands that correspond to Zn 3d levels. The following 6 bands from -5 eV to 0 eV is related to O 2p bonding states. The first two conduction band states are firmly Zn localized and correspond to empty Zn 3s levels. The bandgap determined using this calculation is around 3.77 eV and is in good correlation with the experimental value of 3.4 eV, which was calculated using the standard LDA method.

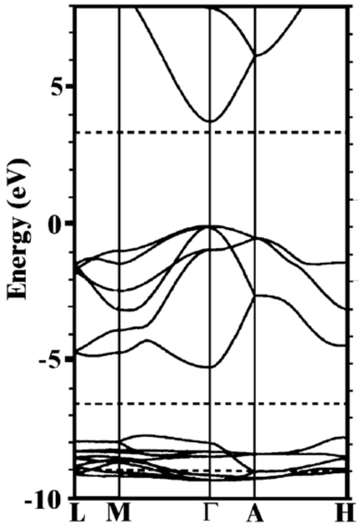

Figure 2. 4. The LDA band structure of bulk wurtzite ZnO calculated using an atomic self-interaction-corrected pseudopotentials (SIC-PP) method [120].

2.1.2. Planetary Ball Milling

For this research work, planetary ball mill (PBM) [57] was chosen as a preferred nanogrinding technique. PBM was selected because they are suitable for both wet and dry, fine and ultra-fine grinding of coarse particles down to the nanometer size. Furthermore, they were also among the most chosen nanogrinding methods in the laboratory for good reproducibility, comparatively short processing time and safe handling [121]. PBM has thus been a useful method for preparing materials for various applications in industry [121].

Planetary ball milling techniques are beneficial for chemical, pharmaceutical and food industries, where obtaining finer particle sizes is very important for shaping final products. Apart from finer particle size, high-energy ball milling can also alter the chemical structure inside the material through bond breaking and/or reforming. Hence, these techniques can produce nanostructures such as alloys, nanocrystalline powders, nanocomposite, amorphous materials [57].

Generally, the PBM chamber consists of two or four pots/jars (shown in ***Figure 2. 5 b)***. The grinding pots are attached to the planetary disk, which rotates around a common central axis, and at the same time, pots also rotate around on their axis. The high revolution and rotational speed produced by the disk and jar generates large impact energies of milling balls; thus, making grinding more effective. Also, the chosen milling balls for grinding are commonly rigid and comparatively inert materials.

Figure 2. 5. (a) Fritsch Pulverisette 7 Micro Mill premium line. (b) Grinding jar (c) Overall layout of planetary disk of Fritsch Pulverisette 7.

The speed of grinding balls' is influenced by both revolution and rotational speed and the charge on the powder. Similarly, the action of grinding beads also affects the number of collisions, the ball velocity, and final energy dissipation [122]. Furthermore, the motion of balls inside the grinding jars is complex and is directly related to operation parameters. As seen in ***Figure 2.6***, as the filling rate and/or the revolution speed increases, the motion pattern of the ball changes from cascading to cataracting to rolling [123]. In the cascading regime, the milling balls move along the wall of the grinding container to the top of bulk material, from where they fall to the bottom of each other. Similarly, in the rolling or centrifuging ball regime, the balls adhere to the wall of the grinding jar with almost no relative velocity. Likewise, in cataracting regime, the balls travel up on the walls and then detach with high intensity to impact the rest of the bulk or the opposite wall [121]. In general, cataracting regime is preferred over a rolling regime to get the highest efficiency from the operating energy of the PBM [121].

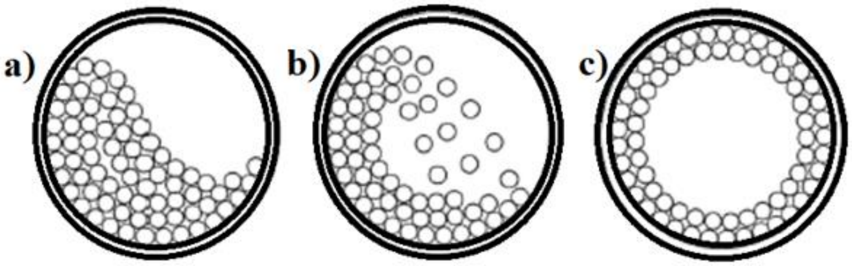

Figure 2.6. Motion of grinding beads: (a) Cascading (b) Cataracting (c) Rolling. (Adapted from [123]).

It is also claimed that, the counter direction of rotation to revolution results in higher impact energies in the ball compared to the normal direction [123]. Also, selecting suitable milling balls reduce unnecessary side reactions or high abrasion [124]. To achieve higher impact energy from beads, one should choose balls with high density or large diameter [121], which ultimately creates finer particles with large surface areas. However, ball material are also beneficial at lower impact energy for efficient mixing and/or longer grinding conditions [121]. Also, larger/fewer number of balls and/or mixtures of random sizes balls are not recommended by mill manufacturer because those can affect the reaction and cause abrasion [124–126]. Yet, if the mass of milling beads is constant, and thus, the filling ratio remains constant, then the yield product stays unchanged independent from ball diameter [121].

Other important factors affecting the grinding process are the presence or absence of a solvent, termed as wet or dry grinding, respectively. On the one hand, in dry grinding, powder of one or more materials is placed in the grinding container together with grinding balls. The use of more than one material in the dry grinding process will lead to the formation of alloy [127]. Also, particle breakdown into finer sizes is possible in dry grinding due to the impact energy of beads transferred directly onto the powder. On the other hand, in the wet grinding process, milling is done in the presence of a solvent, which has several benefits such as superior heat dissipation, improved homogeneity, easier withdrawal of the ground material, and surpassing of ground particles to mitigate agglomeration [128]. However, one disadvantage of wet milling is unpredictable reaction occurs during the grinding process, which leads to poor functionalization on particle's surface [128]. The surface chemistry of such a coating can be characterized using X-ray photoelectron spectroscopy (XPS) and Raman spectroscopy.

The major drawbacks of both types of milling are contamination and wear during the grinding process [121]. The collision of the ball against each other and the grinding jar's wall during the grinding process will result from wearing the jar and the beads. The displaced materials get combined into the powder, where it contaminates or alters the powder chemistry. Some authors have experimentally studied the wear rate constant of the dislodged material. Their result shows that the increase in wear rate is linearly dependent on the revolution speed of the grinding mill and is mainly independent of milling time [129]. Similarly, contamination can be minimized by using the same material as the milling jars and milling beads as feed material to avoid cross-contamination. Yet, the changing chemistry of the resultant powder remains a concern [121].

2.1.2.1. Milling process

The grinding process is carried out on the milling chamber, which consists of milling jars. Principally, all jars inside the chamber could also be used for milling purpose if their weight remains the same. However, some milling container/s could also be used as a counterweight if all milling jars are not filled with ground materials. Both the grinding jar and counterweight jar should match their weight on the mechanical dial scale, as an imbalance in weight could cause an accident during the grinding process.

Inside the empty grinding jar, beads were filled first, followed by the powder to be ground and then the solvent. Precaution should be taken while handling the milling jar. While closing, the pots were tightly interlocked on their handle and afterwards sealed using parafilm. Next, the grinding condition in PBM was programmed, and milling was performed. Pause time was also set during grinding duration. Rest time was essential because heat was rapidly generated due to the friction caused inside the grinding chamber. After each pause time, leakage was checked, and pressure was released from the pot. During the grinding process, the powder and solvent react with each other, and pressure gets build-up, so evacuating pressure from the jar during rest time prevents explosion or damage to the machine. Also, increasing the rest time and grinding cycle is recommended if the grinding condition is set at higher grinding speeds and/or longer grinding time.

2.1.2.2. Extraction process

Once the grinding cycle completes, using the special empty device, we extract the ground suspension. Before extraction, one should check the jar temperature and pressure. Particularly for this kind of PBM machine, the manufacturer provides a special emptying device. The device consists of a syringe pump tip, funnel lid, two seals, two stainless steel strainers, adapter and O-rings. After removing the handle of the grinding bowl, O-ring was placed on top of the grinding jar and later fitted with the adapter, thin seal, two stainless steel strainers and thick seal, respectively. The two strainers consist of a mesh of 0.08 mm and 0.8 mm in width. The smaller mesh was placed towards the funnel lid side so particles less than 80 µm gets extracted. After the syringe got screwed on the funnel lid, the jar containing suspension was made upside down and shook vertically so that all materials got dislodged from the bottom of the jar. The syringe filled with suspension and air was pumped 2-5 times and was extracted. The first extraction could not remove all the materials, so additional solvent was injected into an emptied syringe and transferred to a grinding jar. The process was repeated 5 to 7 times. Each extraction from the syringe was stored in different vials. Each vial contained decreasing solid particle concentration and was labelled accordingly.

Figure 2.7. Steps for extraction (a) shaking bowl containing suspension vertically for 3-5 times (b) Pull-push suspension containing syringe for 2-5 times (c) extract suspension slowly from grinding bowl.

Figure 2.8 shows the grinding experiment of one of our trials. The material was ZnO ground in DI solvent at 200 rpm for 60 minutes (consists of 12 cycles where each cycle has 5-minute grinding time and 5 minutes rest time).

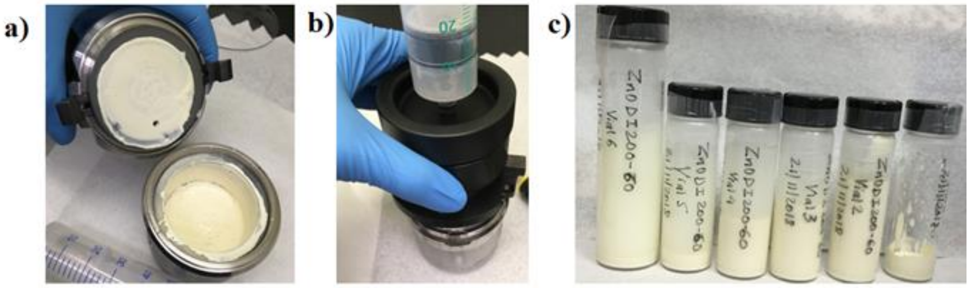

Figure 2.8. (a) ZnO material after completion of grinding cycle (b) Extraction equipment attached on grinding bowl (c) The suspension's extraction steps followed, as shown in **Figure 2.7**, and different suspension densities (right to the left shows decreased density order) are extracted.

Special attention should be given while cleaning the O-ring, mesh and grinding bowl container. Sometimes ground materials were stuck on the grinding jar components, and in such a case, light sonication in water or IPA solution would be helpful.

2.1.3. Film Coating/Casting Techniques

After creation of the nanoparticle suspensions, the next step is to create thin films from the slurry. We have chosen the solution coating/casting technique because the solution is directly transferred to the substrate. The three different deposition techniques used for this research are explained in brief in the following sections.

i. Drop Casting

This technique involves placing liquid drops of desired material onto the surface of the substrate and subsequently allowing the solvent to evaporate [130]. This method is straightforward, low cost and waste less material. The film thickness and properties depend on the volume of dispersion and concentration. Generally, the substrate is heated to speed up the evaporation process and/or improve film morphology. Difficulties in film formation are some disadvantages of this method.

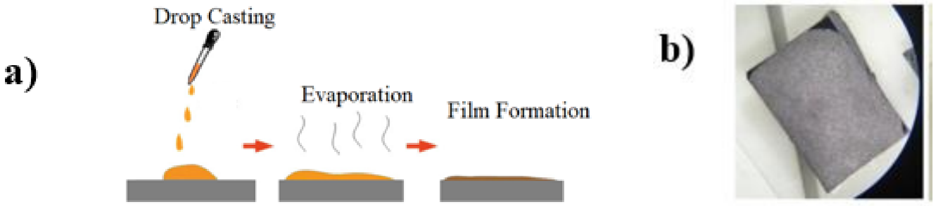

Figure 2.9. (a) Suspension deposited using drop casting. (b) Ground suspension ($TiSi_2$ powder ground at 400 rpm in EG solvent for 10 minutes.) coated on SiO_2/Si substrate.

In our research, we have prepared most of our silicon and titanium disilicide films using the drop-casting technique on both flexible and rigid substrates. We have used both micropipette and disposal pipette for the extraction of suspension. The films prepared using EG/DI solvent is dried in an oven/hot plate, whereas films ground using IPA are dried at room temperature.

ii. Doctor Blading

Doctor blade or tape casting is another frequently used technique to fabricate the thin film on large-area surfaces. In this process, a slurry containing nanomaterials are placed on a substrate beyond the blade. When a constant relative movement between the blade and substrate is achieved, the slurry spreads on the substrate forming a thin sheet of layer [131]. This technique has been used for creating film thicknesses from twenty to several hundred microns. Some advantages of this method are a fast and efficient process for making uniform film layer, less solution wastage, producing films from solutions with a wide range of viscosities, coating rigid or flexible substrates, and delivering high throughput.

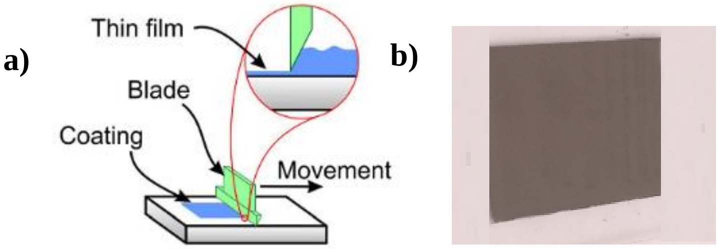

Figure 2.10. (a) The mechanism of doctor blade method [132] (b) Doctor blading of ground $TiSi_2$ films (suspension prepared in EG solvent at 400 rpm for 60 minutes) on glass substrates.

In our research, we have prepared most of the ZnO film using a doctor blading technique. Before, creating the uniform nanostructured film, we first used scotch tape to make casting surfaces on the thick glass substrate. The tape is masked on the substrate in such a way that it adheres well to the substrate without bubbles. The thickness of the nanostructured film is controlled based on the scotch tape thickness (approx. 60 µm). Then, we drop around 5 µL of colloidal suspension of ZnO nanoparticles (suspension is first centrifuged and supernatant is removed to control the particle concentration) on one end of the substrate. Using the razor blade, the suspension is dragged towards the other end of the substrate and leave the sample for drying on the hot plate (100 ^{0}C) for 5 minutes. Later, scotch tape was carefully removed, and electrical contact regions were created.

iii. Dip Coating

Dip coating refers, dipping a substrate into a liquid coating, removing the substrate from the liquid, and draining the excess liquid. In this method, the film is formed on the surface of the substrate after the suspension is evaporated. The film thickness varies by altering various parameters (the rate at which the substrate is immersed and removed from the liquid, the immersion time, the liquid and substrate intrinsic properties and the number of immersion processes). Some ground suspension of $TiSi_2$ trials were tested using this method.

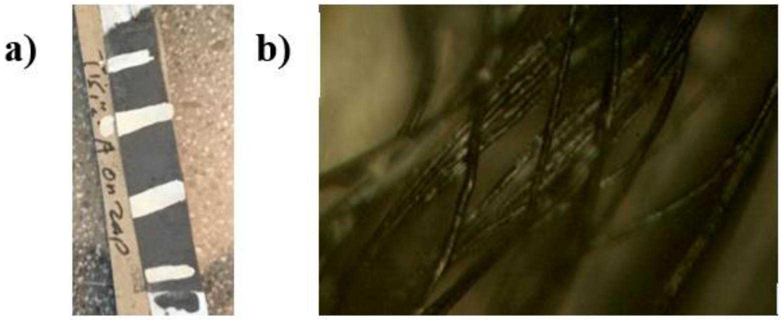

Figure 2.11. (a) Dip coating of paper substrate on $TiSi_2$ suspension (powder ground at 400 rpm for 10 minutes in EG solvent) (b) Optical image of dip coated cotton thread using $TiSi_2$ suspension (powder ground at 400 rpm for 60 minutes in EG solvent).

2.1.4. Film Treatment

After deposition or casting, the thin film undergoes a thermal treatment process, i.e., drying or annealing process. The film treatment for most of our nanostructured thin film was done by drying them in a mechanical convection oven or hot plate. The film treatment time depends upon the suspension's volume, solvent type and temperature used for drying. For annealing process, a chemical vapor deposition tube furnace (first nano Easy Tube 2000 3-Zone system) was used. The tube furnace consists of a quartz tube (3 x 40-in.), quartz loader holding samples, heating elements and a metallic shield.

2.2. Experimental Set-up

This thesis mainly focuses on three different application areas of a prepared film, and their experimental setup was designed accordingly. The first part of the experiment involves the drop-casting technique for preparing a thin film. The prepared film's wettability behavior on a glass was investigated. Later, more tests were done in other flexible and rigid substrates. Besides this, the conductivity test of those samples was also done. In the second part, we continue preparing the films with both drop-casting and doctor blading processes. The often-used trials in the second part are ZnO materials; however, some adhesion test using doctor blading technique was done for silicon and $TiSi_2$ samples as well. In the following section, brief literature about different application and experiment set up arranged in the lab will be explained.

2.2.1. Wettability and Contact Angle

The wettability of a surface or material is determined by the contact angle of liquid formed onto the substrate surface. The ability of the liquid to spread on deposited solid (or liquid) substrate refers to wetting. Therefore, when a liquid is dropped on the substrate surface, the two-surface form an angle (contact angle), which is an angle tangent to the liquid surface made with the substrate. This angle determines the wetting tendency of the nanostructured surface. Hence, a wetting liquid forms a contact angle less than 90^0 with the substrate surface, whereas a non-wetting liquid forms an angle between 90^0 and 180^0.

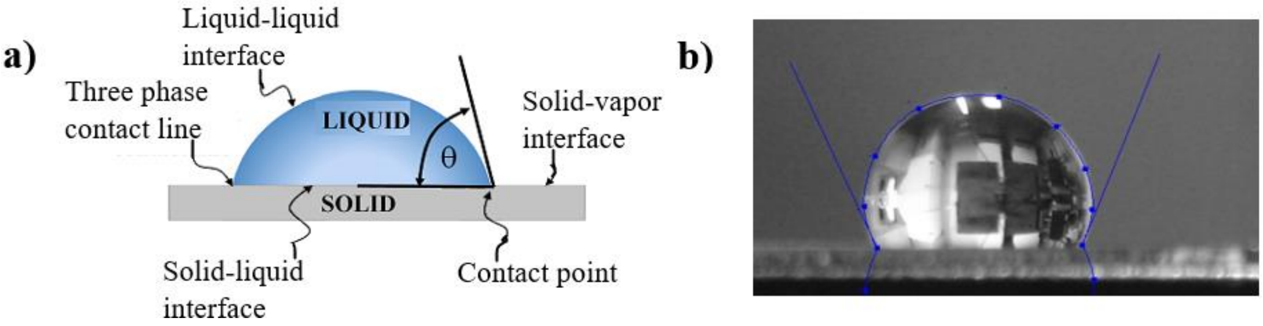

Figure 2.12. (a) Drop showing the three-phase contact point at the solid/liquid/gas interface. (b) Contact angle ($114.1^0 \pm 0.3^0$) of DI water on ground silicon coated on thin glass substrate using the drop-casting method.

On plane surfaces, the dropped liquid experiences two forces: adhesive and cohesive. The adhesive force between the solid and liquid favors spreading, whereas cohesive forces within the liquid counteract the spreading. The balance between both forces determines the contact angle of the liquid on the surface [133]. Generally, the interaction and repulsion forces between solid and liquid and the three-phase interface properties (gas, liquid and solid) indicate the actual degree of contact angle. The lower the contact angle, it means that cohesion forces are weaker than the adhesive forces. For this phenomenon, the molecules of the liquids tend to interact with solid molecules than liquid molecules. Similarly, a higher contact angle is formed when cohesive forces get stronger than adhesive forces, and fluids interact with each other rather than with solid surfaces.

There are only a few entirely flat surfaces. Surface roughness is considered as one of the vital parameters to determine the contact angle between the rough surfaces. There are two widely followed models: the Wenzel and the Cassie-Baxter models, which explicitly indicate the influence of roughness on the wettability characteristic. Wenzel’s model suggests that if a liquid interacts with the rough surfaces, then the effect of roughness wets the entire surface. On the other hand, the Cassie-Baxter model assumes the liquid droplet partially wets the surface due to air pockets between roughness structures. The apparent contact angle of a liquid droplet in the Wenzel state [134] is given by

$$cos\theta = \boldsymbol{r}\, cos\theta_{\mathrm{Y}} \qquad (1)$$

Where '$\mathbf{r}$' is the roughness factor, defined as the ratio between the actual surface area and the geometric projected area of the rough surfaces and θ_{Y} is Young's contact angle (the equilibrium contact angle on smooth surfaces). Since '$\mathbf{r}$' is always greater than unity, this model explains that surface roughness improves the hydrophobicity of inherently hydrophobic surfaces ($\theta_{\mathrm{Y}} > 90^0$). In contrast, hydrophilic surfaces become more hydrophilic with increasing surface roughness.

Likewise, the Cassie and Baxter model [135] mainly emphasizes porous structure and identifies the contact angle formed on those surfaces. This model explains that the liquid drop on top of the absorbent structure creates a liquid surface interface as a composite interface due to air pockets between the roughness. And so, the apparent contact angle is determined by the energetics of the contact area underneath liquid, where the fraction of solid and air area are present [136]. Hence, contact angle, in which one of the components is air (i.e., $\cos(180^0) = -1$) becomes,

$$cos\theta = \boldsymbol{f}. cos\theta_Y + (\boldsymbol{f} - 1) \qquad (2)$$

Where 'θ' is the contact angle and '$\boldsymbol{f}$' is the solid-area fraction, and 'θ_{Y}' is the contact angle of the smooth surface.

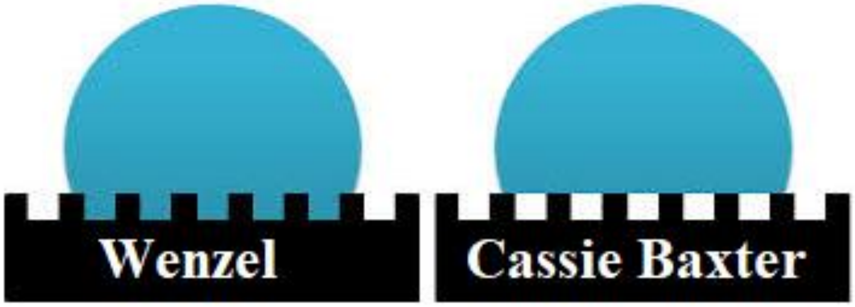

Figure 2.13. Wenzel’s model- wetted contact between the liquid and the rough substrate. Cassie’s model- non-wetted contact between the liquid and the rough surface.

We built a contact angle set up to measure a different ground film coated on various substrates for our wettability experiment. The ground suspension stored in the vial was sonicated, shook and re-sonicated, and finally drop cast with the appropriate volume on a substrate. The colloidal suspension was then dried at a reasonable temperature, and the contact angle was measured.

For the contact angle set up, the apparatus used were the plano-convex lens, stage, light source, and camera. The camera, lens and stage were aligned together, so that clear image of the drop was captured. At first, nanostructured thin film was placed onto the stage from the opening present just above the stage. After the light source is switched on, we then place the 3 µL of DI water drop onto the film surface using a micropipette. The lid of the enclosed chamber is closed, and the water drop image is captured within 10-15 seconds. At least 5-7 images of the drop were taken from each film. If the film is large (some films spread more on the substrate e.g., IPA ground nanoparticles) then we try to drop DI water on other sides of the film as well and retake the images. However, for smaller size films, we repeat the measurement on multiple new films that were prepared at the same time from respective suspensions. For CA measurement, we prepared at least

3 – 5 samples and 6 – 8 samples for spreading and non-spreading films, respectively. So, each measurement of respective trials consists of at least eight to twelve CA data. Later, we average the contact angle measured on the multiple films of same grinding condition trials.

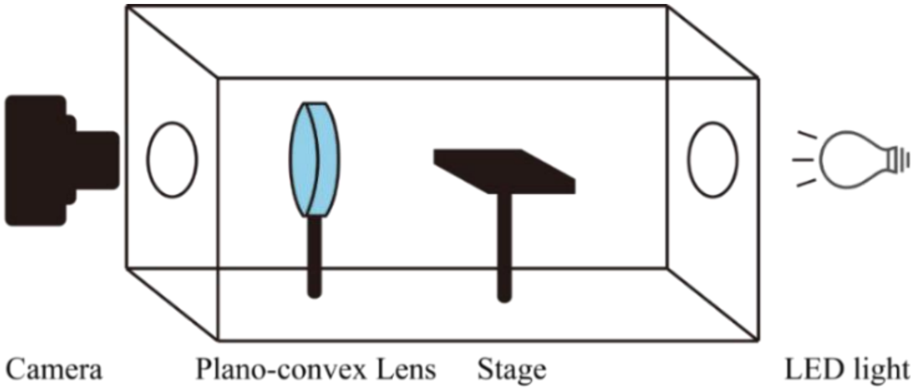

Figure 2.14. Schematic illustration of setup for contact angle measurement. Camera (Canon Power Shot SX410IS) and backlight are mounted outside the metal enclosure, whereas lens (Thorlabs LA1131C) and stage (Thorlabs MS1) are mounted inside the metal enclosure.

2.2.2. Conductivity

The electrical transport on the nanostructured materials varies from their bulk counterpart due to the increase of interface atoms and shrinkage of defects at/or near the grain boundary. The electrical conductivity of nanostructured materials is influenced by the action of charge carriers, where movement depends on grain size, type of materials (metals, insulator or composite), defects and doped impurities [137]. Semiconductors such as Si can enhance electrical conductivity through a doping mechanism [138]. $TiSi_2$, on the other hand, has low resistivity, good thermal stability and self-alignment with silicon. These properties make $TiSi_2$ the most attractive silicide in the semiconductor industry [105,139–141].

For our conductivity measurement, we fabricate the two-terminal thin films device, similar as shown in ***Figure 2.15***. The ground suspension was drop cast/doctor bladed on a different substrate and dried at the appropriate temperature. The suspension was sonicated and approximately 2 µL of suspension is drop casted onto the substrate. They are then dried at the appropriate temperature in a mechanical convection oven. After drying, silver paint on either side of the film was painted for creating contact regions and are further dried to remove the solvent from the silver paint. For electrical measurement, at least 3-5 different samples were prepared, and electrical resistivity of each trial was averaged. The experiments were carried out in ambient conditions and under room light. The electrical properties of samples are examined using a semiconductor characterization device in conjunction with the probe station. Tungsten probe tips of 1 µm nominal diameter were brought into contact with the silver electrode. For, *I-V* measurement one of the probe was set as electrical ground (source electrode) and the other is as input (drain electrode). The probe station and the microscope are connected to a digital display that helps position the electrodes at the exact location in the contact regions. The electrical characterization system used in this research can measure the current in the range of pico-amperes, with the resolution of a *femto-ampere* and accuracy of 0.1% or less. For all samples prepared for the conductivity measurement, voltage is passed across the two-terminal device and observed corresponding output. A specific sweep voltage range is selected.

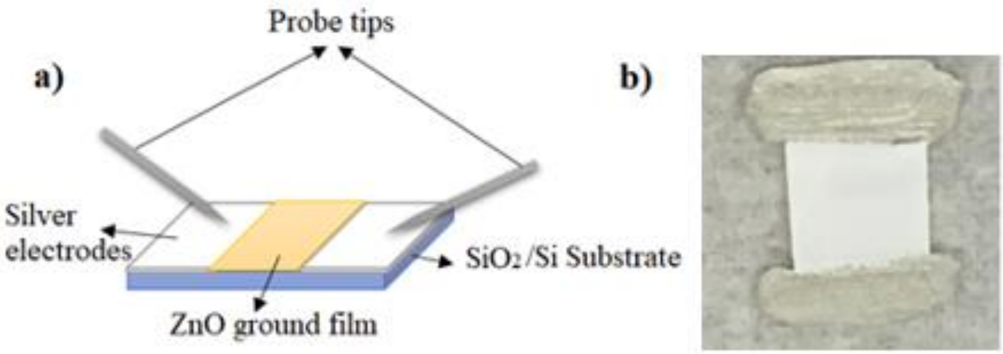

Figure 2.15. (a) Schematic illustration of electrical measurement set up in the lab. The two electrical probes from the Keithley 4200 SCS is applied in the silver contact region where constant voltage sweep is used, and the current response is recorded. (b) Ground ZnO film with a silver contact region that is prepared for electrical measurement.

2.2.3. Gas sensitivity

A chemical sensor is a device that converts the chemical information, ranging from concentration of particular sample components to total composition analysis, into an analytically valuable signal [142]. Generally, basic metal oxide gas sensors comprise a sensitive layer, a substrate, an electrode and a heater. The most attractive and frequently used device structure in gas sensing applications is the planar device structure (shown in ***Figure 2.16***). Similar device was fabricated for our experiment purpose. The main components of the planar sensor device are the sensitive layer (nanostructured film) and the contact electrodes that lie on the same plane. Mainly electrodes (e.g., gold (Au), platinum (Pt), Titanium (Ti) or aluminum (Al)) are normally inter-digitated and are embedded on top or at the bottom of the sensing layer. These electrodes can be active or passive. For measurement, voltage is applied between the electrodes and a current flowing through the device is calibrated in turns of change in resistance between the electrodes [143]. However, the reverse phenomenon, i.e., to feed current and measure voltage, is also possible.

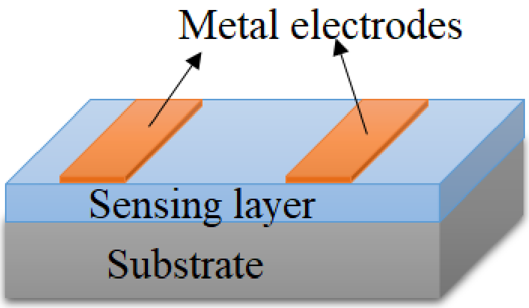

Figure 2.16. Schematic diagram of the planar/resistive gas sensor device structure.

Several works in the literature [76,144–164] have explained various gas sensing parameters such as response (R), response time (τ_{res}), recovery time (τ_{rec}), target gas concentration, operating temperature, humidity, sensitivity and detection limit, that has affected the sensor performance. All these gas sensing characteristics are described briefly in the section below

a) Gas response

The gas response is the ratio of resistance changes on the surface of the gas sensor before and after being exposed to the target gas. Different researchers have mathematically expressed responses in several forms [163,165]. Various approaches have been implemented to increase the sensor's response. Some methodologies, such as changing microstructure (grain-size) and porosity of metal oxide semiconductors, helps in improving the sensor's response [166]. The porosity in sensing film plays an important role in the sensor performance because it decides the rate of gas diffusion [166]. Likewise, smaller particles stay in compact form during the coating process, and they also get easily congregate and grow up together during heat treatment. These behaviors of small nanoparticles can ultimately block the gas diffusion path and reduce sensing response [167]. However, the addition of dopants or impurities can enhance the sensor's response [168].

b) Response time and Recovery time

Response time is when the sensor takes upon exposure to a target gas from the first reaction to the saturate value when the sensor reaches a particular percentage level (many reports represent 90% as response time, denoted as T_{90}) [169]. Further, lower the response time better is the sensing properties of the sensor. Also, higher concentrations of target gas give a shorter response time. Other parameters that affect sensor response time are gas flow rate and temperature. Similarly, recovery time is needed for the sensor to return to 10% of the original baseline when the test gas is removed, and the sensor is later cleaned with dry air [169]. To reuse the sensor short recovery time is required. An example, shown in ***Figure 2. 17***, is the one way of calculating response time and recovery time.

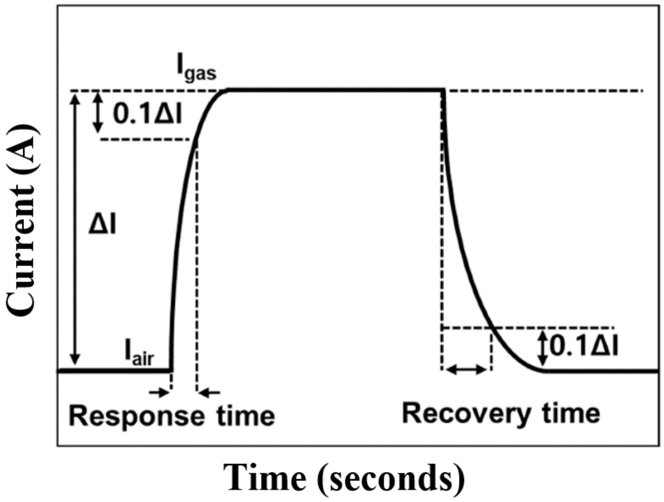

Figure 2. 17. Response and recovery time calculation at constant voltage bias mode. (Adapted from [165]).

c) Analyte concentration

The amount of target gas concentration used for gas sensing also affects the sensor's response. In most cases, gas sensor response increases with increased concentration amount. However, at some point, the response of the gas gets saturated and slower. Basically, at low target gas concentration, many reaction sites are available for chemical reaction, leading to fast response. But, at higher concentrations, the available reaction sites decrease, and response gets slower. Lastly, when a very large concentration of the analyte gas molecules is used, it can form multiple layers on the metal oxide surface, and thereby response gets saturated [161].

d) Working temperature

Temperature is another vital factor that alters the gas response. Therefore, a specific working temperature is assigned for a particular sensor type. Usually, the temperature that corresponds to the maximum gas response is known as working temperature. Most metal oxide gas sensors affected by temperature influence show similar gas response behavior as shown in ***Figure 4.9***. Generally, responses increase and reach their maximums at a precise temperature and then decrease gradually with increasing the temperature. With the temperature rise, it increases the average kinetic energy of the molecules, but to first order does not change the height of the barrier. So the reactants cross over the barrier more frequently and creates faster adsorption and desorption mechanism [170]. However, at very high temperatures, the adsorbed gas molecules may escape before the reaction resulting in a lower response [159]. Thus, finding an optimal working temperature is vital in achieving the maximum response of the metal oxide sensor.

e) Humidity

The performance of metal oxide sensors is also influenced by environmental humidity. Water adsorbing on the metal oxide surface will not donate the electron to the sensing layers; however, a reaction between the surface oxygen and water molecules conduces to a decrease in baseline resistance of the gas [171]. Secondly, the adsorption of water molecules leads to less chemisorption of oxygen species on metal oxide surfaces due to the decrease of surface area. Adsorption of water molecules displace oxygen molecules from the surface of nanoparticles, and electrons withdrawn from the ZnO conduction band is released back. This causes a reduction in the sensor resistance at higher humidity [171].

f) Sensitivity

Sensitivity is defined as the change of measured signal per analyte concentration unit. Usually, high sensitivity is preferred for thin-film sensors because it can measure the low concentration of the target gas. Calibration curves are used to recognize the instrumental response to an analyte and predict the concentration in an unknown sample. The calibration also determines the limit of detection and the limit of quantitation. The sensitivity is calculated from the calibration plots of relative response as a function of concentration and is determined as the derivate of the calibration plot in the working temperature. The unit of sensitivity is /ppm. The data fitting follows the power law as shown below

$$R = A\ x\ [C]^{B} \qquad (3)\ [172]$$

Where, A and B are the coefficients for the fit, and C is the gas concentration.

g) Selectivity

Preferential chemiresistive sensing performance for a specific type of gas by a sensor in the presence of another gas at the same operating conditions is called sensor's selectivity. The selectivity is measured in terms of selectivity coefficient/factor as a ratio of target gas to another gas. The general expression of the sensor's selectivity is expressed as [173],

$$Selectivity\ cofficient\ (K) = \frac{Selectivity\ of\ the\ sensor\ toward\ interface\ gas\ (S_A\ )}{Selectivity\ of\ the\ sensor\ toward\ interface\ gas(S_B)} \qquad (4)$$

Where, S_A and S_B are the responses of the sensor to a target gas A and an interference gas B, respectively.

h) Limit of detection (LOD)

There are several terms that have used for defining the limit of detection [174]. In general, the limit of detection, or called detection limit, is the lowest concentration of the analyte that can be detected by the sensor under the stated condition of the test.

$$LOD = 3xS.D/b \qquad (5)[172]$$

Where, 'S.D' is the standard deviation of the blank or is the standard deviation of the ordinate intercept of residual standard deviation of the linear regression, and 'b' is the slope of the calibrated line.

Some literature determine LOD, as the concentration that corresponds to the signal at three times the baseline noise [172]. The baseline signal is the one we get at zero analyte concentration. It basically quantifies the noise that is produced within the sensor environment.

i) Stability and Recyclability

The stability of a gas sensor refers to its ability to maintain its sensing performance repeatedly and even for long durations. This includes retaining the sensitivity, selectivity, and response and recovery time. The issue of low stability on metal oxide sensors will lead to uncertain results, false negative alarms and the need to frequently recalibrate or replace sensors. Generally, nanostructured materials with small grains suffer from degradation due to their high reactivity. There is no unified approach to increase the sensor stability; however, calcination, post-annealing treatment or reducing working temperature can increase stability up to a certain extend. However, doping metal oxides with metal nanoparticles or the synthesis of mixed oxides has also increased the sensor stability [144].

Flow rate conversion:

To calculate the concentration of the target gases, one should convert the unit of mass flow controller (MFCs) i.e., standard cubic centimeters per minute (SCCM) to parts per million (ppm). For this, first we convert the SCCM to atom/s for an ideal gas with the following equation:

$$1 \text{ sccm} = \frac{6.02214 \times 10^{23}\left[\frac{atoms}{mole}\right]}{2.2413\left[\frac{liters}{mole}\right]\times 10^{3}\left[\frac{cc}{liter}\right]\times 60\left[\frac{s}{min}\right]} = 4.4477962 \times 10^{17}\left[\frac{atoms}{s}\right] \quad (6)$$

Where, 6.02214 x 10^{23} atoms/mole is the Avogadro’s number, and 22.413996 is the molar volume of ideal gas at standard pressure and temperature.

Then, convert 100 sccm testing gas by equation below, since our testing chamber has the volume of 1 mole, the result $4.4477962 \times 10^{17}\left[\frac{atoms}{s}\right]$ is converted as

$$\frac{4.4477962\times 10^{17}\left[\frac{atoms}{mole}\right]\times 100\ sccm \times 60\ s}{6.02214\times 10^{23}\left[\frac{atoms}{mole}\right]}\ \text{x}\ 10^{6} \approx 5000\ \text{ppm} \qquad (7)$$

Where, the transit time inside the chamber is approximately 60 seconds.

<u>For pure gas flow (mg/L)</u>

For the pure gas flow incorporated in the chamber from flow controller, one can determine the concentration as,

$$\frac{Test\ gas\ flow\ \left(\frac{mg}{s}\right) x\ t}{Volume\ of\ chamber} \qquad (8)$$

Where ‘t’ is the transit time inside the chamber. Test gas flow is calculated in a similar way in [175].

2.3. Characterization techniques

The characterization of materials performed in our research involves phase analysis, compositional characterization, structural and surface characterization, which shows strong influences on the properties of the thin films. Below is a brief discussion on some of the techniques used during the research tenure.

2.3.1. Scanning Electron Microscopy (SEM)

The scanning electron microscope is the equipment used to observe the particle morphology at higher magnification, higher resolution and depth of focus compared to an optical microscope.

When an electron hits the atom, several interaction products are produced, and each product provides specific information about the sample. Scattering of an electron from the electrons of the atoms results in producing backscattered electrons and secondary electrons.

A beam of electrons is generally transferred from the electron source towards the specimen using positive electrical potential. The electron beam is confined and focused using metal apertures and magnetic lenses into a thin, focused, and monochromatic beam. Electrons in the beam interact with the specimen atoms, eliminating signal that consists of various information such as surface topography, composition and other electrical properties. These interactions and effects are detected and transformed into an image.

In this research, we have collected SEM images of the different ground thin films. The SEM images showed single distinguishable particles, and they seem to appear in quite irregular shapes. It was evident that the higher the grinding condition (time/speed), the more uniform was the particle size. Furthermore, solvent also played an essential role in creating uniform particles and reducing agglomeration. Also, other important information like porosity was extracted from SEM images.

2.3.2. Atomic Force Microscopy (AFM)

Atomic force microscopy (AFM) is a kind of scanning probe microscopy (SPM), where the probe is used to measure local properties (e.g., surface topography) of a thin film. The technique is used for investigating the various film properties of grains, phases, and surface layers in many materials such as ceramics, metals and polymers. Several imaging modes (contact, tapping and noncontact modes) are present, providing information about sample surfaces and detailed three-dimensional topographies. In this research, AFM tapping mode was used for capturing various ground film images. The images were captured using a Nanonics Multiview-1000 scanning probe microscope. Nanotec Electronica WSxM software was used for observing and analyzing AFM images.

Figure 2.18 (a) and (b) shows an example of AFM scanned images (left) and analyzed images (right) on WSxM software. The AFM images are imported into WSxM software, and profile locations are created (green line shown in images at the right) on 2D images. The measurement is done along horizontal, which is the length along with the profile (X [µm]) and towards vertical is the measured height (Z [µm]). It is observed that line profile heights range from approximately Z = 60 nm to 200 nm for 800a samples and Z = 100 nm to 300 nm for 200a samples. The results signify that particles in 200a samples are considerably larger than 800a samples. Another vital piece of information extracted from AFM images is the surface roughness of the thin film. We have analyzed the film roughness (shown in chapter 3 and 4) of $TiSi_2$ and ZnO samples.

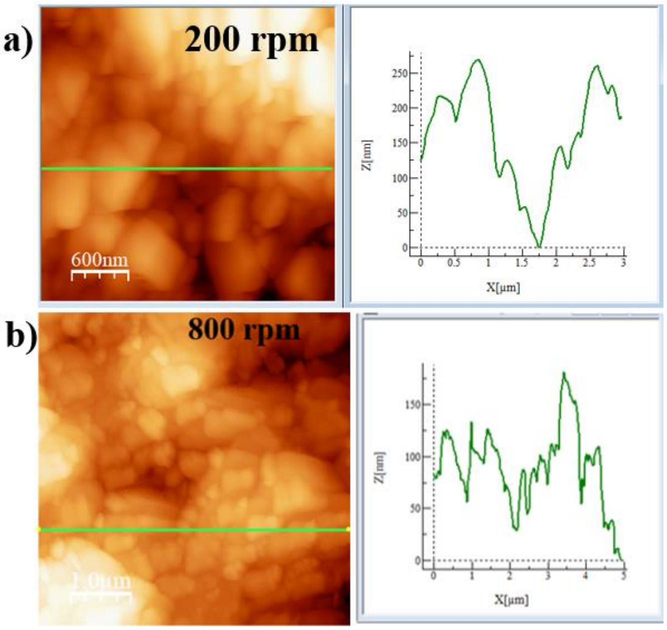

Figure 2.18. AFM scanned images of ZnO sample ground using EG solvent at constant grinding time for 10 minutes (a) ground at 200 rpm (200a sample) (b) ground at 800 rpm (800a sample) (c) 3D AFM image of 800a sample (d) cross-sectional line profile of 800a sample.

2.3.3. Raman Spectroscopy

Raman spectroscopy is a very useful technique in providing both chemical and structural information of the sample. This spectroscopy is an analytical technique where scattered light is used to measure a sample's vibrational energy modes. The interaction of light on a sample can cause elastic or inelastic scattering of light. Generally, elastic scattering occurs when the incident photon energy (Rayleigh) and scattered light have the same frequency, and therefore no energy is lost during this phenomenon. However, in inelastic scattering, the scattered light has lower or higher energy than the incident light. The scattered light with loss energy is called Stokes, and when the scattered light gains energy, they are called anti-Stokes. The types of interaction are most commonly represented by frequency or energy level and are shown in ***Figure 2.19***. The frequency of scattered light is represented as

$$\bar{\nu} = \frac{1}{\lambda_0} - \frac{1}{\lambda_v} \qquad (9)$$

Where λ_0 represents the wavelength of incident light and λ_v is the wavelength of the scattered light. The frequency of the scattered light is denoted in wavenumber units (cm^{-1}), by conversion.

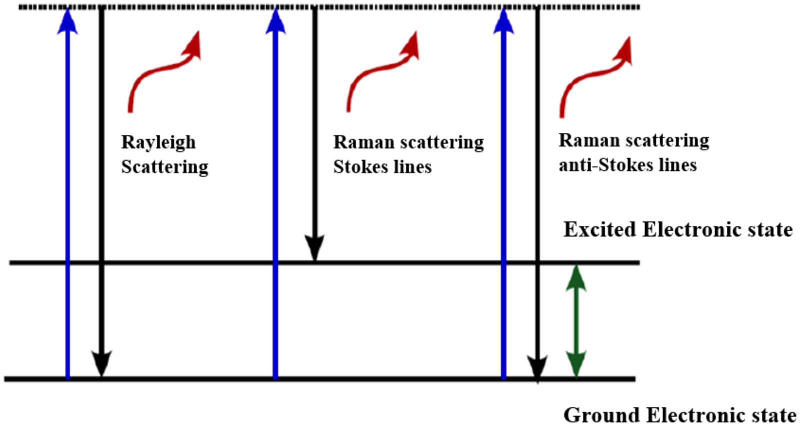

Figure 2.19. Energy level diagram showing three different types of interaction of light on material's surface.

In this research, the composition of the thin films was analyzed via Raman spectroscopy. To measure the Raman Scattering, a laser (632.8 nm He-Ne) that acts as an excitation source was focused on the sample through an optical microscope. The back-scattered light from the sample is collected using the optical microscope and sent into a spectrometer. The CCD camera was coupled with a PC interface that allows storing and controlling Raman data. The laser was spotted in multiple point on the film and the average intensity values were plotted. The measurement was carried out using Dr. Brolo's equipment in the Chemistry Dept. at the University of Victoria. The Raman peaks of ZnO and $TiSi_2$ milled samples were studied and are analyzed based on their spectral positions. Raman peaks at 196 cm^{-1} (B_{3g} symmetry vibration), 210 cm^{-1} (B_{1g} symmetry vibration) and 245 cm^{-1} (A_g symmetry) indicate the C54 phase for $TiSi_2$ nanoparticles [94]. Similarly, Raman spectrum of bulk ZnO presents 6 first-order peaks [176–180]. The two most intense peaks are associated to the E_2 modes at 99 cm^{-1} (named as E_2^{low}), dominated by the vibrations of the heavy Zn sub-lattice, and the second at 437 cm^{-1} (named as E_2^{low}), which involves mostly the oxygen atom [176–178,180]. These are non-polar modes and Raman active only. Others A_1 and E_1 phonons are due to oxygen dominated. They are polar modes and exposure two different frequencies of the transverse optical (TO) and longitudinal optical (LO) phonon modes [180]. The 203 cm^{-1} peak is due to A_1 symmetry and attributed to a transverse acoustic (TA) overtone[176,177]. This mode also can occur due to $2E_2^{low}$ with possible contributions of 2TA [176,177]. Due to the influence of the phonons outside the center of the Brillouin zone, the second-order Raman spectrum become dominant and low-wavenumber region around 333 cm^{-1} is ascribed to difference between $E_2^{high} – E_2^{low}$ [176]. Additional peak that emerges around 410 cm^{-1} in the spectrum (E_1 symmetry), which is due to E_1 (TO) mode [177]. Similarly, peak around 541 cm^{-1} is due to A_1 symmetry and is attributed to $2B_1^{low}$ and LA (longitudinal acoustic) overtones [176,177]. The E_1 (LO) mode around 586 cm^{-1} arise from the background, which originate from second order Raman scattering [176]. The presence of impurities and/or defects can also influence this mode [176].

2.3.4. Photoluminescence Spectroscopy

Photoluminescence (PL) spectroscopy is a form of light emission spectroscopy where light emission comes from a process called photo-excitation. As the light is directed onto a sample, the electrons from the material travel into excited states (excitation). When the electrons move back to their equilibrium states from the excited states, the energy is released in light (relaxation) form. This technique helps in identifying point defects, including extrinsic and intrinsic defects in materials. It is also a useful tool in evaluating the quality and physical parameters in thin films and nanomaterials. In this research, PL properties of different ZnO sensors were investigated.

2.3.5. Energy Dispersive Spectroscopy (EDS):

Energy-dispersive X-ray spectroscopy (EDS) is a non-destructive analytic tool capable of providing chemical information about the elemental composition inside the material that is being mapped. The EDS uses high-energy electromagnetic radiation (X-rays) to eject the ‘core’ electrons from an atom. Removing these electrons from materials leaves a hole that a higher energy electron can fill in, and it will release energy as it relaxes. The energy released during this relaxation process is unique to each element present on the periodic table. Such a bombarding process on a sample using X-rays helps identify the element type and their proportion. In this research, EDS properties of $TiSi_2$ and ZnO thin film were investigated.

Chapter 3

3. Multifunctional thin films

Colloidal suspension used for the results in this chapter were prepared by R. Sapkota and Julia E. Bobak. Jinxiang Zou (MITACS Globalink program) and Sahil Dawka (MEng Graduate student) assisted in preparing nanostructured films. Jinxiang Zou assisted in analyzing contact angle data and electrical measurement of the samples. The author worked on preparing colloidal suspension of silicon, $TiSi_2$ *and ZnO used in this chapter. The author also worked on measuring contact angle and electrical properties of different nanostructured films coated on various rigid and flexible substrates. Parts of the results in this chapter were published in [J2].*

This chapter will be focused on results of multifunctional nanostructured thin films fabrication and characterization. The promising multifunctional characteristics are explained based on wettability and conductivity measured on different prepared thin film via PBM. Furthermore, various factors such as, annealing condition, and the nature of powder/materials coating behavior on different substrates are also studied using wettability and conductivity tests.

3.1. Introduction

In the past few decades, the physical and chemical properties of nanomaterials, which are significantly different from traditional bulk solids, have interested many researchers in developing nanomaterials for various applications [68,69,181]. Consequently, to take the advantage of these desired properties, thin films of nanoparticles have been extensively used to produce nanostructured surfaces for numerous applications, including solar cells [182], photocatalysis [183], self-cleaning surfaces [184], and transparent conductive films [185]. Two main approaches: “top-down” or “bottom-up” nanofabrication methods have been implemented for controlling the morphology of nanoparticles during the fabrication process, which in turn alters the nanostructured film properties [42,186].

PBM is a prominent tool for nanofabrication, which offers a unique top-down approach to nanoparticle thin-film synthesis. This technique can produce immense amounts of nanoscale particles in an appropriate solvent without the use of complex chemical or physical processing. The grinding process commences from crushing bulk powder into a nanoscale colloidal suspension suitable for thin-film coating of various functional materials from solution. Generally, efficient energy impact during milling motion of beads crushes the material into fine particles through collisional and frictional forces that leads in producing nanostructured films [122]. PBM also has numerous advantages in comparison to other ball mill types, including simple setup/cleaning and moderate cost. Several parameters that influence the milling process are speed of revolution, jar rotation speed, milling time, the total weight of milling balls, the ratio of beads and grinding materials volume, and the relative direction of motion of disk revolution and jar rotation [121]. Additionally, solvent used during wet grinding can also change the resultant slurry properties. Consequently, adjusting the PBM grinding parameters, the size and dispersion of the nanomaterials can be controlled. Hence, such optimized method during grinding are used by different industries [59,187–194] for creating morphological nanostructures. Lately, PBM has been utilized for studying magnetic properties of Co/SiO_2 nanoparticles [195], preparing ultra-fine

Si nanoparticles [196], hydrogen storage [197], creating bio-nanocomposites [58], graphene powder [198], molecular crystal powder [199], preparing catalysts and electrodes [200–202], producing interlayer materials for solar cells [203], preparing nanobiochars [204] and nanoparticle ink [56], producing nanoparticles for lubrication [205] and carbon nanotube nanocomposites [206], and investigating nano Ti-polymer [207].

The PBM and its performance of silicon-based materials are particularly relevant to the application and provide a wide area for further exploration. In this work, we study the thin films prepared using nanoparticles of $TiSi_2$ or Si formed via PBM in different solvent and showed the nanoscale grinding approach could be used for creating multifunctional nanostructured film coating on various substrates. This work is mainly focused on varying grinding parameter to examine the effect on structure, surface wettability and electrical properties of the nanostructured film. The main goal of our work is to produce the resultant coating with tunable behavior about both electrical conductance and wettability and thereby yield the film with a wide range of variation in resistivity and contact angle through the grinding condition. These approaches of preparing nanofilms from the colloidal suspension can provide benefits for surface coatings and devices.

3.2. Methods and Materials

Silicon powder (-100+325 mesh, 99.999% purity, Alfa Aesar), $TiSi_2$ powder (-200 mesh, 99.5% purity, Alfa Aesar), isopropanol (IPA; Laboratory grade, Fisher), and ethylene glycol (EG;

99% purity, BDH) were used as received. A 100 nm layer of SiO_2 on silicon wafers (SiO_2/Si), and glass were used as flat substrates for thin film coatings.

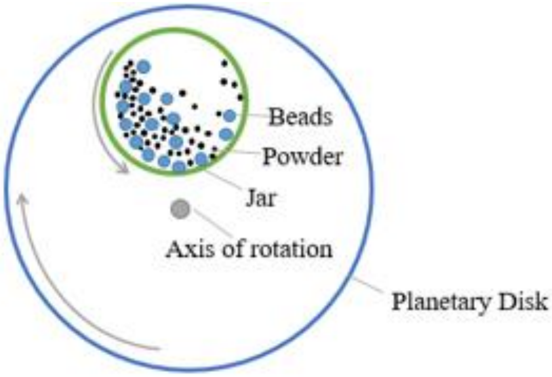

Figure 3.1. Planetary ball mill grinding motion. The planetary disk rotates opposite to the direction of the jar rotation. The disk revolves around the axis of rotation, which defines the speed of revolution.

Wet grinding is performed using a Retsch PM-200 PBM machine (see schematic, ***Figure 3.1)*** (jars made of zirconia, 50 mL capacity) or Fritsch Pulverisette 7 planetary micro mill (see schematic, ***Figure 2. 5 a***) (jars made of silicon nitride, 80 mL capacity). Zirconia beads (2 mm in diameter) are used for grinding. In a typical experiment, $TiSi_2$ powder (20.8 g) is ground in approx. 10 mL EG solvent with approximately 100 g of beads; Si powder (4.48 g) is ground with approx. 10 mL of IPA with approximately 90 g of beads. The grinding speed and time are varied between 200-1000 rpm (revolutions per minute) and 10 - 480 minutes (in cycles of 5 minutes grinding; 10 minutes resting), respectively. After each grinding trial is completed, a syringe and stainless-steel mesh are used to extract and separate the resulting suspension from the grinding beads. Additional solvent (10 mL) is also added to the jar and the extraction process repeated as required to remove all the ground particles. Several films from the ground materials via drop-casting are prepared on substrates for the characterization. The ground materials tend to settle at the bottom of the vial. To ensure uniformity of the resulting films, suspensions are shaken and dispersed using an ultrasonic bath (VWR ultrasonicator cleaner with digital timer) prior to coating substrates. If the suspension is frequently used, then light sonication is enough for the dispersion. However, the material gets stuck solidly at the bottom of the vial if not used for a longer period. In such a case, continuous sonication and manual side-wise shaking at regular intervals will make a homogenous suspension. The volume of solution used for making films varied from a few µL to tens of µL. $TiSi_2$ films are usually dried at 75^0 C in a mechanical oven (Lindberg/Blue MO1440A-1), whereas Si films are dried at room temperature for 15-20 minutes.

For structural characterization, scanning electron microscopy (SEM) is performed with a Hitachi S-4700 and surface imaging employed a Nanonics MultiView 1000 atomic force microscope (AFM) with Olympus BXFM optical microscope. Film composition was analyzed via Raman spectroscopy using a Renishaw inVia system with 632.8 nm laser line and energy dispersive x-ray analysis (EDX) using a Hitachi S-2600N SEM. A custom-made set up is used for contact angle (CA) measurements similar to previous work [133] (see ***Figure 2.14)***. To obtain the CA data, 3 µL of deionized (DI) water is typically dropped on the prepared thin films. The analysis of CA data is performed using ImageJ (version 1.46r and drop snake analysis plugin) [208]. Electrical studies are performed using a Janis probe station in conjunction with a Keithley 4200 semiconductor characterization system. For electrical measurements, two-terminal contacts are made on the films using silver paint and subsequently dried in the oven at 75^0 C for approximately 45 minutes.

3.3. Results

Examples of thin film coatings formed using ground titanium disilicide and silicon are shown in ***Figure 3.2***. Optical microscopy of film cross-sections showed measured thickness varied from approximately 10 µm to 30 µm. Flat, non-planar and flexible thin coatings could all be formed from solution using the nanoparticle dispersions resulting from nanoscale grinding and displayed good stability and adhesion under ambient conditions and up to several hundred degrees Celsius.

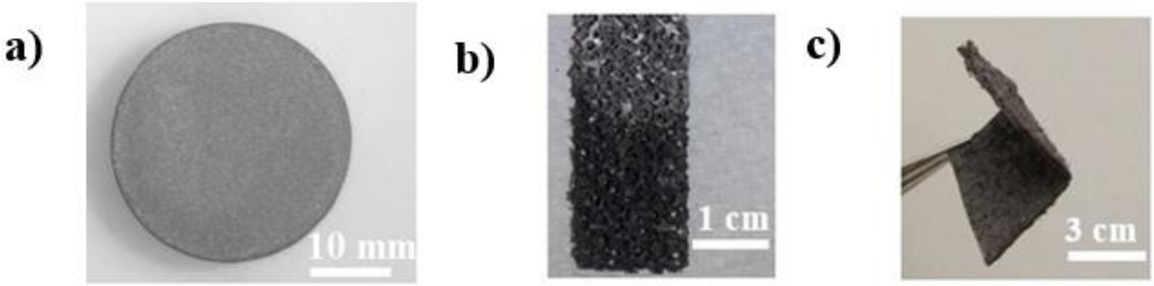

Figure 3.2. Optical images of thin film coatings. (a) $TiSi_2$ ground in EG at 400 rpm for 30 minutes coating a flat glass substrate. (b) Porous aluminum dip coated with $TiSi_2$ nanoparticles. (c) Silicon ground with IPA at 500 rpm for 100 minutes coating a flexible (fabric) substrate.

SEM images in ***Figure 3.3 a and b*** show particles before and after grinding, highlighting the effectiveness of PBM at reducing sizes to nanoscale dimensions from the starting micron-scale powder within minutes. For Silicon materials ground at higher grinding conditions (400 rpm for 100 min) in IPA solvent, shows some particle sizes as small as 50 nm. However, a range of particles between 300 nm to 100 nm were primarily present. The nanoparticle coatings were also characterized by AFM (***Figure 3.3 c and d).*** As the particles are ground into finer sizes over longer periods of time, we observe a reduction in root mean square (RMS) roughness as measured with AFM to well-below 100 nm (***Figure 3.3 e***)

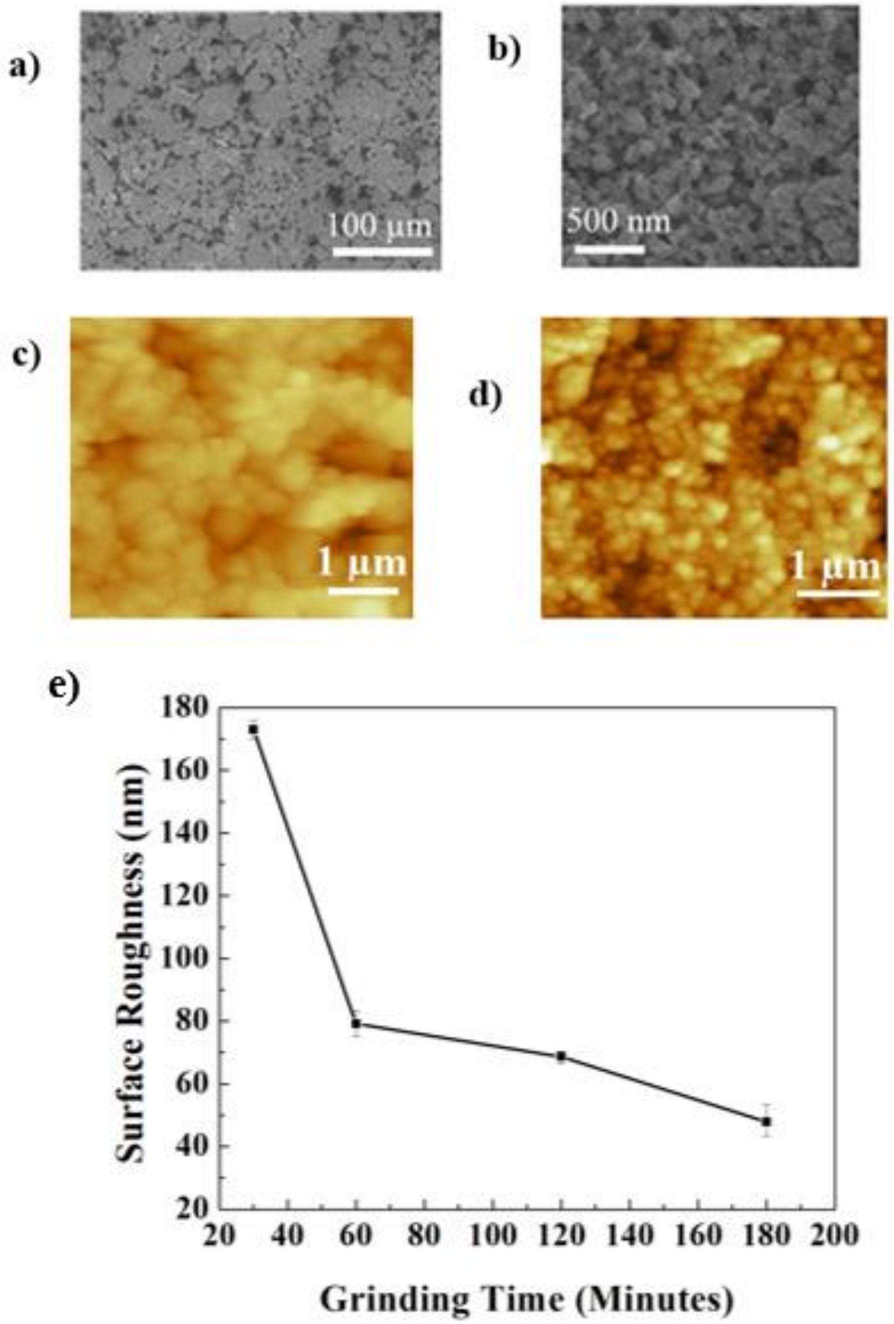

Figure 3.3. a) SEM image of unground Si powder (particle sizes between approximately 10 µm to 50 µm). (b) SEM image of ground Si in IPA at 400 rpm for 100 min (particle sizes approximately 50 nm).

AFM images of $TiSi_2$ ground in EG at 400 rpm for (c) 30 min and (d) 180 min. (e) Plot of RMS surface roughness of $TiSi_2$ film ground in EG at 400 rpm versus grinding time.

Raman spectra generally showed the crystallinity of ground material remains intact after milling (***Figure 3.4*** **a**). However, EDX data (***Figure 3.4 b and c***) showed that carbon and oxygen peaks appeared in films formed via the grinding process, which is likely due to surface modification of the nanoparticle surfaces (see discussion section below).

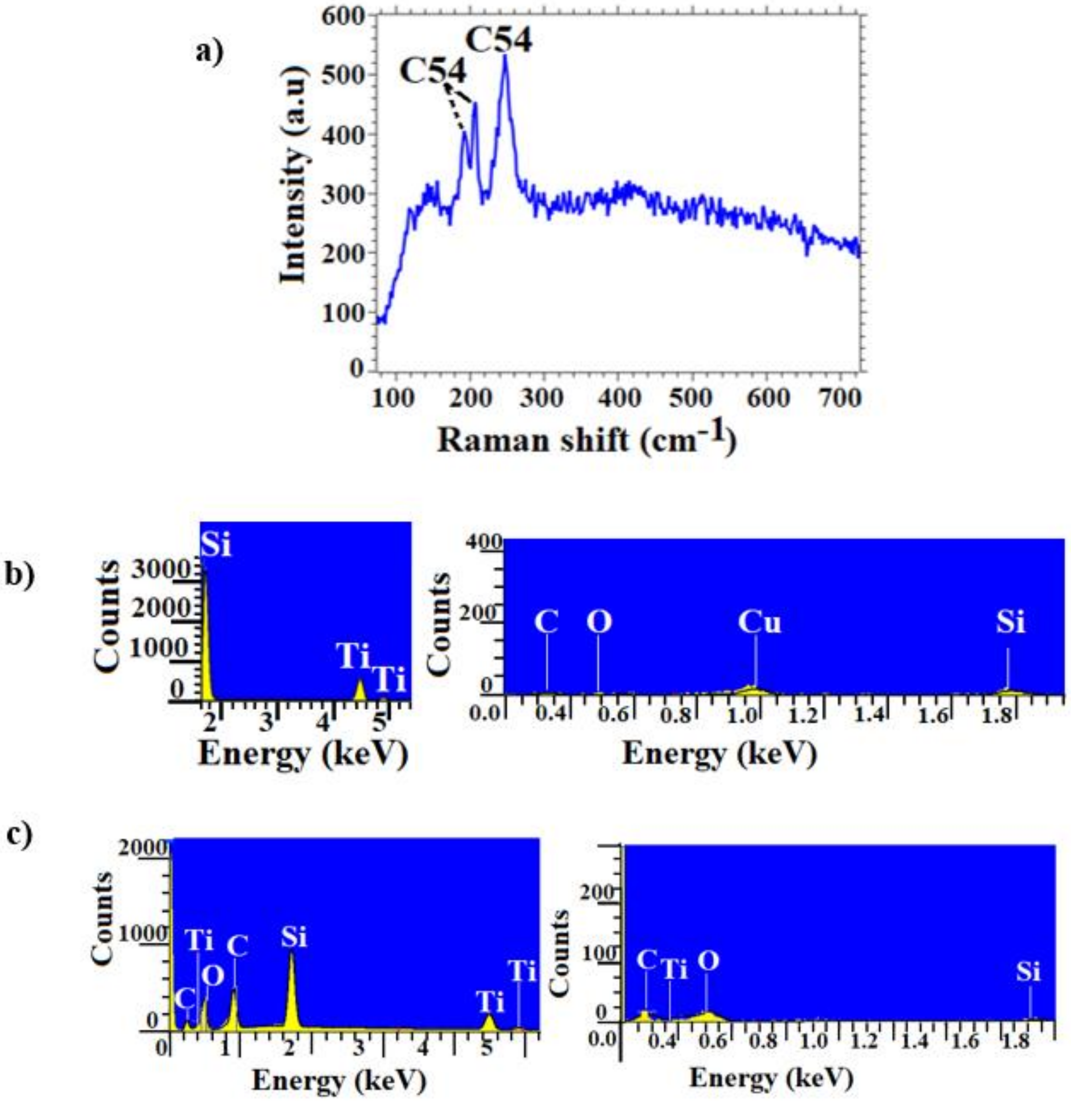

Figure 3.4. (a) Raman Spectra showing orthorhombic face-centered C54 phase [91] peaks of TiSi$_2$ ground in EG at 400 rpm for 60 min. (b) EDX of bulk unground TiSi$_2$ powder taken with 10 kV (left) and 3 kV beam voltage (right). (c) EDX of TiSi$_2$ ground in IPA at 400 rpm for 10 min taken with 10 kV (left) and 3 kV beam voltage (right). (Cu peaks are from sample holder)

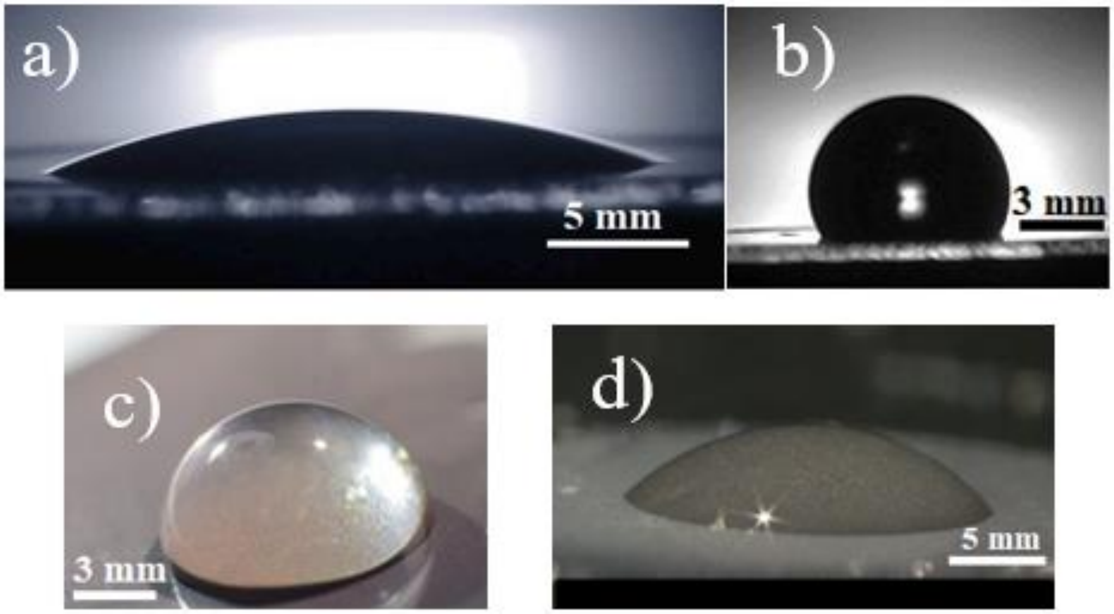

Figure 3.5. Images of water drops on Si films ground in IPA at 500 rpm for (a) 60 min (CA = 17.7 ± 3^0) and (b) 8 hours (CA = 117.7 ± 2^0). (c) Image of water drop on Si film ground in IPA at 400 rpm for 15 hours (CA = 115.1 ± 2^0). (d) Image of water drop on $TiSi_2$ film ground in EG at 400 rpm for 30 minutes (CA = 38.6 ± 4^0).

Figure 3.5 shows photographs that illustrate the effect of different grinding conditions on the thin film contact angles we observed. In this case of Si, the contact angle increases with grinding time resulting in a change from a hydrophilic to a hydrophobic film surface. In ***Figure 3.6*** we plot contact angle vs. grinding time for Si films. In general, it is observed that films of silicon nanoparticles become increasingly hydrophobic (larger CA) as grinding time is increased to obtain smaller particle sizes. Films of titanium disilicide on the other hand, show a trend of increasing hydrophilicity or decreasing CA with grinding time (***Figure 3.7 a***), as well as grinding speed (***Figure 3.7 b***). This behavior is likely due to a combination of geometric/size effects and surface modifications caused by the PBM process (see Discussion section). Overall, the CA data illustrate the ability of nanogrinding to tune the wettability of surfaces over a broad range from hydrophilic to hydrophobic.

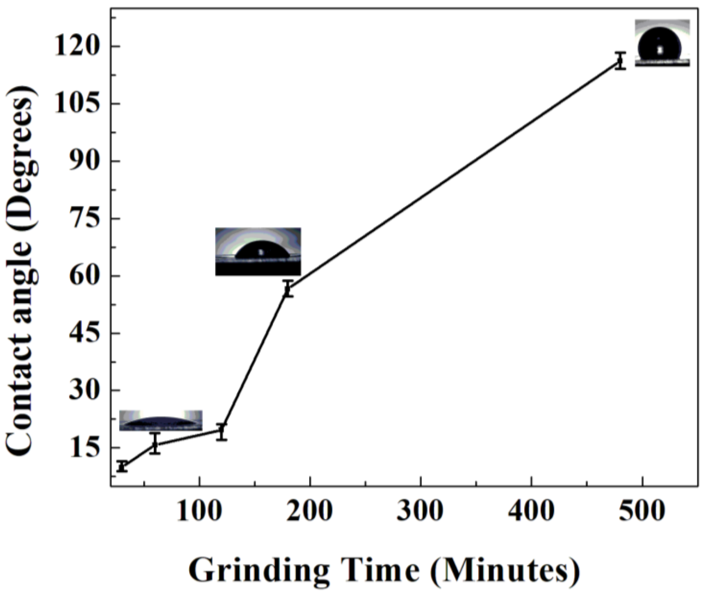

Figure 3.6. Variation in contact angle of Si films with grinding time (constant grinding speed of 500 rpm in IPA).

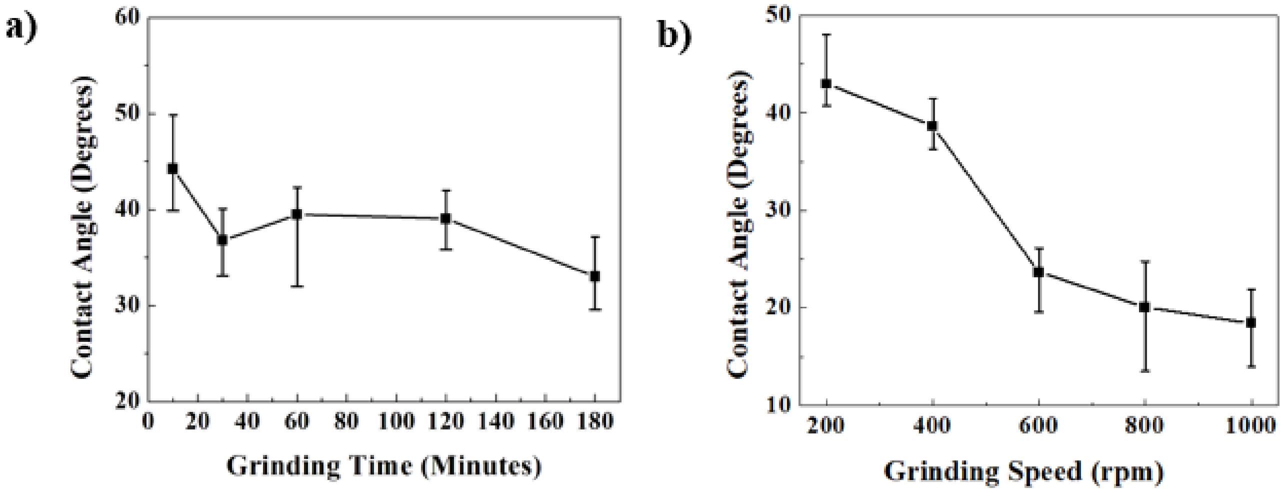

Figure 3.7. Variation in contact angle of $TiSi_2$ films with grinding time (constant grinding speed of 400 rpm in EG). (b) Variation of contact angle for $TiSi_2$ films with grinding speed (constant grinding time of 10 minutes in EG).

Contact Angle variation with respect to solvent

The variation in contact angle is observed on different nanostructured film prepared at varied grinding condition (speed/time/solvent). Nanostructured film created from colloidal suspension of nanoparticles (silicon, titanium disilicide and zinc oxide) shows alternation of contact angle with respect to grinding parameters. Along with the various geometric sizes of nanoparticles formed during grinding, the effect of solvent on nanoparticles surfaces is also clearly noticeable (***Figure 3. 8***) as experimented from contact angle analysis.

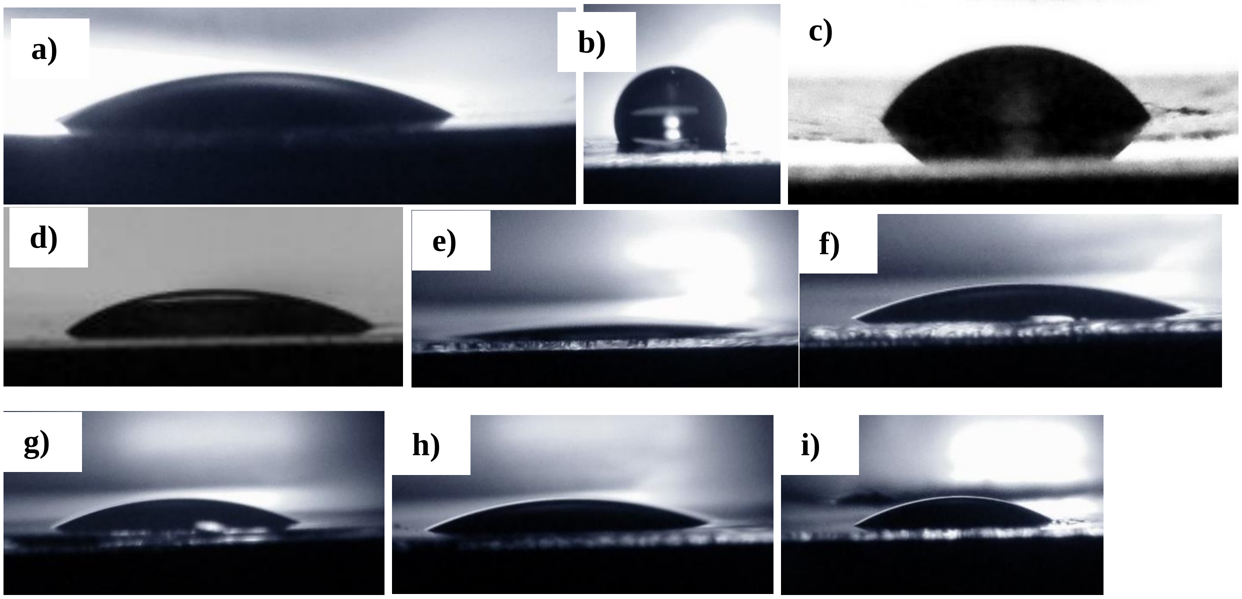

Figure 3. 8. DI water drops on $TiSi_2$ films ground in IPA at 400 rpm for (a) 100 min (CA = 23.9 ± 0.7^0) and (b) 300 minutes (CA = 105.1 ± 3^0). (c) DI water drops on Si film ground in EG for 60 minutes (c) 300 rpm (CA = 43.70 ± 1^0). (d) 500 rpm (CA = 24.3 ± 1^0). DI water drops on ZnO film ground in EG for 10 minutes (e) 200 rpm (CA = 7.71 ± 1^0). (f) 600 rpm (CA = 18.23 ± 1^0). DI water drops on ZnO film ground in DI solvent at 200 rpm for (g) 10 minutes (CA = 21.2 ± 1^0). (h) 30 minutes (CA = 19.97 ± 1^0) (i) ZnO ground in IPA solvent for 10 minutes (CA = 25.4 ± 2^0). All films were prepared on glass substrates.

We also examined the electrical properties of the thin films: $TiSi_2$, in particular, is known to be metallic in the bulk crystalline phase. Two-terminal current-voltage (*I-V*) characteristics of the thin films showed linear behavior (e.g., ***Figure 3.9 a***), indicating low-resistance ohmic contacts were made to the $TiSi_2$ films cast from solution. Thin film resistivity versus grinding time is plotted in ***Figure 3.9 b***, which initially shows a decrease in resistivity followed by an increase as the grinding time approaches 1 hour. The decreased current flow for longer grinding times may be caused by chemical groups created on the surfaces of the particles from the grinding process (***Figure 3.4)*** and/or an increased inter-particle contact resistance as surface area vs. volume increases for smaller particles in the thin films (see discussion below). However, once again, the tunability of film properties formed via nanogrinding is evident and, when combined with the results of ***Figure 3.6 - 3.9***, their multi-functional nature as well.

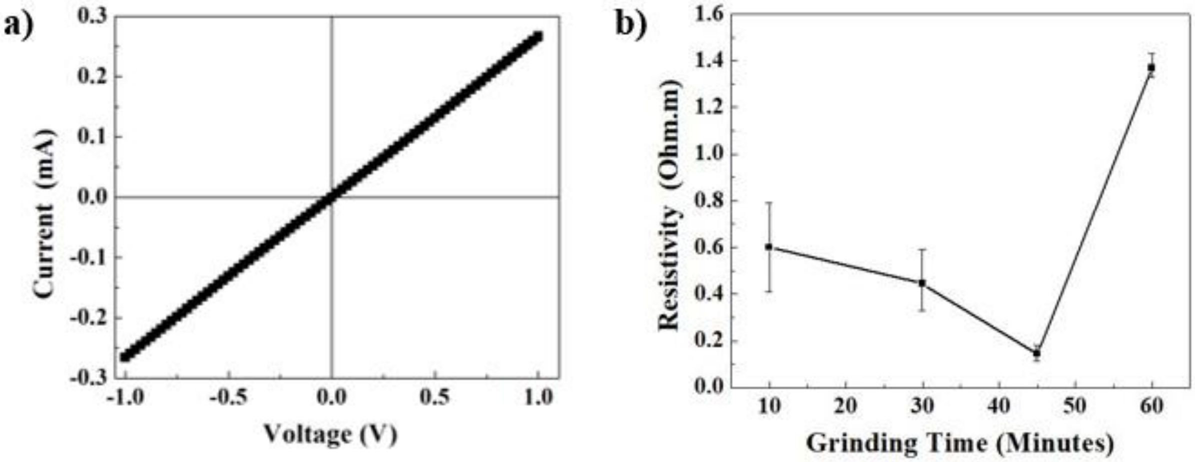

Figure 3.9. (a) Typical I-V plot for $TiSi_2$ thin film formed on SiO_2/Si substrate (ground in EG at 500 rpm for 10 min.). (b) Resistivity versus grinding time for $TiSi_2$ films ground in EG at 400 rpm.

Similarly, electrical measurement of ZnO shows linear behavior when measured at ambient conditions as shown in ***Figure 3. 10***. The drop casted film of ZnO is prepared using 2 µL suspension. We observed the effect of solvent on the nanoparticles surface, which have altered the electrical behavior on the nanostructured films. The sample were tested under room light.

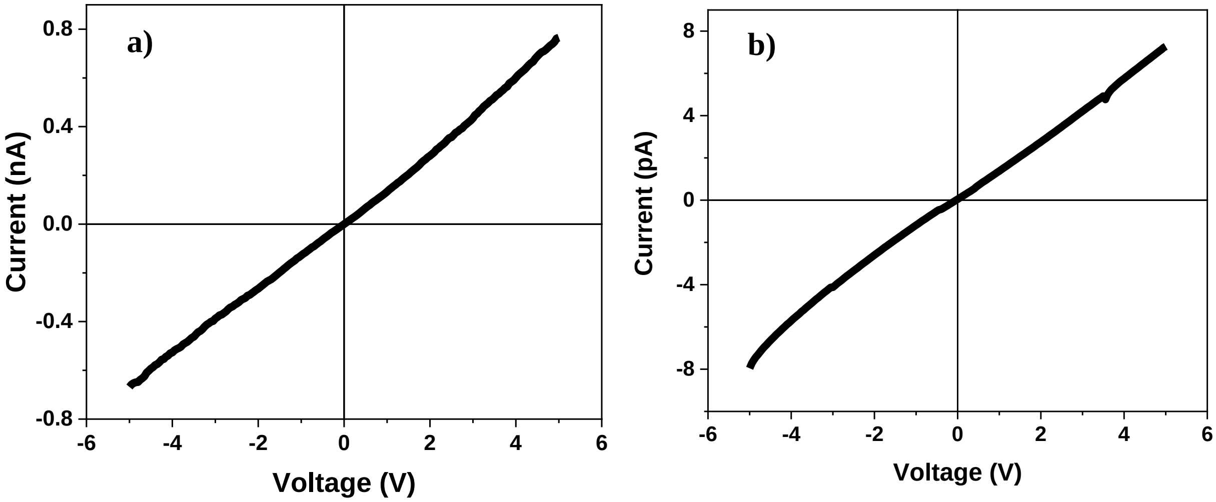

Figure 3. 10. Typical *I-V* plot for ZnO thin film formed on glass substrate ground for 10 minutes (a) in EG solvent at 200 rpm (b) in IPA solvent at 200 rpm.

3.4. Discussion

Since ball milling is a potentially reactive high-energy mechanochemical technique, grinding in the presence of organic solvent as in the present study may result in surface modification of Si and $TiSi_2$ by alkyl, alkene, hydroxyl or related functional groups [209]. Thus, surface properties may depend upon the molecular groups that get attached to the surface during milling (as evidenced by the EDX data). However, the chemical reaction process can be quite complex and it is difficult to predict the precise reaction route and final products from the starting materials – The energy from high-speed impact of beads during milling likely creates dangling bonds on the bulk powder feed and generates reactive silicon radicals, which can lead to the chemical bonds of organic compounds dissociating to form groups which continue to react with surface atoms of Si or $TiSi_2$ forming new chemical bonds like Si-C bond, similar to previous work [210] but in our case with shorter ligands due to the solvents used for grinding.

For silicon, an increasing surface area due to the reduction of particle sizes would lead to an increase in the concentration of functional groups (such as alkyls, alkenes or alkynes) over time during grinding, which likely contributes to the increase in hydrophobicity observed in ***Figure 3.6***. In contrast, for titanium disilicide, the EG solvent used for grinding is more stable and, in addition, attachment of functional groups may be partially inhibited due to titanium, which does not easily form covalent bonds with organic groups [211]. In this case, the modification of the surface of $TiSi_2$ may not have as much influence on the wettability properties of the resultant thin films [212,213]. Another factor in the changing contact angle versus grinding conditions is due to the surface roughness of the nanostructured films. For example, the contact angle of DI water on silicon films ground at 400 rpm for 480 minutes was approximately 115°. The increase in contact angle may be caused by the droplets staying in the Cassie-Baxter state [214], whereas for lower grinding times the liquid can enter gaps in the silicon film and thus obeys the rule of surface topography present in the Wenzel state [134].

IPA solvents can be responsible for creating various functional group on the surfaces of the nanostructured films. Different functional groups can be formed at various treatment times [215], such as hydrocarbon (C-C/C-H), single carbon-oxygen bond i.e hydroxyl or ether (C-OH/C-OR), two carbon-oxygen bonds e.g., carbonyl (C=O) or diether (O-C-O) and π- π^* shake-up satellites [215]. Increase in oxygen concentration on the surface of nanostructures results in increasing the hydrophilicity of the surface whereas hydrocarbons appear to result in hydrophobic behaviour [215]. Therefore, it is assumed that the increased grinding with IPA solvent resulting in hydrophobic surfaces might have occurred due to additional hydrocarbon functional groups being formed.

The electrical resistivity of a nanoparticle thin film depends on packing, grain size, type of solid, etc., all of which affect the transport of charge carriers. The effect of solvent type used for grinding in our studies was also important, with IPA leading to films that were generally poor electrical conductors compared to films produced with particles ground in EG. The efficient creation of nearly insulating alkyl functional groups on the particle surfaces during grinding in IPA is likely the source of this behavior. The resistivity of the $TiSi_2$ film formed via the PBM process could be varied over a large range depending on grinding conditions: In general, when grinding times were either very short (few minutes) or very long (hundreds of minutes) the electrical resistivity increased such that the films became almost insulating. Similar behavior was observed when adjusting grinding speed from 200 rpm to 1000 rpm. The increase in resistivity at the two extremes of grinding likely arises from two very different effects: For small amounts of grinding (time and/or speed) the resultant films appear discontinuous under AFM with what are likely many high resistance gaps and poor contacts due to irregular particles and spacing; For large amounts of grinding, interparticle contacts become more numerous as the surface-to-volume ratio increases, which, along with the introduction of additional chemical moieties on the particle surfaces, likely leads to an overall increase in film resistivity. In the intermediate region (see ***Figure 3.9 b***), the electrical resistivity displays a gradual decrease as grinding speed or time becomes larger, approaching what is likely the optimal grinding condition for electrical conductance based on the parameters of the present study, thus allowing electrical resistivity through the titanium disilicide nanostructured films to be varied in a controllable manner by over one order of magnitude.

3.4.1. Investigation of the annealed films

Generally, the contact angle between 90 to 150^0 are hydrophobic surfaces, 65 to 90^0 are hydrophilic, 20-65^0 are weakly hydrophilic and below 20^0 are superhydrophilic surfaces. The tuning of hydrophobicity to hydrophilicity are usually possible by heat treatment or irradiation of UV light [216]. This possibility of tuning wettability is caused by either change in surface chemistry or surface roughness or the combination of both [216]. The effect of thermal annealing on the nanostructured films at higher temperatures perhaps remove the functional surface groups completely and may alter film wettability.

In order to further examine the effect of functional groups on the nanostructured surfaces, we subjected the experiment of the thin film coatings to elevated temperatures in a quartz tube furnace under an argon environment. The annealing condition was performed by varying temperatures (200 ^{0}C, 400 ^{0}C, 600 ^{0}C and 800 ^{0}C) at different time intervals (30, 60, 180 and 360 minutes) on a variety of substrates (SiO_2/Si, silicon and glass). We studied the wettability and electrical properties of the $TiSi_2$, and Si thin film based on the effect of thermal annealing. ***Figure 3.11*** shows the variation in contact angle for $TiSi_2$ films (coated on glass substrate) as the duration of thermal treatment is increased, indicating a gradual reduction in contact angle. Likewise, ***Figure 3. 12*** shows the variation of contact angle for silicon films on a glass substrate with the increase in the annealing temperature. The results indicate a gradual reduction in contact angle, changing from a hydrophobic to a super-hydrophilic film surface. We have extended our studies further to find the effect of thermal annealing on the different thin films prepared from various solvents. Here, we investigate the multifunctional properties of the nanostructured thin film with respect to different annealing conditions.

Figure 3.11. (a) Sequence of water drop images on $TiSi_2$ films (coated on glass substrates) vs. heating time at 400^0 C under argon atmosphere (grinding in EG at 400 rpm for 180 minutes). From left to right: No heating (CA = 37.7 ± 1^0); 30 min (CA = 23.8 ± 1.5^0); 60 min (CA = 17.3 ± 1^0) and 180 min (CA = 10.5 ± 1^0).

Figure 3. 12. Sequence of water drop images on Si films vs. heating temperature for 30 minutes under argon atmosphere (grinding in IPA at 500 rpm for 100 minutes). From left to right: No heating (CA = 128.09 ± 0.5^0); 200 ^{0}C (CA = 99.19 ± 1.5^0); 400 ^{0}C (CA = 69.27 ± 0.7^0) and 600 ^{0}C (CA = 9.75 ± 1.5^0). The films are coated on glass substrates.

As we know, modifying the roughness and chemical composition of the surface can alter hydrophilicity and hydrophobicity. Particularly, most nano-microtextured were used for producing hydrophobicity/hydrophilicity on various substrates. Some physical treatments like plasma surface modification and chemical corrosion alter the surface roughness, which shows wettability behavior changes [217]. Corresponding to our previous result (shown in ***Figure 3.7***) for non-annealed samples, we observed that increasing grinding time/speed results in reduced contact angle. A similar trend was seen on Si and $TiSi_2$ film annealed at different temperatures/times, despite the type of substrate used. However, the CA were lower than that of non-annealed films. Our solution-casted films were fairly thick (> 20 µm), and we assume the change of contact angle was due to grain size distribution near the film surface, which causes changes in surface roughness. In such films, it is suspected that the surface morphology is very sensitive with increment in annealing temperature, which ultimately changes the grains distributions on the surface of thin films [218]. Therefore, the increasing temperature might have caused aggregated nanostructures on the film surface, reducing the CA. However, AFM and SEM analysis should be investigated to validate the annealed film's surface roughness and morphology (shape, size and particle distribution – see future work, chapter 5).

The contact angle at different annealing conditions is illustrated in ***Figure 3. 13***. In ***Figure 3. 13 (a) and (b),*** it is observed that different $TiSi_2$ film (prepared at various grinding times at a constant speed of 400 rpm using EG solvents) coated on SiO_2/Si substrate shows a decrease in CA with an increase annealing temperature/time. A similar trend of reduced CA is observed on other $TiSi_2$ films (prepared at various grinding conditions (speed/time)) coated on Si substrates (shown in ***Figure 3. 13 (c) and (d)***). Also, $TiSi_2$ films prepared from varied grinding conditions (shown in ***Figure 3. 13 (e) and (f)***) are also coated on a glass substrate. We observe decreasing CA when annealed at a temperature more than 400 ^{0}C for up to 180 minutes. However, CA tends to increase when film coated on glass is annealed at 400 ^{0}C for longer time (> 180 minutes). It is suspected that the contact angle alternation at longer annealing time and/or higher annealing temperature might occur due to a change in surface roughness and/or morphology of grain size.

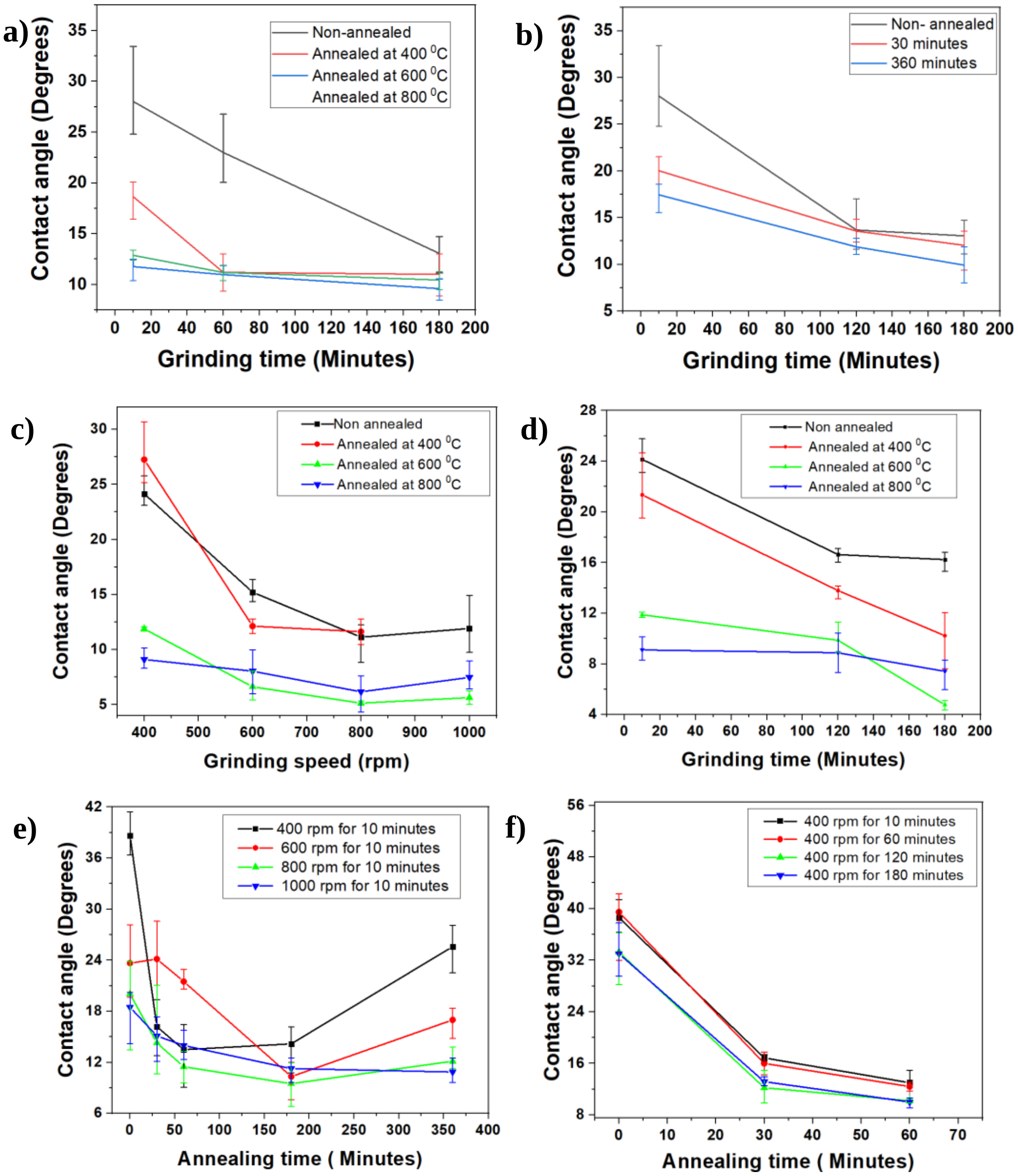

Figure 3. 13. Change in contact angle of different $TiSi_2$ film (coated on SiO_2/Si substrate) prepared from varied grinding time at constant speed of 400 rpm. The film is annealed (a) for 60 minutes at different temperature (b) at 400 ^{0}C for different time. Change in contact angle of different $TiSi_2$ film (coated on Si substrate); (c) prepared at varied grinding speed at constant time of 10 minutes, where films are annealed for 30 minutes at different temperature, (d) film prepared at varied grinding time at constant speed of 400 rpm, where films are annealed for 60 minutes at different temperature. $TiSi_2$ film coated on glass substrates are annealed for different time (e) annealed at 400 ^{0}C (f) annealed at 600 ^{0}C.

On the one hand, most of the $TiSi_2$ films coated on various substrates prepared at lower grinding speed/time show the tuning of weakly hydrophilic to superhydrophilic behavior with increasing annealing time/temperature. On the other hand, the film prepared at higher grinding conditions (speed/time) shows slightly lower CA at varied annealing conditions. Indeed, it is observed that several $TiSi_2$ films prepared at different grinding conditions tested at higher annealing temperature/time show superhydrophilic behavior. This may imply that the polarity of surface ligands increases with heat treatment due to breaking of hydroxyl bonds, resulting in behavior like what occurs as grinding time/speed are increased (***Figure 3.7***). Additionally, the surface morphology, composition and crystallinity are the main parameters that influence surface wettability. The effects of annealing can alter the grain size morphology, chemical functionalization group, or the air/water interface of solid and air composite rough structures [210]. So, if the degree of surface roughness changes (increase/decrease), the hydrophilicity of a hydrophilic film gets enhanced, as suggested by Wenzel theory [134].

For silicon film prepared at varied grinding conditions shows a gradual reduction in contact angle with increased annealing time/temperature on all three substrates, as shown in ***Figure 3. 14***. The increased annealing time/temperature for silicon films (prepared at the lower grinding time (<180 minutes)) coated on three substrates shows a slight reduction in contact angle. In contrast, a higher grinding time (480 minutes) trials revealed significantly reduced contact angles on SiO_2/Si and Si substrates. In ***Figure 3. 14 (d) and (e),*** we compare the contact angle vs annealing temperature and contact angle vs annealing time of the specific type of Si film (ground at 500 rpm for 8 hours), coated on three different rigid substrates. For this type of trial, we observed that silicon nanoparticles film on Si and SiO_2 substrates become increasingly hydrophilic (smaller CA) as annealing time (> 1 hour)/temperature (> 400 ^{0}C) is increased. However, gradual reduction on contact angle is observed on glass substrate at lower annealing time (< 3 hours)/temperature (< 400 ^{0}C), whereas at higher annealing temperature/time, CA shows a sharp decline.

Effects of annealing on silicon crystallinity, surface roughness and surface chemistry are responsible for altering silicon film contact angle. It is possible that lower contact angles on most of the annealed film are due to a reduction in air pockets. Generally, the thin film's grain boundary gets improved after thermal treatment, and hence more grains get close to each other by reducing air pockets. Consequently, the film tends to increase hydrophilicity at increased annealing temperature/time. A smaller reduction of contact angle on Si films after thermal treatment is also consistent with the assumption of alkyl or related groups being removed from their surface.

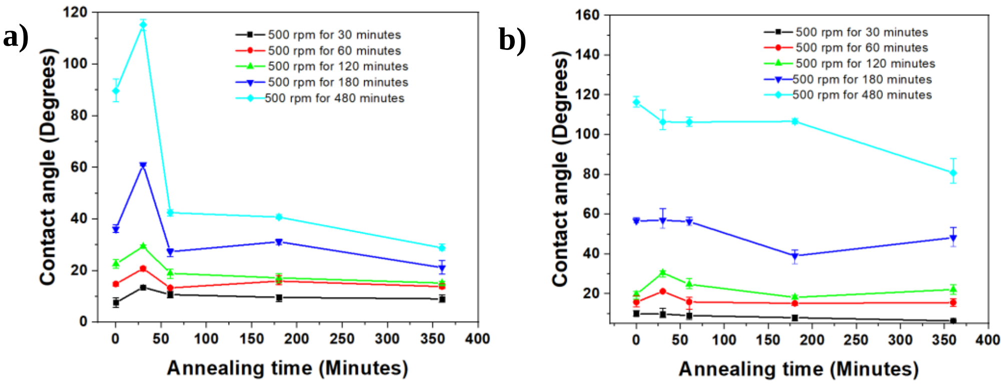

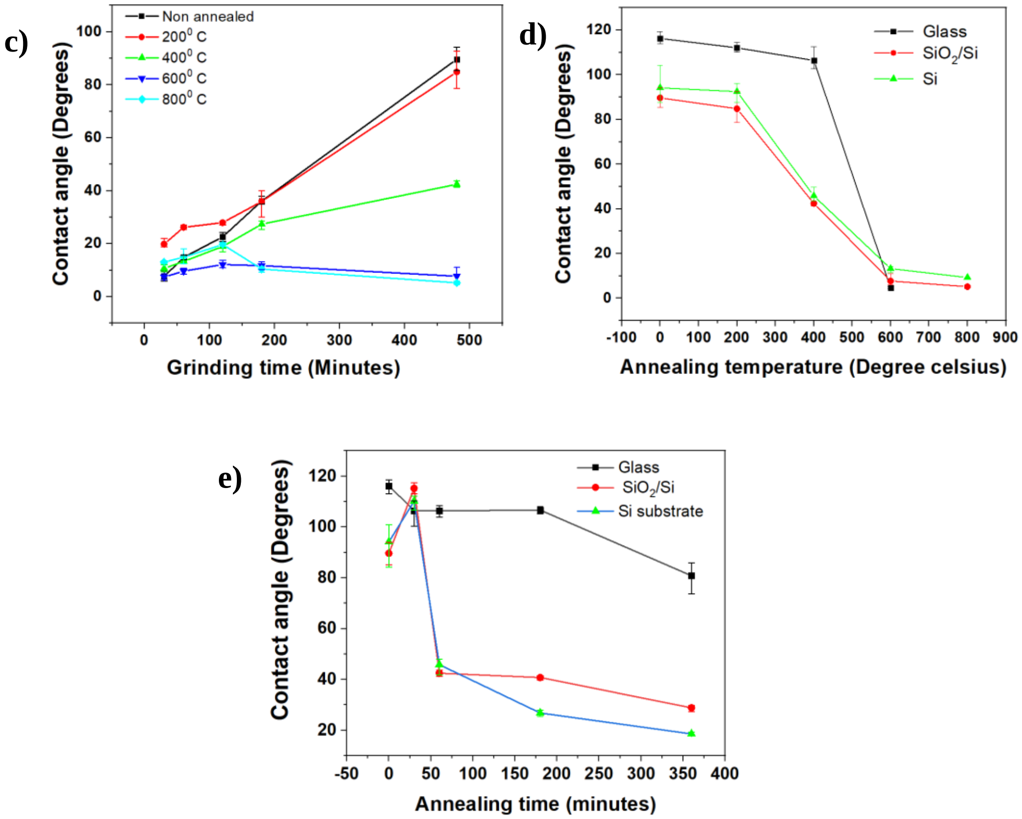

Figure 3. 14. Different silicon film annealed at 400 ^{0}C at different annealing time (a) SiO_2/Si (b) glass substrate, (c) silicon film coated on Si substrate and annealed at different temperature for 60 minutes. Change in contact angles of Si film (Ground for 8 hours at 500 rpm in IPA solvent) (d) Annealed for 60 minutes at different temperatures on various substrates (e) Annealed at constant temperature (400 ^{0}C) for different time on various rigid substrates.

Results from ***Figure 3. 13*** and ***Figure 3. 14*** indicate that contact angle is directly affected by solvent type, ground material type and/or surface roughness of the resultant film. A similar study of Raman and EDX analysis (as shown in ***Figure 3.4***) is required to provide evidence to show the presence/absence of functional surface groups on annealed films. Such study showing the surface functional group of nanostructured film at different annealing temperatures/times can provide deeper information about the cause of reduced CA. On the other hand, investigation of surface roughness and morphology on annealed film could also support relation between CA, annealed thin film texture and grain size.

We also have investigated the effect of annealing conditions on the electrical behavior of $TiSi_2$ and Si film coated on SiO_2/Si substrate. It is well known that a number of carrier concentration is a primary concern for altering the resistivity on any type of film. From our result, we observe that increase in annealing time (up to 360 minutes) shows an increase in resistivity for a film prepared at varied grinding conditions. ***Figure 3. 15 (a)*** and ***(b)*** show different $TiSi_2$ films prepared at various grinding condition that are thermally treated under argon atmosphere at different annealing conditions. Films prepared at a various grinding time (at a constant speed of 400 rpm) and annealed at 400 ^{0}C for 60 minutes, we observe an increase in resistivity for higher grinding time (up to 180 minutes) trials. Similarly, for the film prepared at varied grinding speed (at a constant grinding time for 10 minutes) and annealed at 400 ^{0}C for 360 minutes, we again observe an increase in resistivity for higher grinding speed (up to 800 rpm) trials. We assume some possibilities for an increase in resistivity of $TiSi_2$ ground samples are due to grain boundaries and an increase in defects after milling [92]. There will be more dangling bonds and defects in the powder due to the impact energies from the milling technique. Compared with the non-annealed films (as shown in ***Figure 3.9***), we observe low resistivity for an annealed ground film, as shown in ***Figure 3. 15*** **(a)**. After annealing, chemical composition on the film surface might get changed, and grain boundaries could be reduced, which then improves the inter-particle distance; also, defects will be possibly minimized [92,93]. All these factors help in enhancing carrier concentration flow. For longer grinding speed trials (> 600 rpm), we assume that a large number of defects and/or dangling bonds cause the passivation on top of the $TiSi_2$ layer and thereby shows higher resistance [219]. However, tunability of resistivity at different grinding conditions, such as constant grinding speed (approx. one order of magnitude) and constant grinding time (approx. 4 order of magnitude), was possible after annealing.

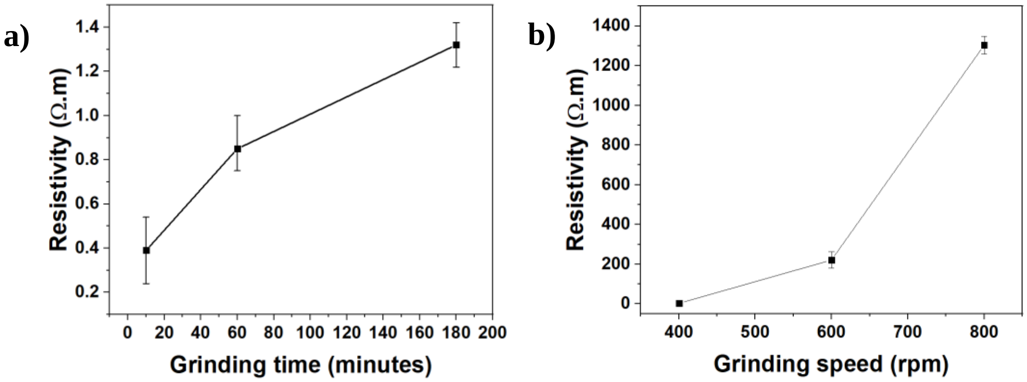

Figure 3. 15. Change in resistivity on $TiSi_2$ film annealed at 400 ^{0}C (a) The films are prepared at constant speed of 400 rpm for different grinding time and later annealed for 60 minutes (b) The film prepared at constant grinding time for 10 minutes with varied grinding speed and later annealed for 360 minutes.

Similarly, we also investigate the annealing effect on a specific type of silicon ground at 500 rpm for 3 hours in IPA solvent. From the result shown in ***Figure 3. 16***, we observed that increase in annealing condition (temperature/time), the current get increases. The milling could introduce defects and vacancies on silicon powder [220]. After annealing, a defect might improve, a grain boundary could be minimized, and chemical groups on ground particles may get removed from the film surface. Likewise, particle crystallinity may perhaps get enhanced at higher annealing conditions. All these factors help in improving current. Thus, annealing effects show tunable electrical properties on silicon ground thin films.

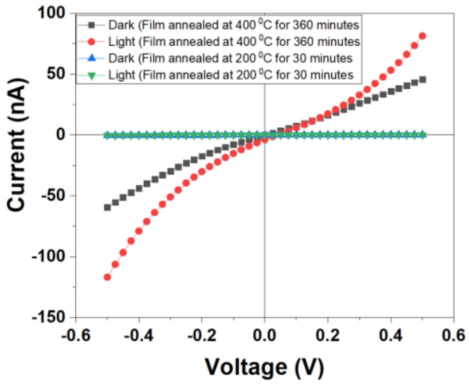

Figure 3. 16. Silicon film annealed at different annealing condition. The film is prepared by grinding at 500 rpm for 3 hours in IPA solvent and later coated on SiO_2/Si substrates.

3.4.2. Wettability and Conductivity on flexible substrates

We have also compared the wettability and conductivity properties of both ground silicon and $TiSi_2$ thin films on various flexible substrates, such as paper towel (~ 7 3/5 x 15”), zap paper (~ 0.15 mm thickness), fiber paper (~ 0.35 mm thickness) and anodic aluminum oxide (AAO) substrates (Whatman Anodisc25 membrane with supportive ring). In our experiment, we ground high purity silicon powder at 500 rpm using IPA solvent at a different grinding time on Pulverisette Fritsch 7 grinding machine and resultant colloidal suspension were coated on different flexible substrates. The prepared films were dried at room temperature, and a wettability experiment was performed. As shown in ***Figure 3. 17***. we observe that increase in grinding time shows higher contact angles for silicon films coated on AAO, paper towel and fiber paper. However, the contact angle decreases for Zap paper substrates coated with higher grinding time (150 minutes) trial. We believe that a decrease in the contact angle might have occurred by the texture formed from smaller particle size on zap paper surface, which favors the water to lower its contact angle against the substrate surface. At last, we found that tuning of contact angle with respect to the grinding condition was also possible in most of the flexible substrates.

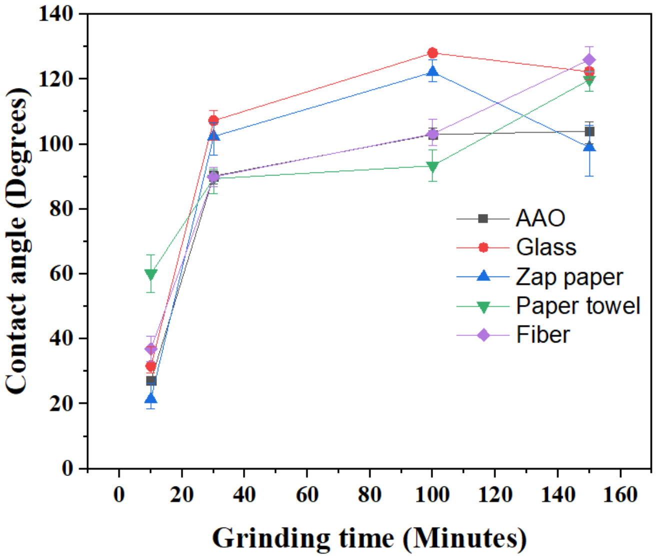

Figure 3. 17. Change in contact angles of silicon film ground at different grinding time with a constant grinding speed of 500 rpm using IPA solvent.

In the case of $TiSi_2$ trials (shown in ***Figure 3. 18***), we show dissimilar observations compared with silicon trials. For most of the $TiSi_2$ suspension coated on a paper towel, the contact angle was not measured because of quick absorption of water drop on the substrate, as the film starts behaving superhydrophilic. Similarly, for fiber paper substrate, a similar case (quick absorption phenomena) was seen for higher grinding speed trials (> 600 rpm). However, on the collected data it is seen that, contact angle decreases with increasing grinding speed/time on all substrates. As we know, the texture formation from grain particles and the air pockets formation might get differ among substrates and hence, causes different contact angles between substrates.

Most importantly, from the previous experiment (film coated on rigid substrates), it is observed that the higher grinding condition trials show a lower contact angle, and it is valid for those samples being superhydrophilic on paper towels and fiber substrates. The observation of lower contact on flexible substrates is possibly due to substrate porosity, which is observed from the spreading of colloidal suspension on the substrate surfaces. Hence, substrates with high porosity tend to show lower contact angles and vice versa.

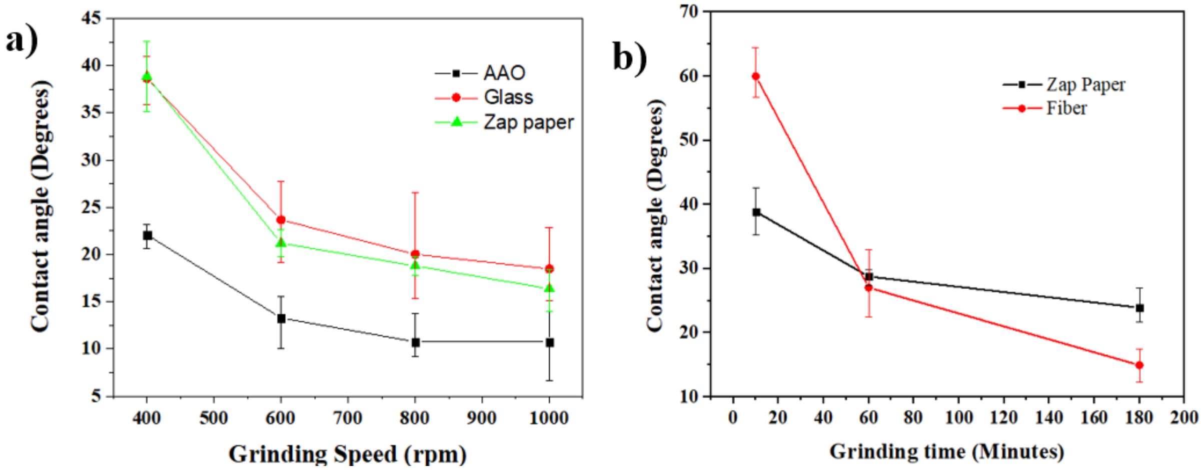

Figure 3. 18. Variation of contact angle on flexible substrates (a) $TiSi_2$ films with grinding speed (constant grinding time of 10 minutes in EG). (b) $TiSi_2$ films with grinding time (constant grinding speed of 400 rpm in EG).

Concurrently, we also did some electrical measurements of $TiSi_2$ trials on those flexible substrates. We observed that the thin films' two-terminal current-voltage (*I*-*V*) characteristics showed linear behavior (***Figure 3. 19***) on zap and paper towel substrates. However, we examined the slight non-linear behavior on AAO substrate (shown in ***Figure 3. 20 a***), which might have occurred due to an unstable contact region during measurement. We observe varied currents on different flexible substrates, and we assume it's due to surface structures created by different grain size particles on top of substrates. The particle dispersion can cause unique geometric patterns on various substrates that can affect inter-particle spacing. On the other hand, chemical groups created on the material's surface during grinding also alter the current. In addition, flexible substrate's porosity is another factor that changes the film property. Comparatively, a paper towel has higher porous structures than AAO and Zap paper, which might have revealed the lower current. Nevertheless, increasing the volume of coating suspension on porous substrates reduces the interparticle distance, improving the current flow. ***Figure 3. 20 b*** shows a change in the electrical current with increased volume of the ground suspension.

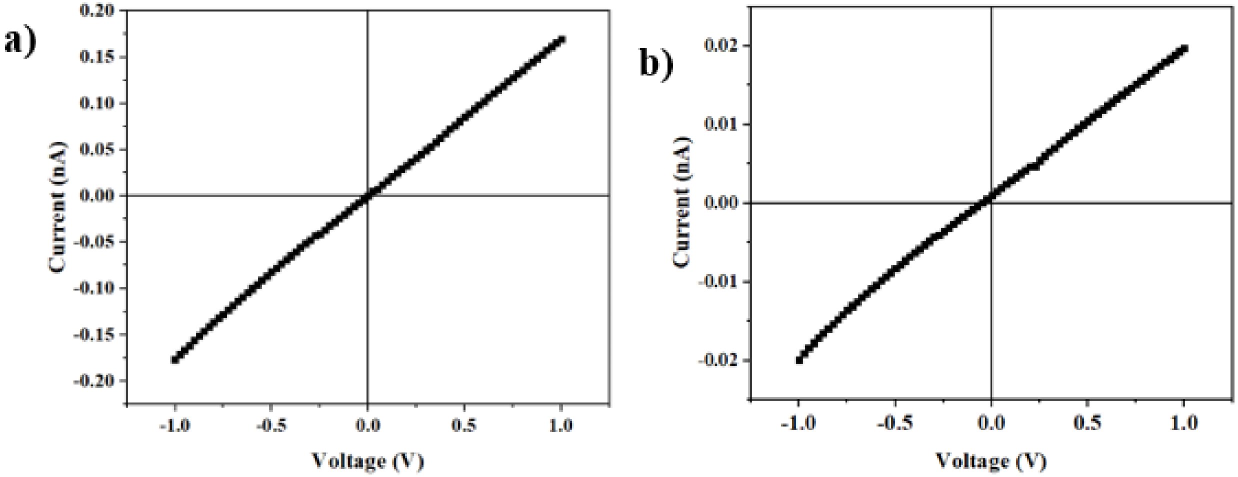

Figure 3. 19. Typical *I-V* plot for $TiSi_2$ thin film (ground in EG at 800 rpm for 10 min) (a) formed on Zap paper substrate (b) paper towel substrate. 2 µL suspension was used for preparing film.

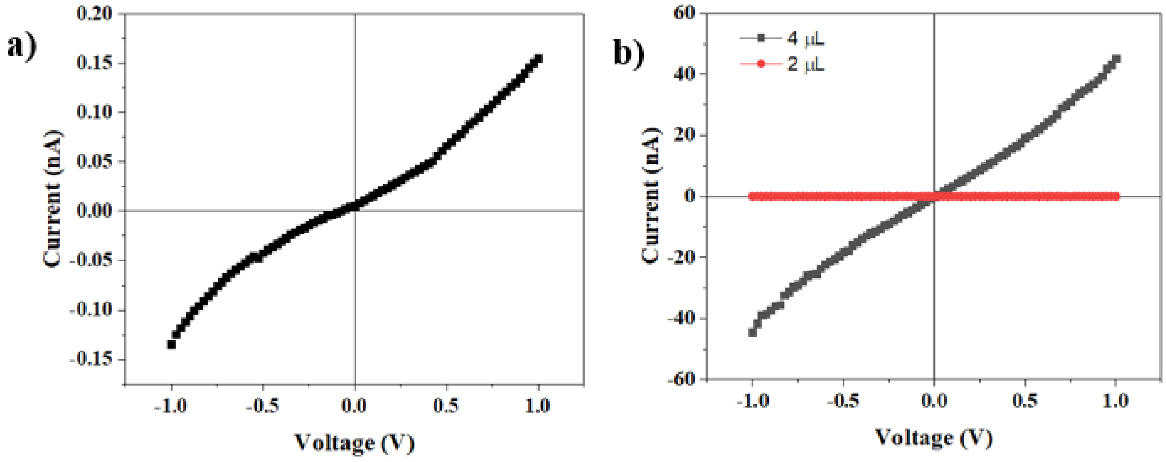

Figure 3. 20. (a) *I-V* plot for $TiSi_2$ thin film (ground in EG at 800 rpm for 10 min) on AAO substrate. 2 μL suspension was used for preparing film. (b) *I-V* plot of $TiSi_2$ thin film (ground in EG at 400 rpm for 10 min) on AAO substrate prepared using different volume of colloidal suspension.

Furthermore, we have coated the $TiSi_2$ suspension on a flexible substrate and have twisted (approx. 120^0) it before examining the electrical properties. This experiment was performed to find the change in the electrical current after twisting. Comparing the result between ***Figure 3. 19-a*** and ***Figure 3. 21***, it is seen that electrical current doesn't seem to be affected much. Therefore, it gives us a clear route that PBM colloidal suspension could also be coated on bendable substrates, which might be used for flexible devices such as transistors, solar cells memory devices, and sensors.

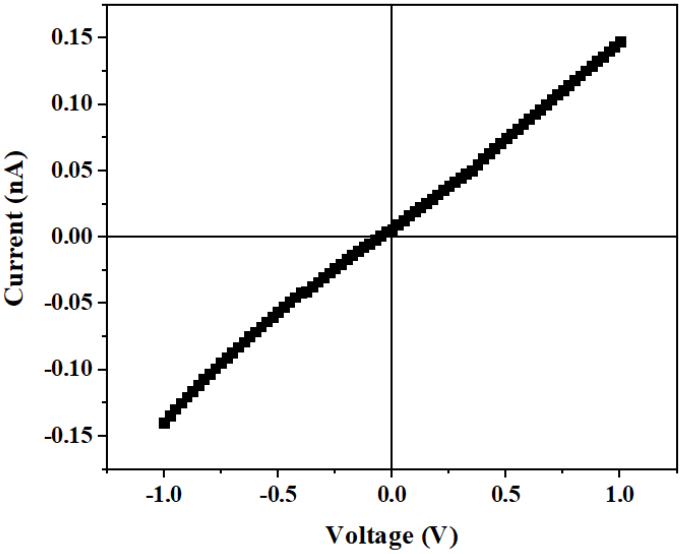

Figure 3. 21. Typical *I-V* plot for $TiSi_2$ thin film (ground in EG at 800 rpm for 10 min) measured on bendable Zap paper substrate. 2 µL suspension was used for preparing film.

3.4.3. Wettability compared between different grade nanostructured films

In this experiment, we have compared wettability behavior on two different types of silicon (low ((2N) 99.0%) and high purity ((5N) 99.999%)). For this, two different grade silicon powders were ground in IPA solvent using Fritsch PBM and drop casted on a glass substrate to create nanostructured films. Then, the wettability experiment was examined on these coated films with/without heat treatment. All prepared samples were initially dried at room temperature; however, annealed samples were further dried under an argon atmosphere. The analyzed data shows that annealed and non-annealed film of definite grade silicon, prepared at different grinding conditions (time/speed), follow a similar wettability trend. ***Figure 3. 22 (a)*** shows that contact angle in low purity silicon film increases with increasing grinding time for non-annealed samples.

We noticed the same behavior for annealed samples; however, contact angles were much lower than non-annealed samples. Similar case observed in ***Figure 3. 22 (b)*** for high purity silicon film. Most importantly, an increase in annealing time (at constant annealing temperature) or temperature (at constant annealing time) shows the decreased contact angle for both types of powders ***(Figure 3. 22 (c), (d)).*** After annealing, factors such as solvent, surface chemistry and particle morphology might affect the material characteristic and result in lower contact angles.

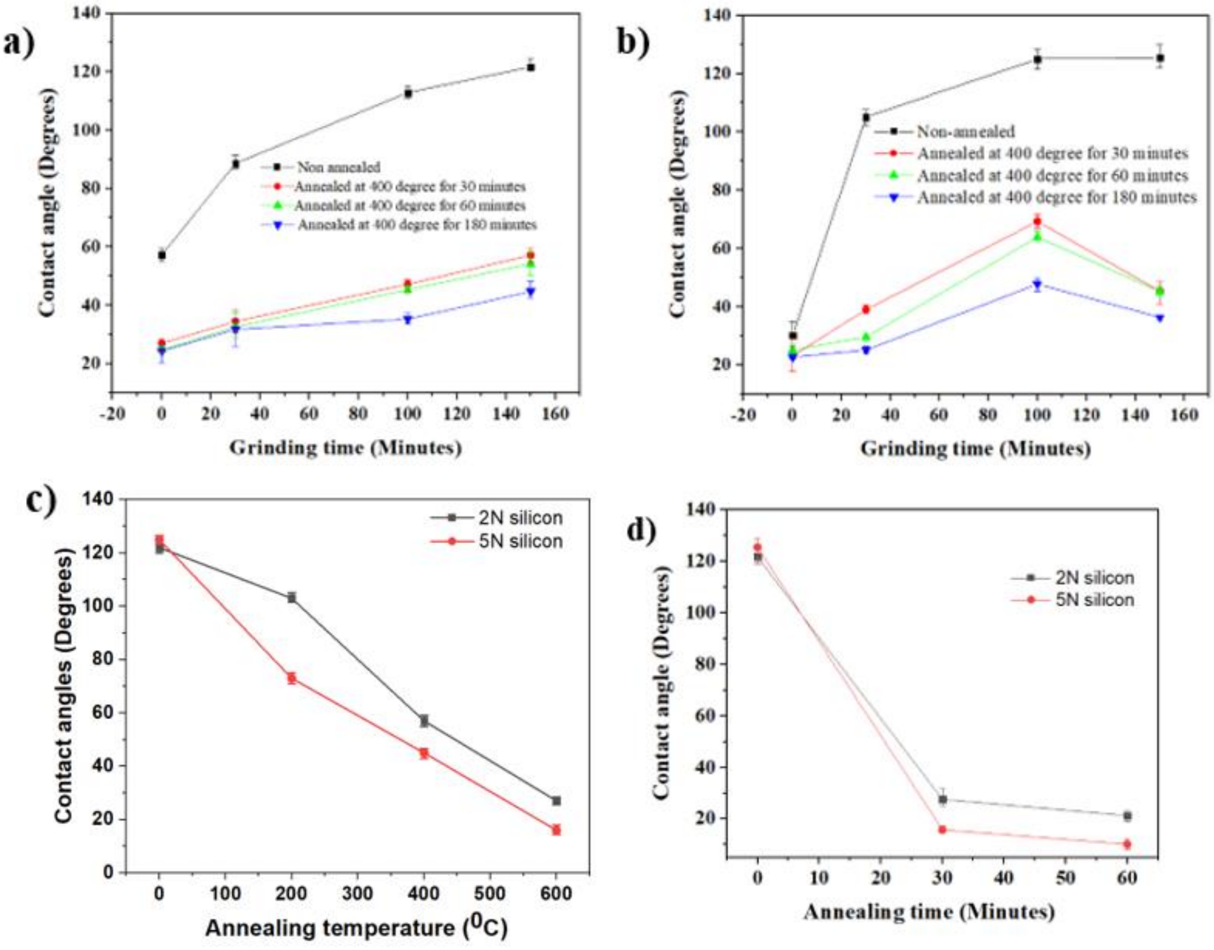

Figure 3. 22. Change in contact angle of the film annealed at 400 ^{0}C for different time. Film prepared from powder ground at 500 rpm for different time (a) Low purity silicon powder (b) High purity powder. Change in contact angle of low and high purity silicon film (powder ground at 500 rpm for 150 minutes)

(c) annealed for 30 minutes at different annealing temperature and (d) annealed at 600^0 C for different time (d). All samples were prepared on glass substrates.

Overall, we find that broad tuning of film wettability from hydrophilic to hydrophobic or vice-versa is possible by altering the combination of materials and solvents used during PBM, along with changing film surface roughness using different grinding speed and/or time. In addition, the increased film surface energy as particle size is reduced and changes in crystallinity may affect contact angle via nanoscale size effects and by altering the interactions with functional surface groups. Solvent type, functional groups and rheology on the nanoparticle surfaces will be important factors to determining the applications of the thin films produced by PBM [221,222]. Lastly, one may also introduce different organic compounds during the milling process [223] to specifically functionalize and/or passivate the nanoparticle surfaces for different uses [224–226].

3.5. Conclusion

In summary, we prepared and studied thin-film coatings consisting of silicon and titanium disilicide nanoparticles prepared via a colloidal nanogrinding technique. The prepared suspensions were covered on various substrates using different coating techniques. The fabricated nanostructured films show tunable properties on contact angle and electrical conductivity measurements. The effect of wettability and conductivity were examined on various types of rigid and flexible substrates with nanoparticle coating. The results show decreased contact angle with increased grinding condition (speed/time) for EG ground $TiSi_2$ film. In contrast, the contact angle increases in Si powder ground at different grinding times using IPA solvent. The impact of surface chemistry was also studied based on annealed $TiSi_2$ and Si films coated on rigid substrates. For this, we examined the wettability effect on both non-annealed and annealed films prepared from the silicon of different grades. The annealed films show a decrease in contact angle at different annealing conditions, implying the effect of surface reaction. Also, an improvement in conductivity was observed in the annealed film. Overall, nanogrinding allows the tunability of film properties that can lead to novel multi-functional coatings depending on the particular combination of material, solvent and nanoparticles geometries/dimensions used.

Chapter 4

4. Thin film gas sensor

Sahil Dawka [101] *(MEng graduate student) and Tanay Kumar (MITACS Globalink program) helped with some of the nanogrinding trials for the results in this chapter. The author worked on preparing most of nanogrinding trials used in this chapter. The author also worked on methodology and Pengjun Duan* [103] *(MEng graduate student) and Tanay Kumar (MITACS Globalink program) helped prepare nanostructured films using the doctor blading technique. Film characterization, investigation and analysis were performed by the author and Pengjun Duan. Anusha Venkataraman (PhD student) helped image the ZnO thin films via AFM. Parts of the results in this chapter were published in [J1].*

In this chapter, a thin film chemiresistive sensor that functions at room temperature was fabricated using ZnO colloidal suspension. All sensors fabricated for the gas sensing experiment were prepared from the doctor blading technique. Various factors (grinding parameters, humidity and temperature) that affect the gas sensing performance of different PBM nanoink sensors are presented in the subsequent sections.

4.1. Introduction

Nanostructured thin films and coatings find broad areas of application due to their unique properties, which is a result of both size and interface effects [160,227–233]**.** In particular, thin film gas sensing devices based on nanostructures are relevant for monitoring environmental gas concentration, controlling chemical processes, agricultural and medical applications [148,155,234,235]. The most common factors, such as grain size, microstructure, free charge concentration, sensitive layer morphology, geometry, specific materials reactivity, show the physical changes in surface conductivity. For efficient gas sensing, the film properties and structure play a vital role in sensor operation depending on particle size, porosity and the diffusion time of the gas species [166]. Nanoparticles have a larger relative surface area, thereby accelerating exchange with the surrounding atmosphere and leading to a larger detection signal to larger or bulk particles. High porosity of a nanoparticle sensing film also facilitates the rapid diffusion of the gas species and improves sensing performance. Similarly, gas homogenization time for nanoparticles can be several orders of magnitude smaller than for micron sized particles. Semiconducting metal oxide nanostructures have shown exceptional chemical, optical, mechanical and electrical properties for sensing [146,147,236]. Metal oxides show a large change in their electrical conductivity in the presence of various gas environments [236,237]**,** and thus by monitoring the variation of current (or resistance) through these films, they can function as sensitive gas detectors. Lowering the operating temperature needed for metal oxide gas sensors is an important goal, and room temperature operation, in particular, has attracted wide interest due to low-power consumption, portability, and cost-effectiveness [238]. Some approaches such as noble metal functionalization or creation of oxygen vacancy have addressed to a sensor to operate it at room temperature [168,239–241]. Several types of metal oxide films have been used for gas sensing applications [147–149] including TiO_2 [242], SnO_2 [150], and ZnO [151,243,244]. Among these, ZnO, a wide band gap (~ 3.34–3.37 eV) [153] semiconductor, is widely used for applications such as varistors [245], memristors [246], solar cells [99], piezoelectric devices [247], and light emitting diodes (LED) [114]. Low resistivity, non-toxicity, large exciton binding energy, different nanostructured geometries, along with high surface-to-volume ratios make ZnO nanoparticles an excellent choice for optoelectronic and gas/vapor sensing applications [100,116]. ZnO is considered a "chemoresistive" sensing material wherein the presence/absence of adsorbed oxygen species on its surface alters the amount of free carriers available to participate in charge transport [148,151], which can be used to sense, e.g., oxygen [243], hydrogen [240], ethanol [248], NO_x [249], acetone [250], NH_3 [251] and CO [252].

The gas sensing performance of ZnO-based gas sensors mainly relies on its working temperature that alters the reaction kinetics, conductivity, and electron mobility. Traditional sensors use the elevated temperatures, which enhance the adsorption-desorption mechanism by lowering the activation energy. The use of high temperature limits ZnO sensors broad applications because high temperatures operation not only signifies energy waste but also can cause gas explosion due to flammable and explosive gases which have low ignition point at ambient temperature [153]. Additionally, high temperature can also cause sensor instability, thereby leading to incorrect test results. Therefore, a ZnO sensor that operates at room temperature is a must.

Mainly, ZnO films can be prepared via various fabrication techniques including chemical vapor deposition [253,254], atomic layer deposition [168,255], sputtering [249], spray pyrolysis

[256], pulsed laser deposition [257], sol–gel [171] and ball milling [95,258–260]. In addition, various low-cost solution-based deposition techniques: drop casting [171]; spin coating [252]; doctor blading [248]; screen printing [261] and ink jet printing [262], have been adopted to produce ZnO thin films on various substrates. For example, doctor blading is often used due to its simplicity, cost-effectiveness, uniform and quick deposition, low energy and minimal requirements for the suspension/ink [263]. Planetary ball milling (PBM) is known for its ability to reliably mass produce nanoscale particles in appropriate solvents by grinding high-purity bulk powders [60,95,122,264–267] without any complicated physical or chemical procedure. These techniques are very energy efficient by utilizing the high-impact forces during rotary motion of a grinding jar containing the sample, grinding beads and a liquid medium, arranged eccentrically on a so-called sun wheel, which facilitates the rapid production of nanostructured thin films in an inexpensive manner. They have also been used to produce nanoscale suspensions, or nanoinks, of ZnO for various applications including antibacterial materials [95], varistors [259], catalysts [268], antifouling [269] and anode materials [270], luminescence [271], composites and alloys [152,272,273], gas sensors [274–277], UV sensor and photodetector [278–280]. The PBM process depends on various configurable parameters such as speed of revolution, milling time, and the ratio of beads to feed material. The grinding parameters and solvent used influence the properties and size distribution of the resulting nanoparticle inks and thin films [60], which can be optimized for different applications, including gas sensing.

In this chapter, we will apply the PBM and doctor blading technique to produce ZnO nanoparticle thin film gas sensors that operate at room temperature via changes in resistance upon exposure to different gas species. By varying grinding parameters and examining the effect on nanoparticle structure and electrical characteristics of the resultant films we are able to tune the response signal magnitude and response/recovery times of ZnO gas sensor devices. Tests conducted in dry/humid air and different target gas environments allow us to study the ZnO film fabrication conditions required for optimal gas sensing and validate the feasibility of using PBM nanoinks as the active material for thin film gas sensors.

4.2. Materials and Methods

4.2.1. Materials

Zinc oxide powder (ZnO; Anachemia), ethylene glycol (EG; 99% purity, BDH), deionized water (DI water), and high-purity gases and extra dry air (Praxair) were used as received. Glass slides were used as flat substrates for thin film coatings. Stainless steel single edge razor blades (GEM) were used for doctor blading. Conductive silver paint (Ted Pella) and copper tape (3M) was used to make electrical contacts to ZnO films.

4.2.2. Nanostructured thin film preparation and sensor fabrication

PBM was performed using a Fritsch Pulverisette 7 planetary micro mill (premium line) (silicon nitride grinding jars, 80 mL capacity: zirconia grinding beads, 2 mm in diameter). In a typical experiment, ZnO powder (~7 g) was ground in approximately 10 mL of either EG or DI water solvent (a.k.a. colloidal grinding) with approximately 100 g of beads. The grinding speed and time were varied between 200 and 1000 rpm and 10 min. and 60 min. (in cycles of 5 min.

grinding; 5 min. resting), respectively. After the completion of each grinding trial, a syringe and stainless-steel mesh were used to extract and separate the resulting PBM nanoink suspension from the grinding beads. Several films of each of the ground ZnO trials were prepared for characterization via doctor blading on substrates: A few µL of ZnO nanoink was used to coat the surface by sweeping the blade across the substrate (masked with a single layer of Scotch tape) along with the suspension (blade angle 20-30^0). The film thickness for all prepared sensors were approximately 60 µm (based on scotch tape thickness). The coatings were dried at ~ 100 ^{0}C on a hotplate for approximately 5 minutes. For thin film surface imaging, a Nanonics Multiview 1000 atomic force microscope (AFM) with Olympus BXFM optical microscope was employed. Additionally, Raman scattering measurements of thin film samples were performed using a Renishaw inVia Raman microscope. Raman spectra were collected using 632.8 nm HeNe laser line under ambient conditions. Photoluminescence (PL) spectra were acquired using an Olympus FV1000 confocal laser scanning microscope with solid state laser line of wavelength 405 nm. Scanning electron microscopy (SEM) and energy dispersive X-ray analysis (EDX) were performed using a Hitachi S-2600. The thin film porosity analysis is performed using ImageJ (version 1.46r) [208]. To analyze the porosity and particle size, the SEM/AFM greyscale image are first open on ImageJ software. We then adjust the threshold and analyze the particle. The output results will give information about porous area (in %) of the resultant film. Porosity is averaged out from the multiple images of respective sample's SEM and AFM data. Similarly, for particle size analysis (image does not have to be in greyscale), we first set the scale in the ImageJ software and manually draw a diagonal line on particle size and measure the length of that respective particles. We measure as many as particles that is possible for measurement from the SEM/AFM images. Final particle size is averaged for the respective sample from the collective data of SEM and AFM images. In order to create the gas sensor devices, two electrical contacts to the resulting films were made using silver paint and copper tape (see ***Figure 4. 1 (a)***) followed by drying in a mechanical oven for 10-15 minutes at 75 ^{0}C.

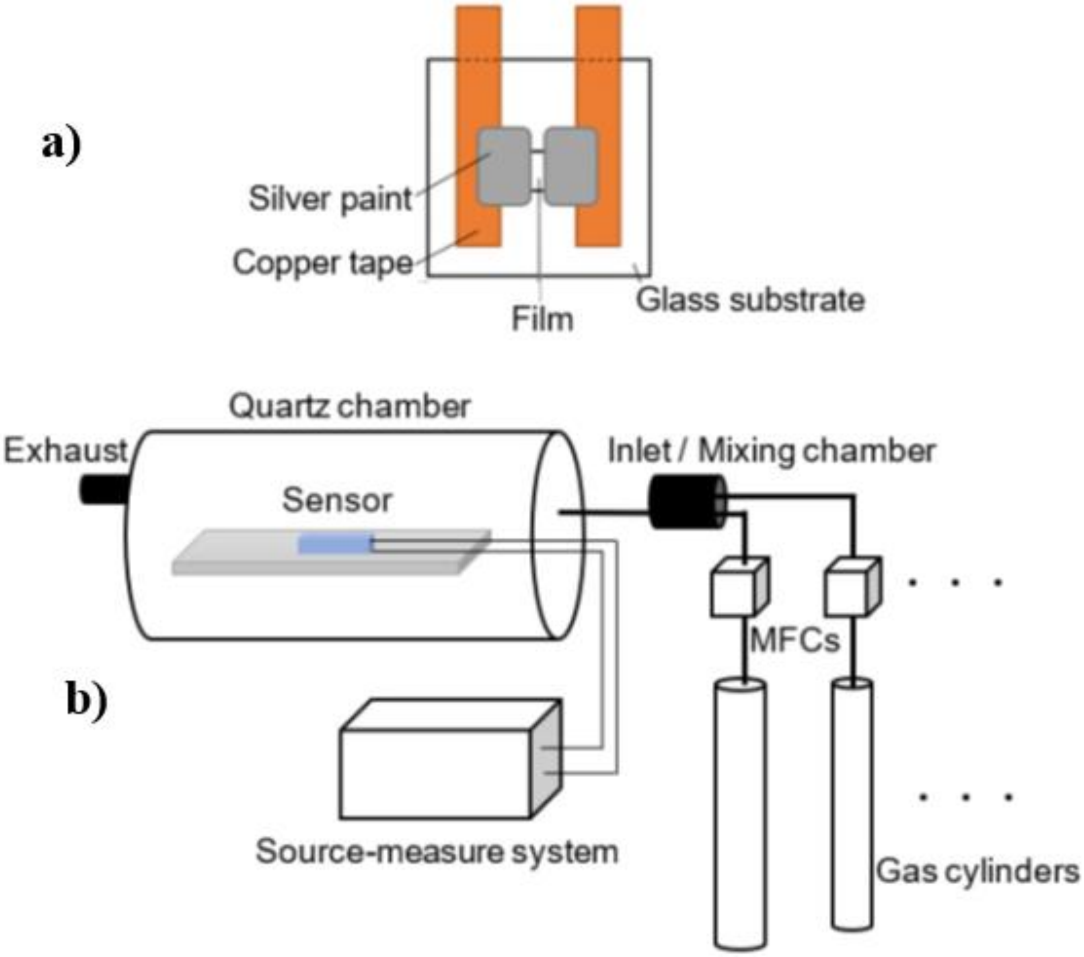

Figure 4. 1. (a) Schematic diagram of thin film gas sensor devices: Copper tape on glass substrates containing doctor bladed ZnO film served as the electrode contacts and silver paint were used for connecting sensor film to electrodes. (b) Illustration of the gas sensing apparatus used. The sensor was placed inside a quartz chamber connected to gas cylinders (carrier and/or target gas) through MFCs. Cu wires are connected to the sample via a hermetic feedthrough for electrical measurements. The electrical response of the sensor was monitored using a precision source-measure system.

4.2.3. Sensor characterization

The gas sensing studies were conducted using the setup shown in ***Figure 4. 1 (b)*** under ambient pressure and temperature (approx. 22 ^{0}C), which consisted of quartz tube chamber connected to a precision electrical source-measure system (Keithley 4200-SCS) and compressed gas source(s) (target/carrier species) through mass flow controllers (MFCs). Two-terminal current-voltage (*I-V*) characteristics, and current response versus time of the ZnO film sensors were measured in different gas environments. Before injecting target gases inside the chamber, a baseline sensor behavior in dry air carrier gas was determined. Relative humidity (RH) inside the test chamber was measured using a Digi-Sense 20250-11 pre-calibrated thermo-hygrometer. All experiments were performed under ambient room light.

4.3. Results and Discussion

4.3.1. Film Morphology and material characterization

An optical microscope image of a typical ZnO thin film coating formed using PBM nanoink and doctor blading is shown in the inset of ***Figure 4.2 (a)***. The coatings displayed good uniformity, stability and adhesion under ambient conditions and up to 200 ^{0}C. The SEM image in ***Figure 4.2 (a)*** shows the milled ZnO films consist of fine nanostructured particles with distributed pores. The ZnO film surface topography was further characterized using AFM (***Figure 4.2 (b))***: As expected, particles were ground into finer sizes as grinding speed was increased and we observed a reduction in root mean square (RMS) film roughness, as measured with AFM (***Figure***

4.2 (c)), which drops below 80 nm for grinding at 1000 rpm for 10 minutes. Higher grinding speed also concurrently reduces particle size below 100 nm (***Figure 4.2 (d))***. For ZnO powder ground using EG at lower grinding conditions (200 rpm for 10 min) had produced the smaller particle size up to 150 nm with average particle size at approximately around 300 nm range; and when ground at the higher grinding condition (1000 rpm for 10 min) produced the particle size below 50 nm, where the average particle size lies approximately close to 100 nm. A similar decreasing trend in particle size/film roughness was observed as grinding time was increased (at constant rpm) (***Figure 4.2 (e))***[60]. Some authors claim that increase in surface roughness enhances the gas sensing performance of ZnO films [281,282]. The experimental research shows that AFM analyzed film only give information about particle size, while XRD provide sample's grain size [283]. Therefore, we believe that ZnO ground at higher grinding condition (speed/time) have much finer grain size compared to lower grinding condition.

The photoluminescence spectrum of a typical film is shown in ***Figure 4.2 (f)***. The milled ZnO thin films showed five different peaks of various intensity levels at different wavelength ranges, which can be correlated with the electronic and structural properties of the milled particles: Consistent with previous studies, the 465 nm peak (blue emission band) is attributed to deep level emission originating from oxygen vacancies or interstitial zinc ions of ZnO [284]. The green emission (525 nm) is due to singly ionized oxygen vacancy or oxygen antisite defect O_{Zn} [264]. Similarly, the peak at 577 nm is most likely due to disorder at the surface of nanoparticles after milling [264]. Lastly, the other peaks 590 nm and 650 nm emission are usually attributed to oxygen vacancies [285,286]. Likewise, a typical Raman spectrum for both milled and bulk powder are shown in ***Figure 4.2 (g)*** and ***(h)***. ZnO powder (bulk) often has a wurtzite structure and there are two A_1, two E_1, two E_2 and two B_1 modes in Raman spectra of its crystal structure [178]. The most common Raman intensive E_2 (low) mode at ~99 cm^{-1} is just beyond the range of our detection, however, the other Raman mode E_2 (high) at ~437 cm^{-1} is visible, which is assigned to oxygen vibrational modes [177]. E_2 (high) mode is most prominent in the starting material; after milling the intensity of peak reduces and gets broadened. Lowered intensity and peak broadening of 437 cm^{-1} peak indicate a change in band structure and crystallinity of nanostructures after milling. The Raman spectra of both ground and bulk powder display three different peaks at about 206, 329, 379 and 412 cm^{-1}, where these peaks are attributed to 2TA;2E_2, E_2(high)-E_2(low), A_1(TO) and E_1 (TO) symmetry, respectively [177]. However, broader Raman peaks and lower intensity are attributed to size effects, lattice strain and lower crystallinity [264,287]. The decrease in crystallinity is attributed to defects produced during ball milling. For the milled nanoparticles, we observed a broad peak around 580 cm^{-1} that became more prominent for longer grinding time or higher speeds. It is predicated that peaks with high intensity from 560 to 580 cm^{-1} indicate the presence of defects related to oxygen vacancy (V_o) and/or zinc interstitial (Zn_i) [176,177], which could be advantageous for gas sensing [168]. The milling media (grinding beads, solvents) can also affect the particles but this is likely only significant for longer grinding times and/or higher speeds (see red curve ***Figure 4.2 (h)*** – the peak at 189 cm^{-1} is assumed to be related to the zirconia grinding beads [288]. The intermediate region in the spectrum of ground ZnO powder, the second-order Raman modes with A1 symmetry (between 756 -850 cm^{-1}), are mostly weak and hardly detected.

The EDX results for our ZnO gas sensor films (***Figure 4.2*** **(i)**) confirmed the presence Zn and O elements with an average atomic percentage of 48.05 and 51.95 respectively. The oxygen content percentage in the milled powder is likely affected by milling time and medium (e.g., solvents) [264,289,290]. In general, ball milling can also cause contamination from the grinding jar and beads [264,290], however our EDX results did not indicate the presence of appreciable elemental impurities for the PBM nanoinks studied.

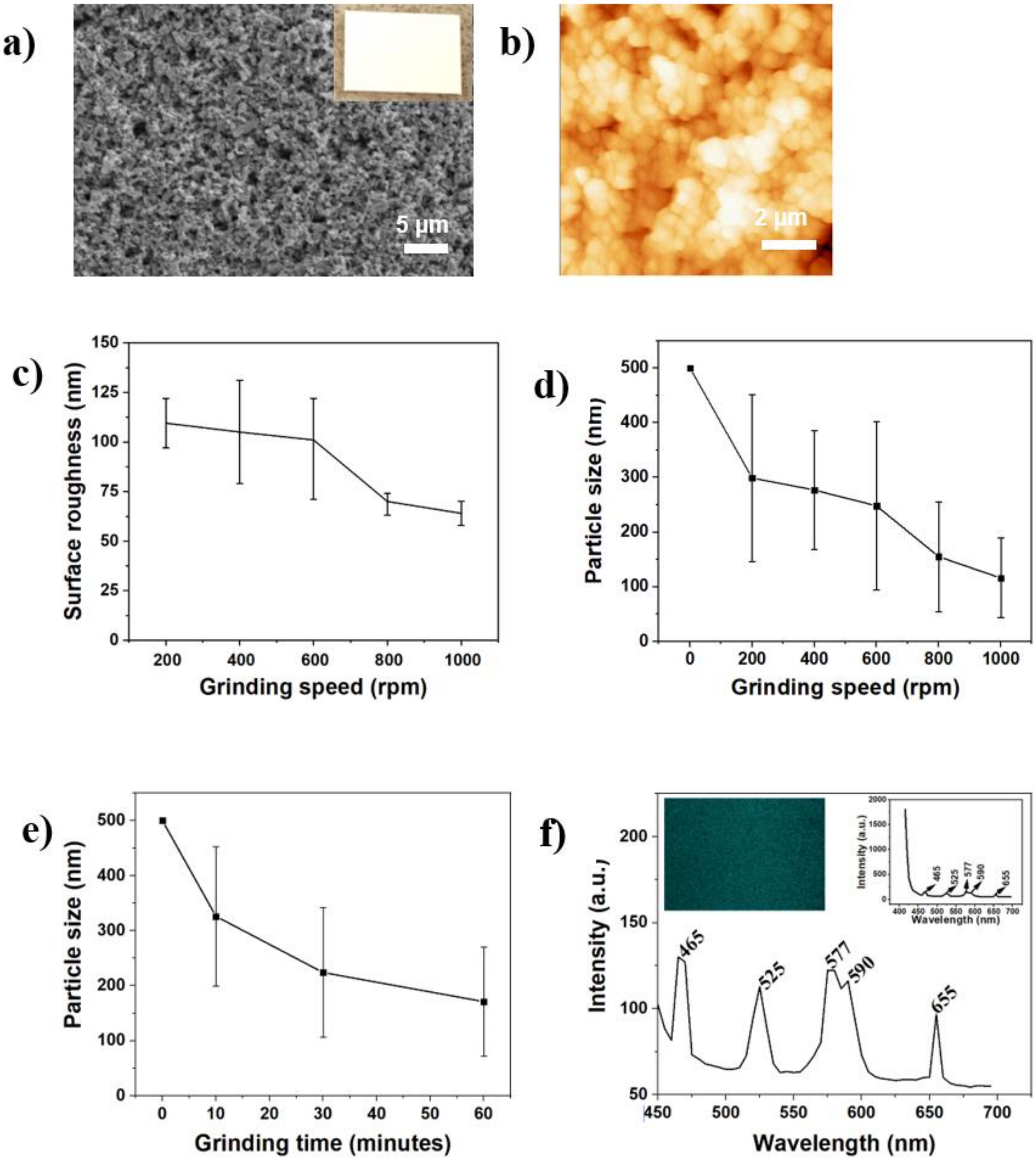

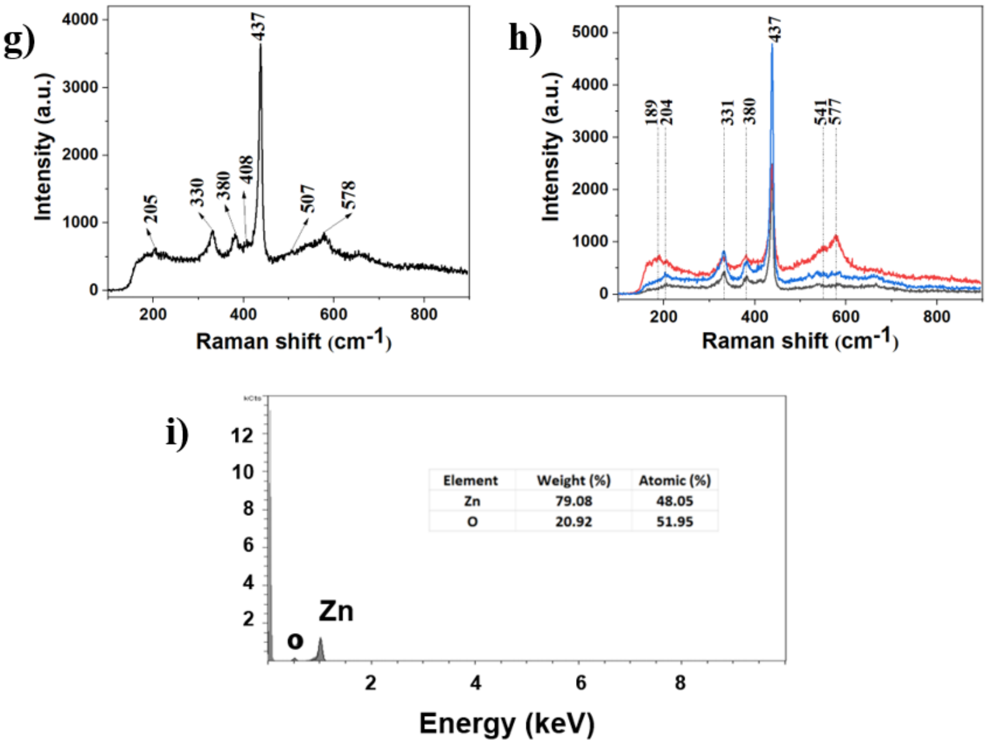

Element	Weight (%)	Atomic (%)
Zn	79.08	48.05
O	20.92	51.95

Figure 4.2. (a) SEM image of milled ZnO nanoparticles ground with DI water at 200 rpm for 30 min. The inset is an optical microscope image of doctor bladed ZnO thin film on glass substrate. (b) AFM images of ZnO film prepared using PBM nanoink with DI water ground at 200 rpm for 10 min. (c) Plot of RMS roughness from AFM of ZnO thin films using PBM nanoink ground in EG for 10 min. at different speeds. Average particle size of ZnO particle obtained from AFM and SEM data of thin film using PBM nanoink ground (d) EG for 10 min. at different speeds and (e) DI water at 200 rpm for different grinding time, (data at 0 rpm/min denote nominal starting bulk powder particle size). (f) Photoluminescence spectra for approximately 450-700 nm of ZnO thin film ground at 200 rpm for 60 minutes using DI water solvent (inset (left) optical map image of total PL intensity obtained for 415-715 nm and (right) overall range averaged full spectrum). (g) Raman spectra of ZnO ground film prepared using DI water ground at 200 rpm for 60 minutes. (h) Raman spectra of different ZnO films ground (EG solvent) and unground: black, bulk sample; blue, ground at 200 rpm for 10 minutes; red, ground at 750 rpm for 90 minutes. (i) EDX spectrum of ZnO film using PBM nanoink ground at 600 rpm for 10 minutes in EG solvent.

4.3.2. Gas sensing results

Figure 4. 3 shows current (at +2 V applied bias) vs. time and *I-V* curves for ZnO thin film sensors formed using the PBM nanoinks. In ***Figure 4. 3 (a)*** the current levels vs. time for a flow sequence of dry air/pure argon/dry air are shown (similar behavior was observed for nitrogen target gas environments). The time-dependent sensor response was observed upon exposure to a target gas atmosphere after reaching a minimum in pure dry air flow whereby output current rises upon injection target gas source(s) and falls upon release of the gas (and re-exposure to dry air/oxygen). Accordingly, the resistance of the sensor undergoes a decrease as it exposed to a target and an increase as dry air was reintroduced. Initially, the sensor sample current (in ambient atmosphere) was observed to increase and started to decrease as soon as dry air was introduced, indicating that the response of the ZnO gas thin film sensors are also strongly dependent on operating atmospheric humidity or RH. The humidity or moisture sensing ability of our ZnO films was confirmed by the resistance data shown in ***Figure 4. 3 (b),*** which shows a large sensor response vs. RH. The resistance is approximately one order of magnitude changed from dry condition (~2 % RH) to 50 % RH.

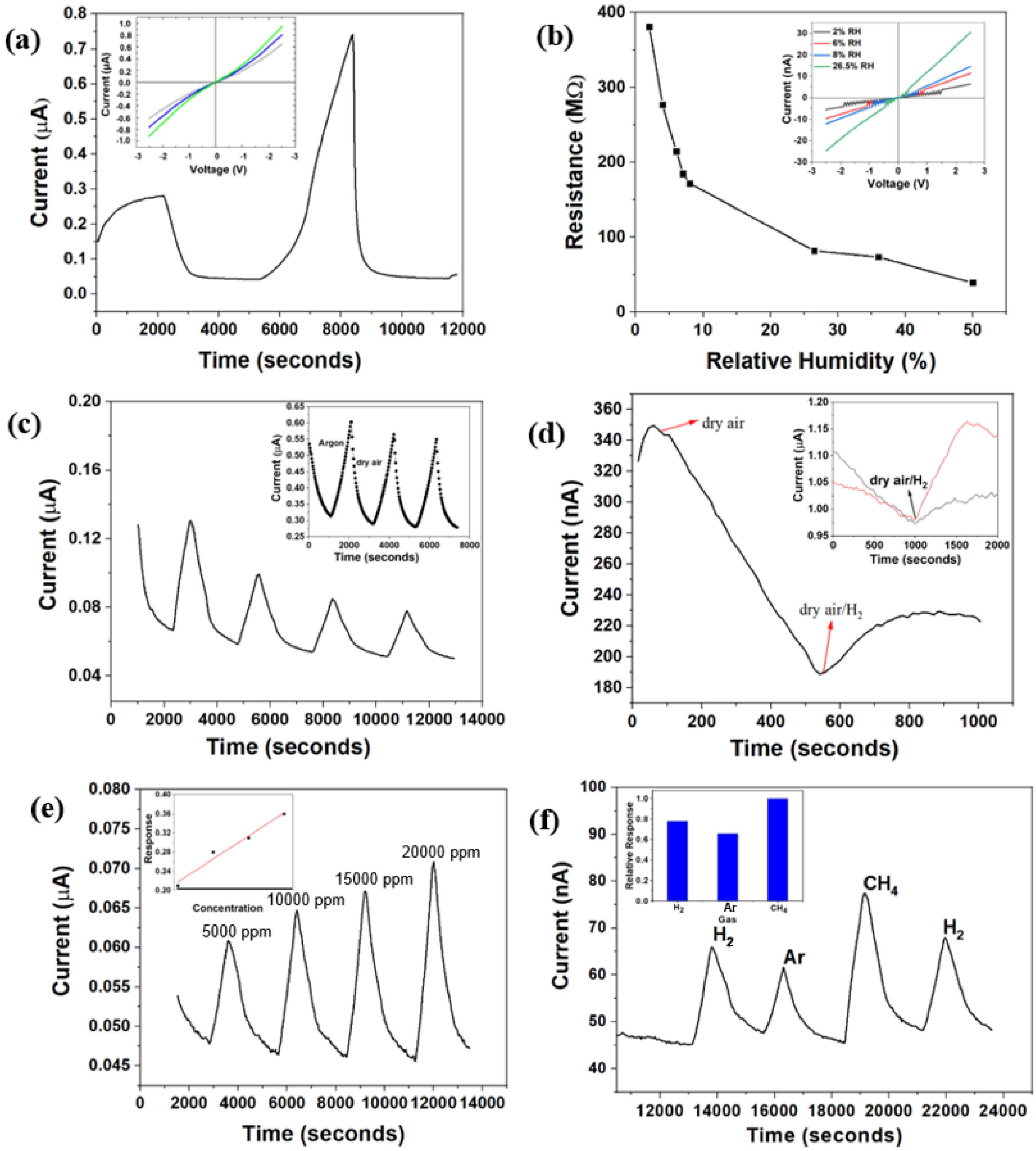

Figure 4. 3. (a) Time dependence of sensor current upon exposure to dry air (~ 2000 s mark) followed by pure argon gas (~ 5500 s mark) and then dry air again (~ 8000 s mark) (all flows 500 sccm) for ZnO thin film sensors formed using PBM nanoinks ground for 10 minutes in EG (400 rpm). Inset shows *I*-*V* plots as current increases near start of argon flow. (b) Resistance vs. RH for a ZnO thin film sensor formed using PBM nanoinks ground at 200 rpm for 30 minutes in DI water. Inset shows individual *I*-*V* plots for different humidity values. (c) Gas sensor (prepared using nanoinks ground at 400 rpm for 10 min in EG solvent)

showing approach to stable baseline vs. time during repeated exposure to 250 sccm of H_2 pulses. Inset shows sensor current vs. time for a similar sequence of on/off dry air/argon gas pulses for ZnO thin film sensor formed using PBM nanoinks ground for 10 minutes in EG (600 rpm). (d) Sensor current vs. time for 500 sccm dry air followed by 400 sccm dry air/100 sccm hydrogen (sensor formed using PBM nanoinks ground for 10 minutes in EG (600 rpm)). Inset shows current vs. time for ZnO sensor (prepared using nanoinks ground at 400 rpm for 10 min in EG solvent) exposed to 450 sccm dry air/50 sccm hydrogen (red curve) and 475 sccm dry air/25 sccm hydrogen (black curve). (e) Current vs. time for ZnO thin film sensor (prepared using PBM nanoinks ground at 400 rpm for 10 minutes in EG solvent) at different H_2 gas concentrations indicated. Inset shows response as a function of gas concentration. (f) Current vs. time for ZnO thin film sensor (sample as in (e)) when exposed to different gases (hydrogen, argon and methane). Inset shows relative response or selectivity to different target gas species.

The target gas response of our sensors was repeatable over multiple flow sequences; however, due to the size of the test quartz chamber and maximum flow rate used (in addition to the film thickness), it took some time to reach a stable baseline as displayed in ***Figure 4. 3 (c),*** which shows the sensor stabilizing after approximately 2.5 h. Also, size of testing chamber will affect the stability and response time of the sensor [6]. In addition, sensing with dry air as the carrier gas to balance the target species was also possible using our PBM nanoink sensors, as evidenced by the detection of hydrogen in ***Figure 4. 3 (d)***, which shows sensor current is proportional to target gas concentration. Further study of sensor response was performed for a sequence of hydrogen gas concentrations ranging from 5000 to 20,000 ppm ***(Figure 4. 3 (e))***, which showed a linear response region **(*Figure 4. 3 (e), inset)***, with a sensitivity of approximately 2.4 x 10^{-2} ppm^{-1}. Furthermore, sensor selectivity was tested by exposure to the same concentration for different gas species ***(Figure 4. 3 (f))***, indicating a strong response to methane, followed by hydrogen and argon, which shows potential for selective gas sensing ***(Figure 4. 3 (f), inset)***. Preferential adsorption of different gas molecules [290] likely leads to the sensor selectivity we observed at room temperature. Most importantly selectivity is related with the different activation energy of target gases for adsorption, desorption and reaction on sensor surface [291]. Upon cycling back to the first gas pulse (H_2), the original sensor signal returned. In general, the gas sensor devices studied gave stable and reproducible responses that stayed within 25% of the original signal after several months. Since our prepared sensor was able to operate at room temperature, it was likely able withstand and perform effectively for multiple months. Apart from that, prepared nanostructured film was crack/break free even after several measurements, proving colloidal suspension with stable adhesion for several months. At present, there is not a recognized method to improve stability of ZnO-based gas sensors. However, stability can be enhanced to some extent by calcination/annealing as the post annealing treatments [164,292]. The gas sensing response is usually defined as the ratio of resistances in two different gas atmospheres. In order to compare the performance of gas sensors prepared using PBM nanoinks with different grinding conditions, the sensor response [156,169] was calculated as

$$\mathrm{S} = \frac{R_a - R_g}{R_a} \qquad (10)$$

where R_a and R_g are the sensor resistance in dry air and in the presence of target gas, respectively.

Figure 4. 4 compares the effects of different grinding parameters (speed/time/solvent) on gas sensor response in the presence of argon target gas. It can be seen in ***Figure 4. 4 (a)*** that sensor response decreases with grinding speed beyond 400 rpm, possibly due to particle agglomeration and porosity variations (see ***section 4.3.3***). Response can also be seen to increase with grinding time, peaking near 30 minutes for a constant grinding speed of 200 rpm ***(Figure 4. 4 (b))***. Grinding of materials using high energy ball milling can produce both surface and bulk defects. It is possible that surface defects would enhance gas sensing performance by exposing adsorption sites, whereas

bulk defects could limit the adsorption surface area [264]. The presence of surface defects such as Zn_i^- and V_o^-related defects is indicated in the Raman data (560 - 590 cm^{-1}) of ***Figure 4.2 (g)*** and ***(h)***, as grinding was increased. This could lead to a significant increase in gas sensor response because more oxygen molecules can be easily absorbed and ionized on the surface of ZnO [293]. However, grinding at higher speed or for a longer time can also give rise to bulk defects; therefore, it is anticipated that there will be a point at which bulk defects arise during grinding, resulting in lower response, which is discussed further below.

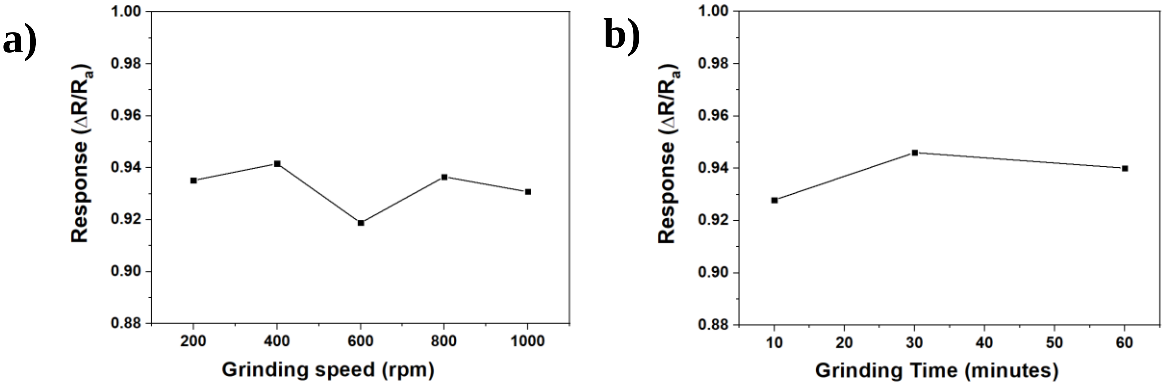

Figure 4. 4. Response of different gas sensors made from ground PBM ZnO nanoinks towards argon gas. (a) Films prepared using EG solvent at different grinding speed for constant grinding time of 10 minutes. (b) Film prepared using DI water solvent at different grinding times for a constant grinding speed of 200 rpm.

4.3.3. Gas sensing mechanism and data analysis

A key characteristic of sensing performance is the response/recovery time of the sensor. Response time is usually defined as the time required for a sensor to reach 90% of the total response of the signal such as resistance upon exposure to the target gas [156]. Likewise, recovery time is typically defined as the time required for a sensor to return to within 10% of the original signal upon removal the target gas [156]. The response and recovery times depend upon diffusion path (distance travelled by gas molecules the nanoparticle sensing surface), film porosity and particle agglomeration [157,166,294,295]. Based on our results (***Figure 4. 5 (a)***), sensors prepared from PBM nanoinks with lower grinding speeds have faster response times compared to sensors prepared from higher grinding speeds, with response time reaching a maximum near 600 rpm before decreasing again at higher speeds. Similarly, increased grinding time also appears to increase response time with a leveling off near 30 minutes observed **(*Figure 4. 5 (c)*).** Gas sensor recovery time generally increased with grinding speed up to 600 rpm before dipping at 800 rpm **(*Figure 4. 5 (b)*),** while a grinding time of approximately 30 minutes also displayed a dip (***Figure 4. 5 (d)***) indicating a faster sensor recovery. In general, to have an effective sensor that responds/recovers quickly one should choose the optimal combination of nanoink grinding conditions and based on ***Figure 4. 5*** this appears to occur for low to moderate grinding speeds (200-400 rpm) and moderate grinding times (~ 30 min.) for the devices studied, or potentially higher grinding speed (~ 800 rpm) with short grinding times (~ 10 min.)

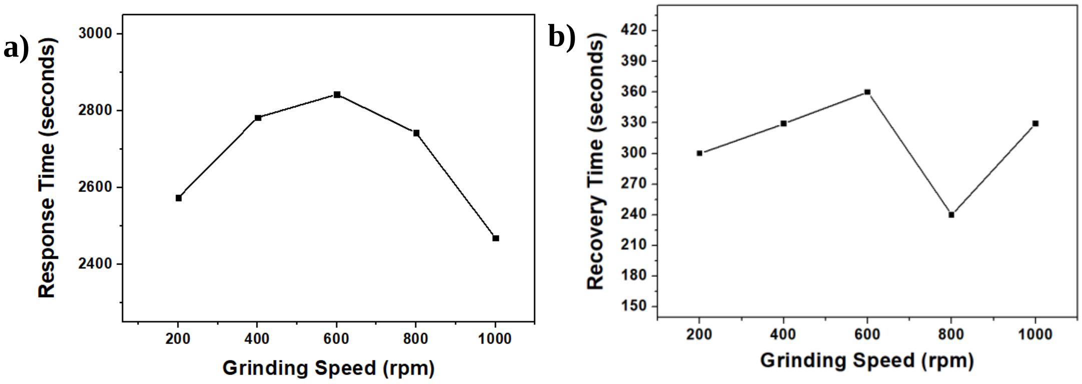

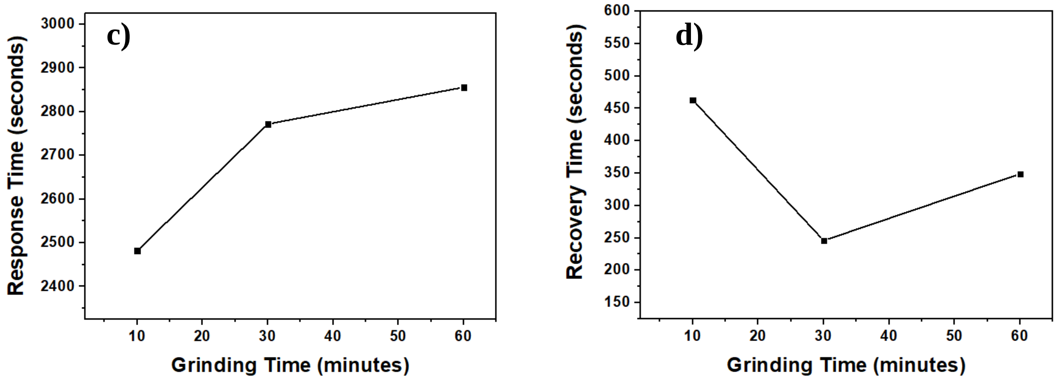

Figure 4. 5. Test gas (argon) response time (a) and recovery time (b) of sensors prepared from ZnO nanoinks ground at different speed for constant grinding time of 10 minutes using EG solvent. Response time (c) and recovery time (d) of sensors prepared from ZnO nanoinks ground at constant speed of 200 rpm for different grinding times using DI water solvent.

As mentioned earlier, the response of nanostructured thin film gas sensors is related to particle size and porosity. ***Figure 4.2 (c)-(e)*** shows that grinding at higher speed or for a longer time tend to result in smaller particle sizes. The smaller particle size is accompanied by an increase in the total sensing surface area; thus, sensor performance is proportional to the decrease in grain size [166]. This explains the increase in sensor response (***Figure 4. 4)*** as grinding speed approaches 400 rpm and grinding time reaches 30 minutes. As particle size decreases further (< 200 nm), it is possible that the nanoparticles suffer from increased agglomeration, which reduces the effective surface area and thus the free surface energy [296–298] (in addition, a large particle size dispersion as in the 600 rpm sample of ***Figure 4.2 (d)*** may exacerbate this effect). The influence of agglomeration is consistent with the decreased porosity observed for the sample made with nanoink milled at a higher rpm (see ***(Figure 4.6 (a))*** [154]. Lower porosity could also explain the faster response/recovery times observed for some samples in ***Figure 4. 5.*** Further to the material characterization data in ***Section 4.3.1***, grinding of the ZnO material eventually leads to an increase in surface and bulk defects. In general, the defect density on the surface is considered higher than in the bulk [299]. Surface defects function as (i) charge carrier traps and (ii) adsorption sites improving the electron-hole separation [300]. Bulk defects, on the other hand, serve as recombination sites [301]. Thus, the influence of grinding on the gas sensing behavior is dependent on the ratio of bulk-to-surface defects. Initially, as the grinding time/speed increases, the ratio of bulk-to-surface defects decreases, which can be attributed to increase in the total surface area leading to comparatively higher surface defects. However, based on our results at higher grinding speeds and for a longer time, this ratio seems to increase due to the formation of excess bulk defects, which may be attributed to bulk crystal distortion caused by excess mechanical attrition.

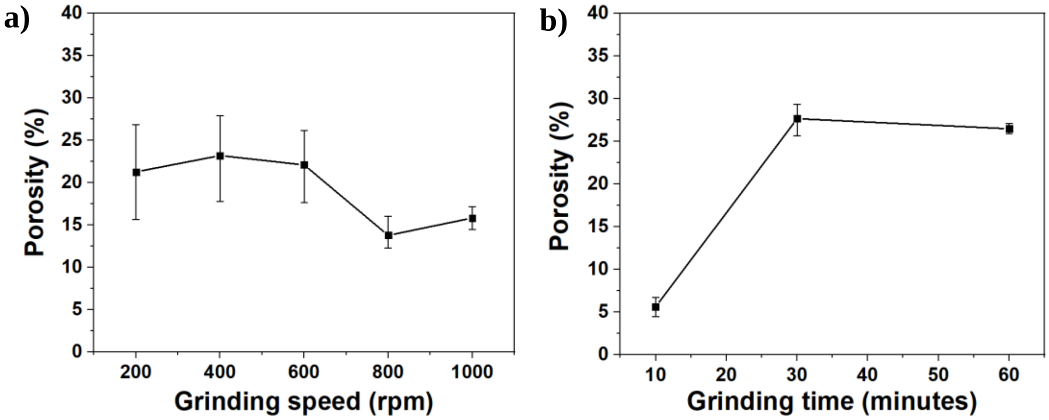

Figure 4.6. Porosity of sensors prepared using ZnO nanoinks obtained from AFM and SEM data. (a) Sensor prepared using EG solvent for different grinding speeds at constant grinding time of 10 minutes. (b) Sensor prepared from DI water solvent at different grinding times for constant grinding speed of 200 rpm.

Factors affecting the thin film sensor

The particle size/shape, surface area and the porosity on ZnO film have a major effect on the sensor performance via increasing the proportion of electron depletion layer in the entire film. ZnO materials can form the electron depletion regions with the thickness of one Debye length on their surface after reacting with oxygen in air [302]. When the grain size (or diameter) of ZnO materials is less than twice of the Debye length, the entire nanomaterials will become an electron depletion region, in other words, the entire material can take part in exchanging electron, and not just surface [147]. In such case, the sensor response usually increases significantly as particle size reduces. However, randomly decreasing the particle size can enhance particle agglomeration and reduce the size of exposed surface area. Therefore, adjusting the optimal particle size is very important in avoiding particle agglomeration, promoting gas diffusion and their synergy effects are vital for creating a sensor that works at low/room temperature [302]. For the milled nanoparticles prepared from higher grinding condition (speed/time), the decrease in particles sizes, tends to suffer from higher agglomeration that ultimately likely reduces the active surface area for gas diffusion, thus lowering the sensor response.

On the other hand, different morphologies of ZnO are also responsible for altering the various sensor performances. Ball milling can produces the nanoparticles with various morphologies (as observed under SEM and AFM images). The different morphological particle of ZnO leads to different gas diffusion capacities during the adsorption-desorption process of gas molecules. For instance, one-dimensional (1D) structures like nanowires, nanorods, nanotubes etc., have high surface to volume ratio leading to greater electron depletion [75]. Such behavior of these nanostructures will enhance the surface reaction, reduces the operating temperature and finally achieves gas sensing at low-working temperatures. Likewise, nanosheets/nanofilms (2D structures) with large porosity shows better response and gas sensitivity as well as better response-recovery characteristics. Nanostructured films owing to their larger specific surface area, will have more active sites on them, which can effectivity improves sensor response [303]. Apart from that, a porous structure/higher porosity are favorable conditions that can create more diffusion channels.

The macro/mesoporous ZnO films prepared via PBM alter the gas response and operating temperature. Based on our results, we observed that increased porosity on ZnO film shows larger sensor response, which is due to increase in gas diffusion on sensing layer and once again will assist in lowering gas sensor working temperatures.

Liang et al. group [304] (***Figure 4. 7***) investigated the effect of gas sensing performance based on grain size and surface roughness. They studied SnO_2 doped film with various concentrations of Ce metallic in an Ar/O_2 mixed atmosphere. Their results show an increase in surface roughness with an increase in doping concentration. Also, an increase in surface roughness showed increase in grain size of nanoparticles. Similarly, their surface analysis shows the closely packed smaller grain sizes without voids or cracks without any visible pores. However, for an increased doped SnO_2 film, the surface grain of thin films gets coarser along with visible and broad grain boundaries. The rough surface is beneficial to increase the interaction degree between the material and target gas molecules and improves the gas sensing performance [281]. Also, narrowly distributed agglomerates of different-sized particles exhibit better sensing performance, where the smaller the agglomerate size, the better the response [305]. This might explain why the 800 rpm PBM ground nanoink sensor shows a better response than the 1000 rpm sensor, even though the sensor prepared from 1000 rpm has better porosity than the 800 rpm.

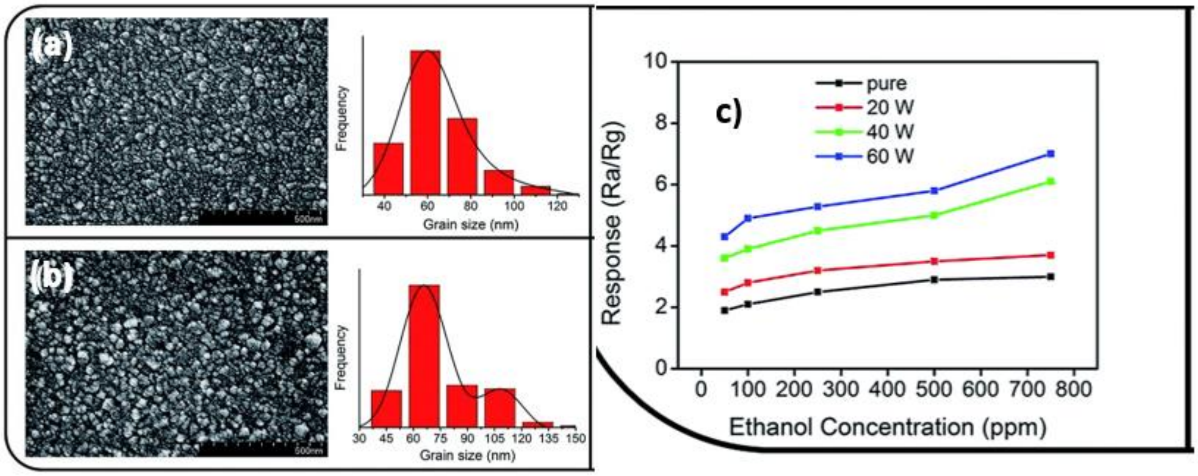

Figure 4. 7. SEM images showing Ce-doped SnO2 thin films (a) 0 W (b) 40 W.(c) Gas sensing response values vs. ethanol vapor concentrations for various Ce-doped SnO_2 films. (Adapted from [304]).

Although particles tend to agglomerate to form larger entities, voids might still be present. In order words, porosity in the sensing layer may be bimodal: each agglomerate may have small pores (micropores), while adjacent agglomerate gets separated by larger pores [306]. The gas diffusion gets slower in smaller pores based on Knudsen diffusion (shown in equation 11). The diffusivity coefficient (D_k) is proportional to pore radius 'r' molecular weight 'M' and absolute temperature 'T'. R in the equation represents the universal gas constant.

$$D_K = \frac{4r}{3}\sqrt{\frac{2RT}{\pi M}} \qquad (11)$$

We assume that the particle starts to agglomerate after 400 rpm and 30 min grinding time based on mesopores and micropores. The smaller pores begin to dominate at 600 rpm, and the gas response sensor decreases, which will also cause an increase in response time since target gas might take longer to diffuse inside all tiny pores. Similarly, after removing the target gas, it will take longer for test gas to vacate from the pores, thus increasing recovery time. For higher trials

(> 600 rpm), we believe that mesopores get dominant and will cause quicker gas response. Also, the response time gets faster because of mesopores due to less diffusion path and diffusion areas. Due to grain cluster formation, micropores of higher grinding trials might get covered by agglomeration, where gas diffusion only occurs from larger mesopores.

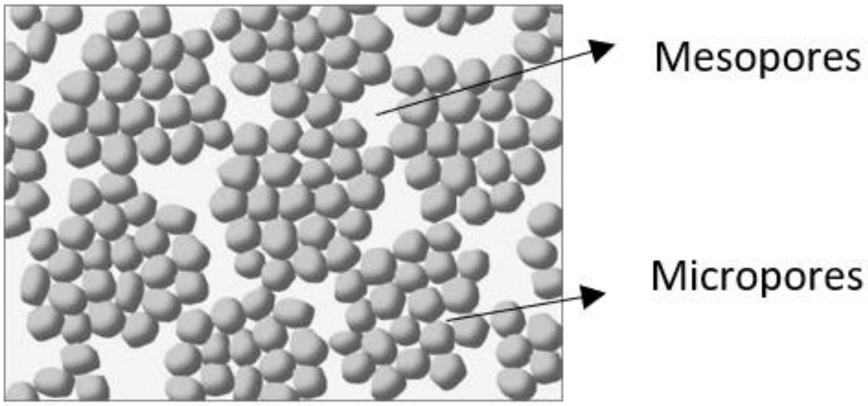

Figure 4. 8. The schematic draw of primary grains united into larger entities. The different pores show the route for diffusivity of gas molecules.

Sensing mechanism

Since ZnO is a chemoresistive sensing material [153], the sensor response mechanism is influenced by the gas-surface adsorption-desorption process, surface diffusion-reaction and redox reactions between active species on the sensor surfaces [145]. In addition, defects of nanostructured ZnO such as oxygen vacancies (See Raman data, ***Figure 4.2***) can act as electron donors, which enhances conductivity and promotes gas sensing performance [168,294]. Grinding in the presence of solvents during PBM can also result in surface modification [307], since ball milling is an energy intensive process. The energy from the high speed impact of the beads can results in the formation of reactive radicals [307]. The grinding media, therefore, can influence the baseline resistivity of the ZnO nanostructured films [153,308,309].

The sensing mechanisms in our fabricated sensors likely depend on surface interaction and charge transfer between adsorbed gas species, which results in variation of sensor resistance (or conductance) [310]; it is reported that O_2^- species will be present at ZnO film surfaces at room temperature [311,312], which results in an electron-depletion layer (barrier layer) on the outer surface of the ZnO in air. Between grains the merging of the two depletion regions creates a Schottky barrier, the magnitude of which determines the conductivity of the materials [154]. The reaction between the adsorbed oxygen species with adsorbed gas molecules can modify the height of the Schottky barrier resulting in the variation of sensor resistivity; in the dark, when the ZnO surface is exposed to an air environment, electrons from the ZnO conduction band ionize atmospheric oxygen to produce negative oxygen ions at the surface of nanostructured film (equation.(12)), thereby creating a low conductivity depletion layer near the surface [313].

$$O_2(gas) + e^- \rightarrow O_2^-(ads), \qquad (12)$$

On the other hand, when light with higher energy than the bandgap of ZnO is incident, electron-hole pairs will be generated. Holes produced by the light absorption migrate to the surface along the potential slope created by band bending and neutralize the negatively charged adsorbed oxygen ions (equation.(13)), which are then desorbed, while the photogenerated electrons reduce the width of the depletion layer, thereby increasing conductivity [313].

$$h^+ + O_2^- \rightarrow O_2\ (gas), \qquad (13)$$

Thus, conduction in dark and photoconduction of the ZnO films are strongly dependent on the ambient gas conditions and oxidizing atmosphere. In addition, RH, defined as the amount of water vapor in air, expressed as a percentage of the maximum amount that the air could hold at a given temperature, can also strongly impact a metal oxide surface [314] and thus alter the sensor response [315–317]. Water molecules adsorbed on the surface tend to dope ZnO with electrons and/or displace previously adsorbed ionized oxygen, releasing electrons back to the conduction band (i.e., the reverse of equation. (12)) [316].In both cases, sensor conductivity increases as consistent with ***Figure 4. 3 (b).***

For the ZnO thin film gas sensors based on PBM nanoink reported here the ultimate performance likely depends on a combination of grain size, porosity and surface-to-bulk defect ratio within the films. The results from porosity (***Figure 4.6***), indicate that there is high surface area in sensors based on PBM nanoinks, peaking around a grinding speed of 400 rpm and grinding time of 30 minutes, which ultimately creates more active sites and gas diffusion channels and hence improves sensing signal magnitude. To probe the gas sensor performance further, we examined the effect of operating temperature on sensor response; thermally activated processes can impact reaction kinetics, carrier concentration and mobility on/near the sensing surface, all of which affect gas sensor detection response and dynamic behavior [318]. ***Figure 4.9(a)*** shows temperature-dependent sensor response data indicating optimal operation near 100 ^{0}C, followed by a decline at higher temperatures, consistent with prior work using metal oxides [159]. Similarly, a shortening of response and recovery times (***Figure 4.9 (b)***) at elevated temperatures is due to large number of gas molecules can overcome the activation energy required for surface reactions, i.e., faster adsorption and desorption occurs on the surface of the ZnO leading to shorter response/recovery time [170]. The increase in temperature increases the kinetic energy of gas molecules, which helps in faster gas diffusion and ejected from diffusive channels, this in turn shows faster response and recovery time. ***Table 1*** summarizes data for ZnO gas sensors fabricated using various synthesis techniques, including ball milling, and their response to different gas species.

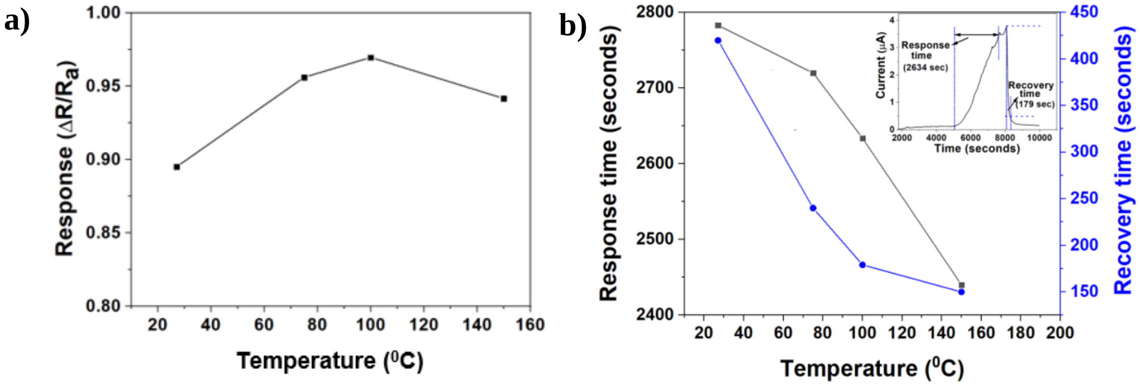

Figure 4.9. Effect of temperature on sensor response. (a) Response for sensors prepared from ZnO nanoinks ground at 600 rpm for 10 minutes using EG solvent. (b) Response and recovery time. The inset shows the time dependence of sensor current upon exposure to dry air followed by argon test gas at 100 ^{0}C.

The gas sensors vary their response depending upon the testing gas and operation temperature due to the adsorption-desorption kinetics. Also, metal oxide gas sensor response depends on stoichiometry, carrier concentration, mobility, and partial oxygen pressure at a specific measuring temperature. Some authors claim that the sensor is coated by the residual compounds from the combustion of the testing gas, resulting in saturation or decreased sensitivity [319]

Table 1. Brief summary of gas sensor response for ZnO-based devices operating at different temperatures.

Material	Target gas	LOD	Response /Temperature	Response time/ Recovery time	Ref
Present work	H_2 (5000 ppm)	500 ppm	21%^{b}/ RT	-	-
CuO coated ZnO using ball milling method	H_2 (200 ppm)	-	~15^{a}/ 300 ^{0}C	-	[320]
ZnO nanotube using chemical etching process	H_2 (500 ppm)	5 ppm	~29.6%^{b}/ RT	~540 s/-	[321]
SnO_2 doped ZnO using ball milling method	CO (200 ppm)	-	~5^{a}/ 450 ^{0}C	-	[152]
ZnO- CuO composite via ball milling process	CO (200 ppm)	-	~12.2^{a}/ 180 ^{0}C	-	[322]
Pt-doped ZnO using RF sputtering	H_2 (1000 ppm)	250 ppm	~5.5^{a}/ 200 ^{0}C	36 s/112 s	[323]
ZnO nanowires by thermal evaporation	H_2 (100 ppm)	50 ppm	~5.5^{a}/ 200 ^{0}C	30 s/-	[324]

$^{a)}S = R_a/R_g = I_g/I_a$; $^{b)}S = (R_a-R_g)/R_a*100\%$

Limitations of current set up

There are few parameters, such as chamber size, high flow rate and film thickness that need to be taken into consideration for the current set up. The target gas response of our sensors was repeatable over multiple flow sequences, however due to the size of the test quartz chamber and maximum flow rates used (in addition to the film thickness) it took some time to reach a stable baseline. Response/recovery time evaluation and LOD is also constrained by gas flow rates (maximum 500-700 sccm), test chamber volume, and gas sensor film thickness used in the present study. In a larger chamber, drift in a baseline resistance and lower response to gas concentration can also be observed [325,326]. Additionally, the film thickness will also affect the sensor response and response/recovery time. The influence of film thickness on the sensor characteristic is mainly explained on the basis of transport phenomena i.e., modeling of the diffusion/penetration of the target gas molecules into the pores of the sensing film, while reacting with adsorbed oxygen on the way (diffusion theory). Thus, thicker films as used in our studies will take much longer to reach their saturation point of sensor response.

4.4. Conclusion

In summary, we showed resistive ZnO thin film gas sensors fabricated using PBM nanoinks and doctor blading operate efficiently under ambient conditions at room temperature. The sensors are effective towards detection of various gas species (oxygen/dry, argon, nitrogen, hydrogen and methane) and atmospheric humidity. Different nanostructured films (with varied sizes and porosity) prepared at various grinding parameters could also be optimized for efficient gas sensing. The results show that sensor's response at different milling speed (400 rpm) and time (30 min) delivered the best combination of sensor signal magnitude and dynamic behavior (time response). Also, the performance was further enhanced when operating temperatures was set up to 100 ^{0}C.

Chapter 5

5. Conclusion and Future work

The preliminary water splitting preliminary experiment were conducted by R. Sapkota and Jinxiang Zou (MITACS Globalink program). For dye degradation experiment, R. Sapkota and Xue Cai [102] *(MEng graduate student) worked together. For photoconductive sensor, most drop casted film were prepared and analyzed by Sahil Dawka* [101] *(MEng graduate student) and later more nanostructured films (both doctor blading and drop casted films) were prepared and investigated by the author. Pengjun Duan* [103] *(MEng graduate student) and Tanay Kumar (MITACS Globalink program) worked together in preparing ZnO nanostructured films using doctor blading technique for UV sensing. The author worked on preparing colloidal suspension of* $TiSi_2$*, Silicon and ZnO that were used in this section. Parts of the results in this chapter were published in [C1].*

5.1. Summary

This work presents the systematic investigation of the planetary ball milling technique for creating various multifunctional nanostructured films. Several parameters (speed, grinding time and solvent) related to the planetary ball mill have created the resultant particles' tunable properties.

The first chapter summarizes the background information about the evolution of nano/microdevices. Further, this chapter presents the motivation behind doing the research. Similarly, the following chapter presents the nanogrinding technique for preparing colloidal suspension. Additionally, different fabrication steps for creating nanostructures/ nanoparticles/film were also presented. For the wettability applications, we had fabricated multifunctional thin film using silicon and $TiSi_2$. Solution coated from resultant suspensions were able to produce stable and uniform thin films on various surfaces (planer and non-planar), including rigid (glass, SiO_2/Si, Si) and flexible (paper, AAO and fabric) substrates. Microscopy, contact angle and electrical conduction measurements showed that produced nanoparticle coatings from solution had tunable properties. For silicon thin film, CA tends to increase with increased grinding time. However, $TiSi_2$ thin film showed a smaller contact angle at higher grinding time/speed. Furthermore, the variation in conductivity of ground film also exhibits a few orders of magnitude variation. As we know, surface chemistry and solvent had altered the thin film properties; we had further explored our research through an annealing experiment to remove the functional groups from nanostructured films coated on rigid substrates. The results showed the reduction of contact angle on both silicon and $TiSi_2$ film at different annealing conditions. Also, the films' conductivity improved at higher annealing time, which might have happened due to improved surface chemistry and/or grain boundaries. We had further investigated the wettability properties of nanostructured thin films prepared from various purity grades of silicon. We observed that the wettability results on non-annealed thin film from both types of powder showed an increasing contact angle trend on glass substrate at increasing grinding time. Results also show that the contact angle on both types of the film was reduced after annealing.

Similarly, $TiSi_2$ and Silicon colloidal suspension coated on flexible substrates were analyzed based on their wettability and conductivity properties. Similar wettability trend was observed on both flexible and rigid substrates. However, the *I-V* characterization of EG ground $TiSi_2$ film (800 rpm for 10 minutes) on flexible film showed a lower current than the rigid substrates. However, increasing volume of suspension revealed increased current on porous/flexible film. Interestingly, we observed that the electrical current didn't change much when the substrate was bent/folded.

Planetary ball milling is considered a low-cost top-down approach, and knowing this fact, we further use this technique for fabricating a colloidal suspension of ZnO. The fabricated ZnO was prepared in a thin film structure and were examined the gas sensing behavior (explained in Chapter 4) at room temperature. The chemiresistive sensor fabricated using PBM nanoinks and doctor blading shows effective detection of various gas species such as nitrogen, dry air/oxygen, argon, hydrogen, methane, in addition to atmospheric humidity. By varying grinding parameters, nanoparticle structure and electrical characteristics of the resultant films could be optimized for efficient gas sensing. The response of different fabricated gas sensors versus milling speed and time revealed that nanostructured films made using ZnO nanoinks milled at 400 rpm and 30 minutes produced the best combination of sensor signal magnitude and dynamic behavior (time response), and further performance enhancement was observed up to temperatures of 100 ^{0}C. Also, spectroscopy analysis (Raman, PL and X-ray) indicates the purity of ground materials.

Along with wettability, electrical conductivity and gas sensitivity examined here, the nanogrinding technique can produce coatings with optical, mechanical, photovoltaic, flexibility, etc., functionality—the large parameter space afforded by this approach can thus allow multifunctional thin films with desired properties to be created for various applications including surface coatings, electronics, photonics, photocatalysis and energy production/storage.

5.2. Future work

5.2.1. Preliminary experimental work

In our research, we did some preliminary experiments on dye degradation, water splitting, and photoconductivity test, and these experiments could be carried out for future work. The brief computational analysis was also performed. We mainly use $TiSi_2$ and Si trials for water splitting experiment, and for photoconductive sensor and photocatalytic activity, we use ZnO samples. Brief explanation and result of our preliminary work are as follows:

Water splitting

Photocatalytic water splitting using suspended nanoparticles has been possible, and many new materials were tested. In case of photocatalytic water splitting, a catalyst (nanopowder) absorbs photon energy, and consequently, an electron is transferred from its valance to the conduction band. To occur splitting, the bandgap of nanopowder must be greater than 1.23 eV (minimum energy required by an electron) and its band edges meet the thermodynamic requirement for the charge transfer to occur, then in principle, excited electrons can reduce hydrogen ions, and holes can oxidize oxygen anions [327,328].

We performed our photocatalytic water splitting experiment using the nanofilms of $TiSi_2$ and Si. The apparatus used in our test consists of a halogen lamp, flask, DI water, hot plate and nanofilms. The nanofilms were created by coating $TiSi_2$ or Si ground suspension on glass and/or AAO substrates. During the experiment, nanofilms were suspended on DI water, and the halogen lamp was irradiated, and the temperature was maintained at 70^0 C. The degassing process was carried out using nitrogen gas for 1-2 minutes. A handheld flammable gas detector was used for detecting the gas generated inside the flask. The bubble formation on the surface of nanofilms (shown in ***Figure 5. 1.(b)***) after light exposure indicates the evolution of gas. The analysis for detecting the type of gas needs further investigation because photocatalyst not only highly dependent on the type of photocatalysts but also dependent on test conditions (reaction temperature and light intensity) [327,328].

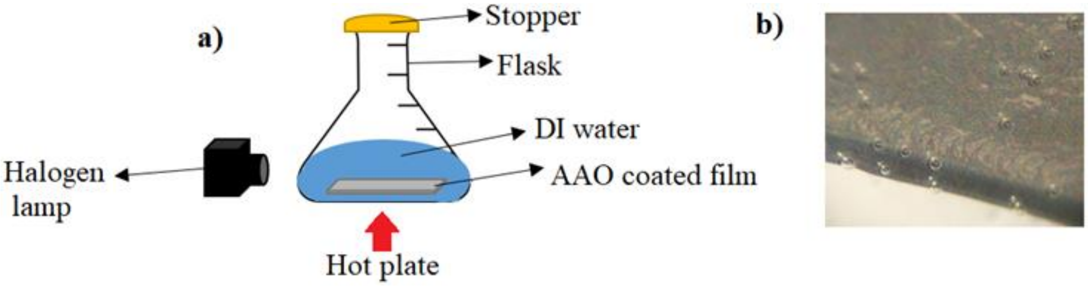

Figure 5. 1. (a) Experiment set up for photocatalysis (b) $TiSi_2$ coating upon exposure to halogen lamp.

Dye degradation [102]

Another groundwork performed in this research was related to dye degradation. The basic dye degradation mechanism undergoes three different processes: electron-hole pair generation, oxidization of hydroxyl group and water molecules, and diffusion of pollutants. When the light gets irradiated on a nanopowder surface, it will absorb photons with energy of same or higher than its bandgap. The absorbed photon helps the electrons in the valance band to become excited and jump from the forbidden zone to the conduction band. At this period, the strong oxidizing hole (h^+) on the valance band oxidizes the hydroxyl group and water molecules on the surface of nanomaterials into OH* radicals [284]. This free radical acts as a strong oxidant that diffuses the pollutants and oxidizes the organic contaminants into water, carbon dioxide or other harmless substances. It is assumed that the dye degradation mechanism depends on various parameters (surface area, particle size, morphology and defects)[73,284,329]. From the milled powder results (based on Chapter 4), we have seen that milling cause alteration on nanoparticles' particle size and defects, and these factors would likely affect the nanopowder's photocatalytic ability.

We have used the different ground powders of nanoparticles for our dye degradation experiments [102]. Initially, 3 ml of suspension (before extraction, the slurry was sonicated to make homogenous colloidal suspension) were extracted from the sonicated vials, poured into epitubes and centrifuged. The clear separation between solvent and nanomaterials was visible after appropriate centrifuged condition (10000/20000 rpm for 10/20 minutes). Later, supernatant was removed, and DI water was added into epitubes and re-sonicated for another 20 minutes (the process is repeated three times). The nanoparticles present inside the epitubes were then dried for more than 6 hours in the mechanical oven at 80 ^{0}C. The dried powders from epitubes were removed, poured on a watch glass, and further dried for 2 hours. The prepared powders were then stored inside a glass vial and were used during the Methylene blue (MB) dye degradation experiment. The main apparatus for this experiment was halogen lamp, a plano-convex lens, 8-dram vial, catalyst, stirrer bar and hot plate. The distance between the dye solutions to the halogen lamp was fixed at 10 cm. The dyes degradation result is shown in ***Figure 5. 2 (b)***.

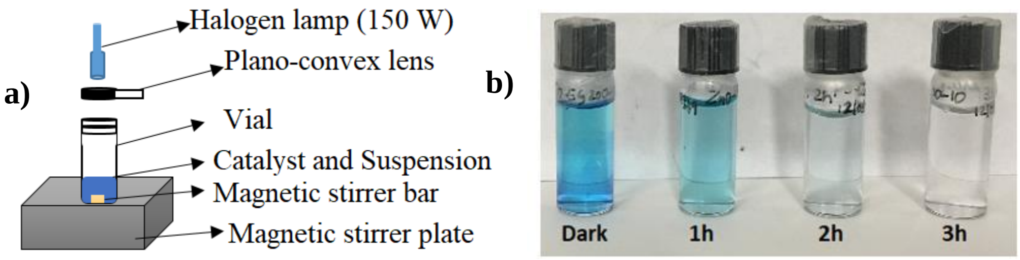

Figure 5. 2. (a) Set up for dye degradation experiment (b) MB Dye degradation behavior of ground ZnO powder (bulk powder ground at 200 rpm for 10 minutes in EG solvent).

For all dye degradation experiments, 7 ppm of dye solution, 10 mg of catalyst powder and a stirring speed of 300 rpm (for homogeneous mixing of catalyst in dye solution) were kept constant, and the experiment was performed in an ambient environment. To achieve the adsorption equilibrium, the suspension was first sonicated at power level 5 for 5 minutes and then placed in a magnetic stirrer plate at a speed of 300 rpm in a dark environment for 1 hour. The dram was also wrapped with aluminum foil to prevent the light from entering inside the vial. After an hour of dark reaction, the sample (1.5 ml) was extracted and centrifuged at 10000 rpm for 10-15 minutes to separate the catalyst and dye solution. The clear supernatant was removed from the epitubes and collected in 0.5-dram vials. A similar process was repeated for light reaction, and the supernatant was extracted. The experiment was run for 4 hours in total. We have extracted following results from preliminary dye degradation experiment.

Photoconductive sensor [101]

The other preliminary test we did was fabricating ZnO photoconductive sensor. The process of photoconduction occurs when semiconductor materials absorb a photon (from electromagnetic radiation) with energy higher than its bandgap then electron-hole pairs are generated. As the light with the appropriate wavelength gets incident on the material's surface, it increases conductance. In the absence of light, generated charge carrier recombines rapidly, which results in sharp decay in conductance. The presence of atmospheric oxygen has explained the prolonged decay process in an n-type semiconductor such as TiO_2 and ZnO. The photoconductivity mechanism is described in chapter 4 [313].

In our experiment, we prepared a thin film sensor by doctor blading/drop casting of the ZnO ground suspension as shown in ***Figure 5.3.a.*** The thin film was quickly dried on the hot plate under ambient atmosphere. After drying, a colloidal suspension of Ag was painted on either side of the film to create contact regions. The sample was further dried in an oven for an extra hour to remove solvent from Ag suspension. The photoconduction properties of drop casted/doctor bladed ZnO sensor were investigated using the sweep voltage of ± 5 V with a step size of 0.1 V, whereas doctor bladed samples of ZnO (both annealed and non-annealed) were prepared, and only a few are examined. The photoconductive sensor measurement setup is shown in ***Figure 5.3 b*** and the photoconductive response is shown in ***Figure 5.3 c .*** Exposure of light on samples is controlled by using a chopper.

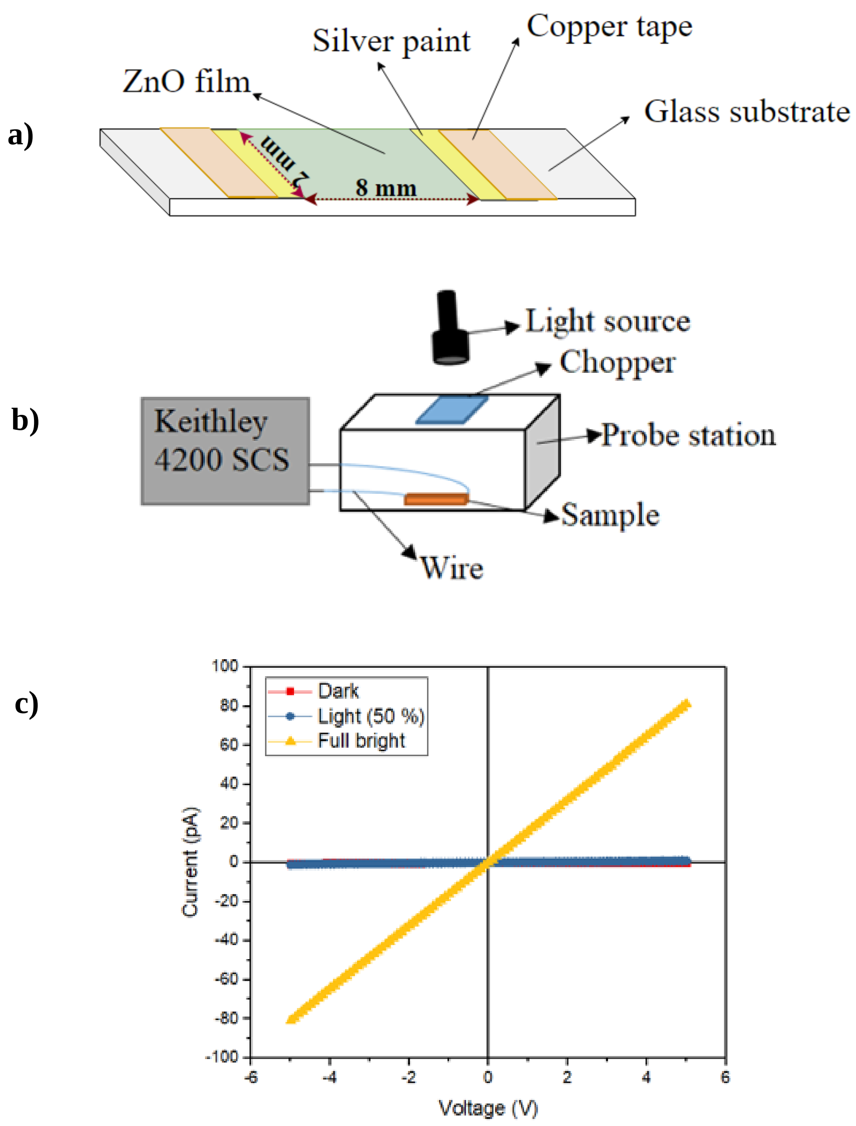

Figure 5.3. Fabricated nanostructure ZnO photoconductive sensor (b) Schematic diagram of photoconductive sensor set up in the lab (c) Photoresponse of drop casted ZnO ground film (prepared at 200 rpm for 10 minutes using EG solvent) on the glass substrate.

Computational simulations

The computational modelling of various material structures and their properties is very useful and valuable in building materials and their application. The research work performed in

Chapter 4 could be further extended by studying the different properties of ZnO using the first-principle calculation based on density-functional theory (DFT). DFT is considered a preferred computational method due to software simplicity and its ability to calculate the ground state properties with predictive accuracy.

For our preliminary work, we did computational studies on the adsorption of oxygen atoms on the two different sites of Zn-terminated (001) surface wurtzite ZnO structure. All calculations were performed by the Cambridge Serial Total Energy Package (CASTEP) module of the Materials Studio software based on the first principle DFT code using on-the-fly generated ultrasoft pseudopotentials (OTFG).

Our optimized bulk ZnO under the above setting shows a lattice constant of a =3.249 Å and c =5.205 Å, c/a ratio of 1.602 and internal parameter (u) as 0.3798. The data has good agreement with the experimental values [330]. Examples of species adsorption on ZnO surfaces is shown in ***Figure 5. 4***.

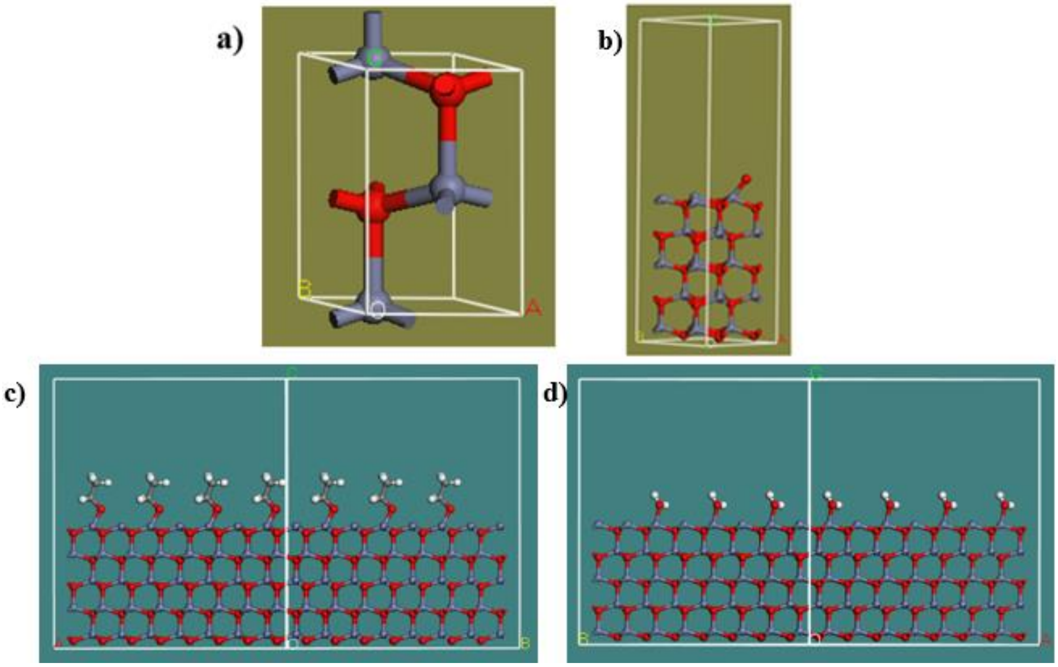

Figure 5. 4. (a) Bulk ZnO crystal structure. Adsorption of species on (001) surface of ZnO supercell (b) oxygen atom. (b) ethanol molecules (c) water molecules. The red, white, light gray and dark gray atoms represent oxygen, hydrogen, zinc and oxygen atoms respectively.

5.2.2. Future applications

The application of the nanogrinding technique continues to gain research interest in preparing multiple nanostructured materials due to its low cost, applicability to various scale industries and capability to grind a variety of nanomaterials. However, different grinding parameters must be optimized for specific type of applications. Integrating grinding parameters and solvents can produce novel nanomaterials that can effectively be utilized in various applications such as gas sensors, solar energy, fuel cells, water splitting, energy storage devices, catalysts, and many more, as some of our preliminary experiments have already shown. Other applications that can be extended from the current research are as follows:

i. Anode materials for Lithium batteries

Silicon-based anodes materials for lithium-ion batteries (LIBs) are among the most promising candidates over conventional anodes used in commercial LIBs. The practical application of silicon is limited due to its volume expansion upon cycling. On the other hand, porous silicon electrodes exhibit excellent electrochemical performances in high electron density LIBs. The mesoporous Si and Si-composite prepared from mechanical milling have shown high reversibility capacity, excellent electrochemical and rate performances and long-term stability. The mesostructured prepared from Si/C composite can effectively control the volume change of Si and prevent unwanted mechanical stress and pulverization during cycling process [331].

From our research, the PBM technique shows that it can produce a porous nanostructure/nanocomposite that could be useful for battery/fuel cell (shown in ***Figure 5.5***). One can move research forward to create anode/cathode material and could study the various grinding parameters that could give efficient performances (high specific capacity).

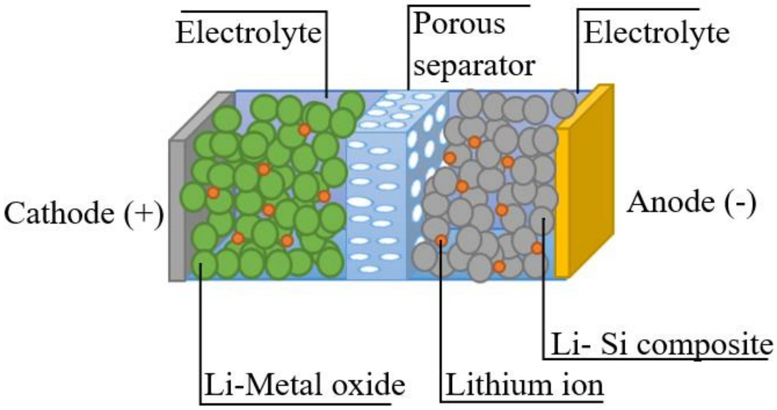

Figure 5.5. Schematic diagram of Lithium-ion battery.

ii. Other applications (anticorrosion, self-cleaning and wear resistance)

In this thesis, some preliminarily work regarding wettability (as explained in **chapter 3)** can be further investigated and analyzed from the prepared ground thin film on other various substrates. Coating the ground suspensions onto different rigid substrates such as metals, woods, polymers, tiles etc., prevents materials from corrosions, fire, fouling and wear resistance. Several nanomaterials/nanocomposites suspension can be coated directly onto these substrates. The adhesion/stability of the ground film on those substrates can be studied. Simultaneously, other applications such as antifouling, water resistance and self-cleaning properties can also be investigated. For example, Zinc oxide nanostructured coating acts as an effective shielding to fouling [269]. Its nanocomposite coatings have anti-corrosion and superhydrophobic properties [332], which can be implemented over a larger scale. Large scale industries (example: transportation, chemical plants, oil refineries, public utility works, pulp and paper mills and marine) uses metals and alloys, and these sectors are often at the risk of corrosion, which can cause economic loss. Therefore, nanocoating revives partially or completely repair/replacement cost and increases the durability of metal surfaces.

The ball milling technology has been studied in process engineering, organic synthesis and nanocomposites formation. However, its potential research in nanostructured thin film fabrication has not been fully explored, as only a limited number of studies have been carried out. Further studies on grinding mixtures of nanoparticles at different grinding parameters, along with surfactants, provide a new route for preparing suspension with no or reduced agglomeration. Similarly, the effect of solvent, bead size, ball to powder ratio and material type can be varied and studied sequentially for various applications. Fourier Transform infrared spectroscopy (FTIR spectroscopy) is an analytical technique which could be used for analyzing the surface composition on the nanoparticle’s surface. This technique has been very effective in identifying the functional group that are attached on the surface of the nanoparticles. Likewise, XPS (X-ray photoelectron spectroscopy) can provide information about elemental composition. The surface chemistry of the nanostructured thin film can study using this technique. Both these techniques will help in determining the functional groups present on colloidal nanoparticle’s surface. The characterization of those obtained nanomaterials provides researchers with new directions for studying their properties and applications.

Different morphological nanostructures show diverse gas diffusion capabilities and responses. For example, one dimensional structures (nanorods, nanotubes) with higher surface to volume ratio are able to operate at lower temperature and shows improved gas sensitivity. On the other hand, 2D nanomaterials (nanoplates, nanofilms) owing to their large specific surface area, create more active sites on the surface and thus improve sensor performance [75,302]. Finding a suitable way for controlling the grain sizes using PBM can result in various shapes of nanostructures which could increase effective ratio surface area, defect density and porosity, which ultimately provides more active sites for gas reactions and detection.

In conclusion, nanoscale grinding technology based on planetary ball milling is a promising synthesis process for preparing nanoinks and nanoparticle films. Many applications of the resulting thin films and nanoparticles can be further researched and implemented in small and/or large-scale industries.

References

1. Thrower, K. The Fleming thermionic diode and the birth of electronics. *Transactions of the Newcomen Society*. **2005**, 75, 229–259.
2. Dylla, H.F; Cornelissen, S.T. John Ambrose Fleming, and the beginning of electronics. *J. Vac. Sci. Technol A: Vac. Surf. and films*. **2005**, 23, 1244–1251.
3. Noyce, R.N. *Microelectronics. Sci. Amer*. **1977,** 237, 62–69.
4. Brinkman, W.F.; Haggan, D.E.; Troutman, W.W. A history of the invention of the transistor and where it will lead us. *IEEE J. Solid-State Circuits*. **1997**, 32, 1858–1865.
5. Moore, G. Moore's law. *Electronics Magazine*. **1965**, 38, 114.
6. Zhang, L. Silicon Process and Manufacturing Technology Evolution: An overview of advancements in chip making. *IEEE Consum. Electron. Mag*. **2014**, 3, 44–48.
7. Abuelma'atti, M.T. MOSFET Scaling Crisis and the Evolution of Nanoelectronic Devices: The Need Paradigm Shift in Electronics Engineering Education. *Procedia-Social and Behavioral Sciences*. **2013**, 102, 432–437.
8. Itoh, K.; Sugii, N.; Hisamoto, D.; Tsuchiya, R. FD-SOI MOSFETs for the low-voltage nanoscale CMOS era. in Proceedings of the 2009 I*EEE International SOI Conference*. **2009**, pp. 1–4.
9. Pouyan, P. Reliability-aware memory design using advanced reconfiguration mechanisms, Universitat Politecnica de Catalunya, **2015**.
10. Haselman, M.; Hauck, S. The Future of Integrated Circuits: *A Survey of Nanoelectronics. Proc. IEEE*. **2010**, 98, 11–38.
11. Lu, W.; Lieber, C.M. Nanoelectronics from the bottom up. in Nanoscience and Technology. **2010**, pp. 137–146.
12. Kim, Y.-B. Challenges for nanoscale MOSFETs and emerging nanoelectronics. Trans. *Electr. Electron. Mater*. **2010**, 11, 93–105.
13. Dongale, T.; Magdum, S.; Goilkar, K.; Chougule, N.; Ghatage, S. Shifting towards nanoelectronics: A device level overview. *J. Acad. Indus. Res*. Vol. 1 (8) **2013**.
14. Radamson, H.H.; He, X.; Zhang, Q.; Liu, J.; Cui, H.; Xiang, J.; Kong, Z.; Xiong, W.; Li, J.; Gao, J.; et al. Miniaturization of CMOS. *Micromachines*. **2019**, 10, 293.
15. Kavalieros, J.; Doyle, B.; Datta, S.; Dewey, G.; Doczy, M.; Jin, B.; Lionberger, D.; Metz, M.; Rachmady, W.; Radosavljevic, M.; et al. Tri-Gate Transistor Architecture with High-k Gate Dielectrics, Metal Gates and Strain Engineering. *In Proceedings of the Symposium on VLSI Technology*, Digest of Technical Papers. **2006**, pp. 50–51.
16. Colinge, J.-P.; others FinFETs other multi-gate transistors; Springer, **2008**; Vol. 73;
17. Natarajan, S.; Agostinelli, M.; Akbar, S.; Bost, M.; Bowonder, A.; Chikarmane, V.; Chouksey, S.; Dasgupta, A.; Fischer, K.; Fu, Q.; et al. A 14nm logic technology featuring 2nd-generation FinFET, air-gapped interconnects, self-aligned double patterning and a 0.0588 µm2 SRAM cell size. *In Proceedings of the 2014 IEEE International Electron Devices Meeting*. **2014,** pp. 3.7.1–3.7.3.

18. Xu, M.; Zhu, H.; Zhao, L.; Yin, H.; Zhong, J.; Li, J.; Zhao, C.; Chen, D.; Ye, T. Improved short channel effect control in bulk FinFETs with vertical implantation to form self-aligned halo and punch-through stop pocket. *IEEE Electron Device Lett.* **2015**, 36, 648–650.
19. Bohr, M.; Mistry, K. Intel's revolutionary 22 nm transistor technology, Intel website 2011.
20. Roy, T.; Tosun, M.; Kang, J.S.; Sachid, A.B.; Desai, S.B.; Hettick, M.; Hu, C.C.; Javey, A. Field-effect transistors built from all two-dimensional material components. *ACS Nano*. **2014**, 8, 6259–6264.
21. Chelliah, C.R.J.; Swaminathan, R. Current trends in changing the channel in MOSFETs by III–V semiconducting nanostructures. *Nanotechnol. Rev*. **2017**, 6, 613–623.
22. Feynman, R. There's plenty of room at the bottom: an invitation to enter a new field of physics. *Engineering & Science Magazine*. **1960**.
23. Eigler, D.M.; Schweizer, E.K. Positioning single atoms with a scanning tunnelling microscope. *Nature* **1990**, *344*, 524–526.
24. El-Shall, M.; Edelstein, A.; Cammarata, R. Nanomaterials: synthesis, properties and applications. *Institute of Physics Publishing, Bristol and Philadelphia, PA* **1996**, 13–54.
25. Visakh, P.; Morlanes, M.J.M. Nanomaterials and Nanocomposites: Zero-to Three-Dimensional Materials and Their Composites, *John Wiley & Sons.* **2016.**
26. González, A.; Noguez, C. Influence of morphology on the optical properties of metal nanoparticles, *J. Comput. Theor. Nanosci.* **2007**, *4*, 231–238.
27. Wang, Z.; Daemen, L.L.; Zhao, Y.; Zha, C.; Downs, R.T.; Wang, X.; Wang, Z.L.; Hemley, R.J. Morphology-tuned wurtzite-type ZnS nanobelts. *Nat. Mater.* **2005**, *4*, 922–927.
28. Eustis, S.; El-Sayed, M.A. hy gold nanoparticles are more precious than pretty gold: noble metal surface plasmon resonance and its enhancement of the radiative and nonradiative properties of nanocrystals of different shapes. *Chem. Soc. Rev.* **2006**, *35*, 209–217.
29. Pokropivny, V.; Lohmus, R.; Hussainova, I.; Pokropivny, A.; Vlassov, S. *Introduction to nanomaterials Nanotechnology*; Tartu University Press Ukraine, **2007**.
30. Becheri, A.; Dürr, M.; Nostro, P.L.; Baglioni, P. S Synthesis and characterization of zinc oxide nanoparticles: application to textiles as UV-absorbers. *J. Nanopart. Res.* **2008**, *10*, 679–689.
31. Zhang, W.; Wang, P.; Fei, X.; Xiu, Y.; Jia, G. Growth mechanism and morphologies tuning of ZnO nanostructures,. *Int. J. Electrochem. Sci* **2015**, *10*, 4688–4695.
32. Viswanathan, B. Nanomaterials, Alpha Science, Oxford, UK, **2009**.
33. Hong, R.; Li, J.; Chen, L.; Liu, D.; Li, H.; Zheng, Y.; Ding, J. Synthesis, surface modification and photocatalytic property of ZnO nanoparticles,. *Powder Technol.* **2009**, *189*, 426–432.
34. A, Alagarasi Chapter - Introduction to Nanomaterials; **2011**; p. 76.
35. Liu, L.; Mei, Z.; Tang, A.; Azarov, A.; Kuznetsov, A.; Xue, Q.-K.; Du, X. Oxygen vacancies: The origin of n-type conductivity in ZnO. *Phys. Rev. B.* **2016**, *93*, 235305.

36. Cuadra, J.G.; Porcar, S.; Fraga, D.; Stoyanova-Lyubenova, T.; Carda, J.B. Enhanced Electrical Properties of Alkali-Doped ZnO Thin Films with ChemicalProcess. *In Solar*; Multidisciplinary Digital Publishing Institute**, 2021**; Vol. 1, pp. 30–40.
37. Sundaram, R.M.; Koziol, K.K.; Windle, A.H. Continuous direct spinning of fibers of single-walled carbon nanotubes with metallic chirality. *Adv. Mater.* **2011**, *23*, 5064–5068.
38. He, H.; Pham-Huy, L.A.; Dramou, P.; Xiao, D.; Zuo, P.; Pham-Huy, C. Carbon nanotubes: applications in pharmacy and medicine. *Biomed Res. Int.* **2013**, *2013*.
39. Dagher, S.; Soliman, A.; Ziout, A.; Tit, N.; Hilal-Alnaqbi, A.; Khashan, S.; Alnaimat, F.; Qudeiri, J.A. Photocatalytic removal of methylene blue using titania-and silica-coated magnetic nanoparticles. *Mater. Res. Express* **2018**, *5*, 065518.
40. Batsaikhan, E.; Chen, Y.-C.; Lee, C.-H.; Li, H.-C.; Li, W.-H. Development of ferromagnetic superspins in bare Cu nanoparticles by electronic charge redistribution. *Int. J. Mol. Sci.* **2015**, *16*, 23165–23176.
41. Leslie-Pelecky, D.L.; Rieke, R.D. Magnetic properties of nanostructured materials. *Chem. Mater.* **1996**, *8*, 1770–1783.
42. Biswas, A.; Bayer, I.S.; Biris, A.S.; Wang, T.; Dervishi, E.; Faupel, F. Advances in top–down and bottom–up surface nanofabrication: Techniques, applications & future prospects. *Adv. Colloid Interface Sci.* **2012**, *170*, 2–27.
43. Yu, H.-D.; Regulacio, M.D.; Ye, E.; Han, M.-Y. Chemical routes to top-down nanofabrication. *Chem. Soc. Rev.* **2013**, *42*, 6006–6018.
44. Hasan, R.M.M.; Luo, X. Promising lithography techniques for next-generation logic devices. *Nanomanufacturing and Metrology* **2018**, *1*, 67–81.
45. Amadi, E.V.; Venkataraman, A.; Papadopoulos, C. Nanoscale self-assembly: concepts, applications and challenges. *Nanotechnology*. **2021**, *33*, 132001.
46. Fatahilah, M.F.; Yu, F.; Strempel, K.; Römer, F.; Maradan, D.; Meneghini, M.; Bakin, A.; Hohls, F.; Schumacher, H.W.; Witzigmann, B.; et al. Top-down GaN nanowire transistors with nearly zero gate hysteresis for parallel vertical electronics, *Sci. Rep.* **2019**, *9*, 1–11.
47. Pease, R.F.; Chou, S.Y. Lithography and other patterning techniques for future electronics. *Proc. IEEE* **2008**, *96*, 248–270.
48. Baláž, P. Mechanochemistry in Minerals Engineering," in *Mechanochemistry in nanoscience and minerals engineering*; Springer. **2008,** pp. 257–296.
49. Thakur Prasad Yadav, D.P.S. Ram Manohar Yadav Mechanical Milling: a Top Down Approach for the Synthesis of Nanomaterials and Nanocomposites. *Nanoscience and Nanotechnology* **2012**, *2*, 22–48.
50. Benjamin, J.S. Mechanicalalloying—A Perspective. *Met. Powder Rep.* **1990**, *45*, 122–127.
51. Gezerman, A.; Corbacioglu, B.D. Use of uniform-sized balls to improve the manufacturing of $CaCO_3$ in ball mills. *Int J Modern Chem* **2012**, *1*, 116–124.
52. Mikó, T.; Kristaly, F.; Bohács, K.; Sveda, M.; Sycheva, A.; Janovszky, D. The effect of process control agents and milling atmosphere on the structural changes of $Ti_{50}Cu_{27,5}Ni_{10}Zr_{10}Co_{2,5}$ master alloy during short time milling. *In Proceedings of the IOP*

Conference Series: Materials Science and Engineering; IOP Publishing. **2018**, Vol. 426, p. 012035.

53. Gaffet, E.; Le Caër, G. Mechanical processing for nanomaterials. In *Encyclopedia of nanoscience and nanotechnology*; American Scientific Publishers Stevenson Ranch, calif, USA, 2004; Vol. 5, pp. 91–129.
54. Sherif, E.-E.M.; Sumiyama, K.; Aoki, K.; Masumoto, T.; Suzuki, K. Mechanism of solid-gas reaction for formation of metastable niobium-nitride alloy powders by reactive ball milling. *J. Mater. Res.* **1994**, *9*, 2891–2898.
55. Glushenkov, A.; Zhang, H.-Z.; Zou, J.; Lu, G.; Chen, Y. Efficient production of ZnO nanowires by a ball milling and annealing method. *Nanotechnology* **2007**, *18*, 175604.

56. Sharma, S.; Pande, S.S.; Swaminathan, P. Top-down synthesis of zinc oxide based inks for inkjet printing. *RSC Adv.* **2017**, *7*, 39411–39419.
57. Zhang, D. Processing of advanced materials using high-energy mechanical milling. *Prog. Mater Sci.* **2004**, *49*, 537–560.
58. Gorrasi, G.; Sorrentino, A. Mechanical milling as a technology to produce structural and functional bio-nanocomposites. *Green Chem.* **2015**, *17*, 2610–2625.
59. Suryanarayana, C.; Ivanov, E.; Boldyrev, V.. The science and technology of mechanical alloying. *Mater. Sci. Eng., A* **2001**, *304-306*, 151–158.
60. Sapkota, R.; Zou, J.; Dawka, S.; Bobak, J.E.; Papadopoulos, C. Multi-functional thin film coatings formed via nanogrinding. *Appl. Nanoscience* **2018**, *8*, 1437–1444.
61. Ricardo, C.A.; Su'ait, M.; Müller, M.; Scardi, P. Production of Cu_2(Zn, Fe)SnS_4 powders for thin film solar cell by high energy ball milling. *J. Power Sources* **2013**, *230*, 70–75.
62. Hassoun, J.; Mulas, G.; Panero, S.; Scrosati, B. Ternary Sn–Co–C Li-ion battery electrode material prepared by high energy ball milling. *Electrochem. Commun.* **2007**, *9*, 2075–2081.
63. Shao, H.; Felderhoff, M.; Schüth, F. Hydrogen storage properties of nanostructured MgH_2/TiH_2 composite prepared by ball milling under high hydrogen pressure. *Int. J. Hydrogen Energy* **2011**, *36*, 10828–10833.
64. Liu, C.P.; Chuang, C.L. Fabrication of CIGS nanoparticle-ink using ball milling technology for applied in CIGS thin films solar cell. *Powder Technol.* **2012**, *229*, 78–83.
65. Tao, T.; Rahman, M.; Ramireddy, T.; Sunarso, J.; Chen, Y.; Glushenkov, A. Preparation of composite electrodes with carbon nanotubes for lithium-ion batteries by low-energy ball milling. *RSC Adv.* **2014**, *4*, 36649–36655.
66. Pradeep, T.; Sandhyarani, N. Structure and dynamics of monolayers on planar and cluster surfaces. *Pure Appl. Chem.* **2002**, *74*, 1593–1607.
67. Srisombat, L.; Jamison, A.C.; Lee, T.R. Stability: A Key issue for self-assembled monolayers on gold as thin-film coatings and nanoparticle protectants. *Colloids Surf, A.* **2011**, *390*, 1–19.
68. Heiligtag, F.J.; Niederberger, M. The fascinating world of nanoparticle research. *Mater. Today* **2013**, *16*, 262–271.

69. Talapin, D.V.; Shevchenko, E.V. Introduction: nanoparticle chemistry, **2016.**
70. Sharma, N.; Ojha, H.; Bharadwaj, A.; Pathak, D.P.; Sharma, R.K. Preparation and catalytic applications of nanomaterials: a review. *RSC Adv.* **2015**, *5*, 53381–53403.
71. Chaturvedi, S.; Dave, P.N.; Shah, N. Applications of nano-catalyst in new era. *J. Saudi Chem.Soc.* **2012**, *16*, 307–325
72. Kolahalam, L.A.; Viswanath], I.V. [Kasi; Diwakar, B.S.; Govindh, B.; Reddy, V.; Murthy, Y.L.N. Review on nanomaterials: Synthesis and applications. *Mater. Today:. Proc.* **2019**, *18*, 2182–2190,
73. Kabir, R.; Saifullah, M.; Khalid, A.; Ahmed, A.Z.; Masum, S.M.; Molla, M.; Islam, A. Synthesis of N-Doped ZnO Nanocomposites for Sunlight Photocatalytic Degradation of Textile Dye Pollutants. *J. Compos.Sci* **2020**, *4*, 49.
74. Gouma, P.; Gouma, P.-I. *Nanomaterials for chemical sensors and biotechnology*.; Pan Stanford Publishing, **2010**;
75. Ridha, N.J.; Alosfur, F.K.M.; Jumali, M.H.H.; Radiman, S. Dimensional effect of ZnO nanorods gas sensing performance. *J. Phys. D: Appl. Phys.* **2018**, *51*, 435101.
76. Nazemi, H.; Joseph, A.; Park, J.; Emadi, A. Advanced micro-and nano-gas sensor technology: A review, *Sensors* **2019**, *19*, 1285.
77. Available online: *www.fisinc.co.jp/en/common/pdf/SB11A00E_P.pdf.(Accessed 4th Jan.2021)*
78. Cheng, I.-C.; Wagner, S. Overview of Flexible Electronics Technology. in *Flexible Electronics: Materials and Applications*; Springer US: Boston, MA, **2009**; pp. 1–28.
79. Chae, S.H.; Lee, Y.H. Carbon nanotubes and graphene towards soft electronics. *Nano Convergence* **2014**, *1*, 15.
80. Guo, C.F.; Ren, Z. Flexible transparent conductors based on metal nanowire networks. *Mater. Today* **2015**, *18*, 143–154,
81. Zhang, Z.; Lv, R.; Jia, Y.; Gan, X.; Zhu, H.; Kang, F. All-Carbon Electrodes for Flexible Solar Cells. *Appl. Sci.* **2018**, *8*,
82. Nazar, Lf.; Goward, G.; Leroux, F.; Duncan, M.; Huang, H.; Kerr, T.; Gaubicher, J. Nanostructured materials for energy storage. *Int. J. Inorg. Mater.* **2001**, *3*, 191–200.
83. Winter, M.; Brodd, R.J. What Are Batteries, Fuel Cells, and Supercapacitors?, *Chem. Rev.* **2004**, *104*, 4245–4270,
84. Santhosh, C.; Velmurugan, V.; Jacob, G.; Jeong, S.K.; Grace, A.N.; Bhatnagar, A. Role of nanomaterials in water treatment applications: a review. *Chem. Eng* **2016**, *306*, 1116–1137.
85. Madima, N.; Mishra, S.; Inamuddin, I.; Mishra, A. Carbon-based nanomaterials for remediation of organic and inorganic pollutants from wastewater.A Review. *Environ. Chem. Lett.* **2020**, 1–23.
86. Kolodziejczyk, B. Nanotechnology, nanowaste and their effect on ecosystems: A need for efficient monitoring, disposal and recycling, *Brief for GSDR 2016*.” **2016**

87. Al-Ruqeishi, M.S.; Mohiuddin, T.; Al-Habsi, B.; Al-Ruqeishi, F.; Al-Fahdi, A.; Al-Khusaibi, A. Piezoelectric nanogenerator based on ZnO nanorods. *Arab.J. Chem.* **2019**, *12*, 5173–5179.
88. Tan, Y.; Kamiya, T.; Durrani, Z.; Ahmed, H. Room temperature nanocrystalline silicon Single-electron Transistors. *J. Appl. Phys.* **2003**, *94*, 633–637.
89. Zhuang, L.; Guo, L.; Chou, S.Y. Silicon single-electron quantum-dot transistor switch operating at room temperature. *Appl. Phys. Lett.* **1998**, *72*, 1205–1207.
90. Huan, C.; Shu-Qing, S. Silicon nanoparticles: Preparation,properties, and applications. *Chin. Phys. B* **2014**, *23*, 088102.
91. Chen, S.; Shen, Z.; See, A.; Chan, L. E Enhancement effect of C40 $TiSi_2$ on the C54 phase formation. *J. Electrochem. Soc.* **2001**, *148*, G734.
92. Mann, R.; Clevenger, L. The C49 to C54 phase transformation in $TiSi_2$ thin films. *J. Electrochem. Soc.* **1994**, *141*, 1347.
93. Dan-Feng, L.; Chang-Zhi, G.; Cai-Xin, G.; Shuang-Lin, Y.; Chang-Wen, H. Low resistivity C54 phase $TiSi_2$ films synthesized by a novel two-step method. *Chin. Phys. Lett.* **2003**, *20*, 1329.
94. Meinardi, F.; Quilici, S.; Borghesi, A.; Artioli, G. Microstructure imaging of C54–$TiSi_2$ polycrystalline thin films by micro Raman spectroscopy. *Appl. Phys. Lett.* **1999**, *75*, 3090–3092
95. Salah, N.; Habib, S.S.; Khan, Z.H.; Memic, A.; Azam, A.; Alarfaj, E.; Zahed, N.; Al-Hamedi, S. High-energy ball milling technique for ZnO nanoparticles as antibacterial material. *Int. J. Nanomed.* **2011**, *6*, 863.
96. Lin, Y.-H.; Faber, H.; Zhao, K.; Wang, Q.; Amassian, A.; McLachlan, M.; Anthopoulos, T.D. High performance ZnO transistors processed via an aqueous carbon-free metal oxide precursor route at emperatures 80–180 ^{0}C. *Adv. Mater.* **2013**, *25*, 4340–4346.
97. Liu, D.; Lv, Y.; Zhang, M.; Liu, Y.; Zhu, Y.; Zong, R.; Zhu, Y. Defect-related photoluminescence and photocatalytic properties of porous ZnO nanosheets. *J. Mater. Chem.A* **2014**, *2*, 15377–15388.
98. Chen, K.-J.; Hung, F.-Y.; Chang, S.-J.; Young, S.-J. Optoelectronic characteristics of UV photodetector based on ZnO nanowire thin films. *J. Alloys Compd.* **2009**, *479*, 674–677.
99. Biswas, C.; Ma, Z.; Zhu, X.; Kawaharamura, T.; Wang, K.L. Atmospheric growth of hybrid ZnO thin films for inverted polymer solar cells. *Sol. Energy Mater. Sol. Cells* **2016**, *157*, 1048–1056.
100. Mao, Y.Z.; Ma, S.Y.; Li, W.Q.; Luo, J.; Cheng, L.; Gengzang, D.J.; Xu, X.L. Synthesis of porous small-sized ZnO nanoparticles and their gas-sensing performance. *Mater. Lett.* **2015**, *157*, 151–154.
101. Dawka, S. Nano-grinding zinc oxide for electronic applications. Master's thesis report, University of Victoria, 2019.
102. Cai, X. Photocatalytic Degradation of Industrial Dye Using Catalysts Synthesized Via Nanogrinding. Master's thesis report, University of Victoria, 2020.

103. Duan, P. Thin Film Gas Sensors Based on Zinc Oxide Nanoinks. Master's thesis report, University of Victoria, 2021.

104. Auslender, M.; Hava, S. Single-Crystal Silicon: Electrical and Optical Properties. in *Springer Handbook of Electronic and Photonic Materials*; Kasap, S., Capper, P., Eds.; Springer International Publishing: Cham, 2017; pp. 1–1.

105. Beyers, R.; Sinclair, R. Metastable phase formation in titanium-silicon thin films. *J. Appl. Phys.* **1985**, *57*, 5240–5245. Duan, P. Thin Film Gas Sensors Based on Zinc Oxide Nanoinks. Master's thesis report, University of Victoria, 2021.

106. Matsubara, Y.; Horiuchi, T.; Okumura, K. Activation energy for the C49-to-C54 phase transition of polycrystalline $TiSi_2$ films with arsenic impurities *Appl. Phys. Lett.* **1993**, *62*, 2634–2636.

107. Ma, Z.; Allen, L. Kinetic mechanisms of the C49-to-C54 polymorphic transformation in titanium disilicide thin films: A microstructure-scaled nucleation-mode transition. *Phys. Rev. B* **1994**, *49*, 13501.

108. Rosenkranz, R.; Frommeyer, G. Microstructures and properties of the refractory compounds $TiSi_2$ and $ZrSi_2$. *Zeitschrift für Metallkunde* **1992**, *83*, 685–689.

109. Iannuzzi, M.; Raiteri, P.; Miglio, L. Self-diffusion of silicon in $TiSi_2$ competing phases by tight-binding molecular dynamics. *Comput. Mater.* **2001**, *20*, 394–400.

110. Medeiros-Ribeiro, G.; Ohlberg, D.; Bowler, D.; Tanner, R.; Briggs, G.; Williams, R.S. TiKamiium disilicide nanostructures: two phases and their surfacess. *Surf. Sci.* **1999**, *431*, 116–127.

111. Villars, P.; Calvert, L. Pearson’s Handbook of Crystallographic Data for Intermediate Phases. *American Society of Metals, Cleveland, OH* **1985**.

112. Iannuzzi, M.; Miglio, L.; Celino, M. Structural and thermoelastic properties of crystalline and amorphous $TiSi_2$ phases by tight-binding molecular dynamics. *Phys. Rev. B* **2000**, *61*, 14405.

113. Chou, T.; Wong, C.; Tu, K.-N. Lattice imaging of metastable $TiSi_2$. *J. Appl. Phys.* **1987**, *62*, 2275–2279

114. Ryu, Y.; Lee, T.-S.; Lubguban, J.A.; White, H.W.; Kim, B.-J.; Park, Y.-S.; Youn, C.-J. Next generation of oxide photonic devices: ZnO-based ultraviolet light emitting diodes. *Appl. Phys. Lett.* **2006**, *88*, 241108,

115. Look, D.C. Recent advances in ZnO materials and devices. *Mater. Sci. Eng., B* **2001**, *80*, 383–387.

116. Wang, X.; Summers, C.J.; Wang, Z.L. Large-Scale Hexagonal-Patterned Growth of Aligned ZnO Nanorods for Nano-optoelectronics and Nanosensor Arrays. *Nano Lett.* **2004**, *4*, 423–426,

117. Özgür, Ü.; Alivov, Y.I.; Liu, C.; Teke, A.; Reshchikov, Ma.; Dogan, S.; Avrutin, V.; Cho, S.-J.; Morkoç; H A comprehensive review of ZnO materials and devices. *J. Appl. Phys.* **2005**, *98*, 11.

118. Zinc oxide nanostructures: growth, properties and applications. *J. Phys.: Condens. Matter* **2004**, *16*, R829.
119. Reynolds, D.C.; Look, D.C.; Jogai, B. Optically pumped ultraviolet lasing from ZnO. *Solid State Commun.* **1996**, *99*, 873–875.
120. Vogel, D.; Krüger, P.; Pollmann, J. Ab initio electronic-structure calculations for II-VI semiconductors using self-interaction-corrected pseudopotentials. *Physical Review B* **1995**, *52*, R14316. Wang, Z.L.
121. Burmeister, C.F.; Kwade, A. Process engineering with planetary ball mills. *Chem. Soc. Rev.* **2013**, *42*, 7660–7667.
122. Fokina, E.; Budim, N.; Kochnev, V.; Chernik, G. Planetary mills of periodic and continuous action. *J. Mater. Sci.* **2004**, *39*, 5217–5221.
123. Mio, H.; Kano, J.; Saito, F.; Kaneko, K. Effects of rotational direction and rotation-to-revolution speed ratio in planetary ball milling. *Mater. Sci. Eng., A* **2002**, *332*, 75–80.
124. Takehira, K.; Shishido, T. Preparation of supported metal catalysts starting from hydrotalcites as the precursors and their improvements by adopting "memory effect. *Catal. Surv. Asia* **2007**, *11*, 1–30.
125. Szuppa, T.; Stolle, A.; Ondruschka, B.; Hopfe, W. Solvent-free dehydrogenation of γ-terpinene in a ball mill: investigation of reaction parameters. *Green Chem.* **2010**, *12*, 1288–1294.
126. Takacs, L.; McHenry, J. Temperature of the milling balls in shaker and planetary mills. *J. Mater. Sci.* **2006**, *41*, 5246–5249.
127. Balema, V.P.; Wiench, J.W.; Pruski, M.; Pecharsky, V.K. Solvent-free mechanochemical synthesis of phosphonium salts. *Chem. Commun.* **2002**, 724–725.
128. Acar, I.; Acisli, O. Mechano-chemical surface modification of calcite by wet-stirred ball milling. *Appl. Surf. Sci.* **2018**, *457*, 208–213.
129. Sato, A.; Kano, J.; Saito, F. Analysis of abrasion mechanism of grinding media in a planetary mill with DEM simulation. *Adv. Powder Technol.* **2010**, *21*, 212–216.
130. Kalantar-zadeh, K.; Fry, B. *Nanotechnology-enabled sensors*; Springer Science & Business Media, **2007**.
131. Zhang, J.; Jung, Y.-G. *Advanced ceramic and metallic coating and thin film materials for energy and environmental applications*.; Springer, **2018**;
132. Frederichi, D.; Scaliante, M.H.N.O.; Bergamasco, R. Structured photocatalytic systems: photocatalytic coatings on low-cost structures for treatment of water contaminated with micropollutants—a short review. *Environ. Sci. Pollut. Research* **2021**, *28*, 23610–23633.
133. Lamour, G.; Hamraoui, A.; Buvailo, A.; Xing, Y.; Keuleyan, S.; Prakash, V.; Eftekhari-Bafrooei, A.; Borguet, E. Contact angle measurements using a simplified experimental setup. *J. Chem. Educ.* **2010**, *87*, 1403–1407.
134. Wenzel, R.N. Surface roughness and contact angle. *J. Phys. Chem* **1949**, *53*, 1466–1467.
135. Cassie, A.; Baxter, S. Wettability of porous surfaces. *Trans. Faraday Soc.* **1944**, *40*, 546–551.

136. Roach, P.; Shirtcliffe, N.J.; Newton, M.I. Progess in superhydrophobic surface development. *Soft Matter* **2008**, *4*, 224–240.

137. Ramasamy, S.; Purniah, B. Electrical properties of nanostructured materials. *Proceedings-Indian National Science Academy Part A* **2001**, *67*, 85–102.

138. Stegner, A.; Pereira, R.; Klein, K.; Lechner, R.; Dietmueller, R.; Brandt, M.; Stutzmann, M.; Wiggers, H. Electronic transport in phosphorus-doped silicon nanocrystal networks. *Phys. Rev. Lett.* **2008**, *100*, 026803.

139. Zou, C.; Zhang, X.; Jing, G.; Zhang, J.; Liao, Z.; Yu, D. Synthesis and electrical properties of $TiSi_2$ nanocables. *Appl. Phys. Lett.* **2008**, *92*, 253102.

140. Schmitt, A.L.; Zhu, L.; Schmeiβer, D.; Himpsel, F.J.; Jin, S. Metallic single-crystal CoSi nanowires via chemical vapor deposition of single-source precursor. *J. Phys. Chem. B* **2006**, *110*, 18142–18146.

141. Smith, M.A.; Holihan, E.; Duncan, B.P.; McRae, J.C.; Miller, P.; Stull, C.; Pinelli, G.; Yost, D.-R.W.; Racz, L.M. A Low-Temperature Nickel Silicide Process for Wafer Bonding and High-Density Interconnects. *IEEE Trans. Compon. Packag. Manuf. Technol.* **2020**, *10*, 908–916.

142. Patel, H.K. *The electronic nose: artificial olfaction technology y*; Springer, **2014**;

143. Bhattacharyya, P.; Basu, P.K.; Basu, S. Methane detection by MIM sensor devices based on nano ZnO thin films obtained by sol-gel and by anodization: a comparative study. in *Proceedings of the 2010 First International Conference on Sensor Device Technologies and Applications*; IEEE, **2010**; pp. 110–115.

144. Bochenkov, V.; Sergeev, G.; others Sensitivity, selectivity, and stability of gas-sensitive metal-oxide nanostructures," *Metal oxide nanostructures and their applications*, **2010**, *3*, 31–52.

145. Vander Wal, R.L.; Hunter, G.; Xu, J.; Kulis, M.; Berger, G.; Ticich, T. Metal-oxide nanostructure and gas-sensing performance. *Sens. Actuators, B* **2009**, *138*, 113–119.

146. Mirzaei, A.; Kim, J.-H.; Kim, H.W.; Kim, S.S. How shell thickness can affect the gas sensing properties of nanostructured materials: Survey of literature. *Sens. Actuators, B* **2018**, *258*, 270–294,

147. Sun, Y.-F.; Liu, S.-B.; Meng, F.-L.; Liu, J.-Y.; Jin, Z.; Kong, L.-T.; Liu, J.-H. Metal Oxide Nanostructures and Their Gas Sensing Properties: A Review. *Sensors* **2012**, *12*, 2610–2631,

148. Dey, A. Semiconductor metal oxide gas sensors: A review,. *Mater. Sci. Eng., B,* **2018**, *229*, 206–217

149. Barsan, N.; Koziej, D.; Weimar, U. Metal oxide-based gas sensor research: How to?, *Sens. Actuators, B* **2007**, *121*, 18–35.

150. Tiburcio-Silver, A.; Sánchez-Juárez, A. SnO_2:Ga thin films as oxygen gas sensor. *Mater. Sci. Eng., B* **2004**, *110*, 268–271.

151. Gupta, S.; Joshi, A.; Kaur, M. Development of gas sensors using ZnO nanostructures. *J. Chem. Sci.* **2010**, *122*, 57–62.

152. Choi, J.D.; Choi, G.M. Electrical and CO gas sensing properties of layered ZnO–CuO sensor. *Sens. Actuators, B* **2000**, *69*, 120–126,

153. Zhu, L.; Zeng, W. Room-temperature gas sensing of ZnO-based gas sensor: A review. *Sens. Actuators, A* **2017**, *267*, 242–261.

154. Wang, C.; Yin, L.; Zhang, L.; Xiang, D.; Gao, R. Metal oxide gas sensors: sensitivity and influencing factors. *Sensors* **2010**, *10*, 2088–2106.

155. Jiménez-Cadena, G.; Riu, J.; Rius, F.X. Gas sensors based on nanostructured materials. *Analyst* **2007**, *132*, 1083–1099,

156. Kumar, R.; Al-Dossary, O.; Kumar, G.; Umar, A. inc oxide nanostructures for NO_2 gas–sensor applications: A review. *Nanomicro Lett.* **2015**, *7*, 97–120.

157. Yuan, Z.; Li, R.; Meng, F.; Zhang, J.; Zuo, K.; Han, E. Approaches to enhancing gas sensing properties: A review. *Sensors* **2019**, *19*, 1495.

158. Galstyan, V.; Comini, E.; Baratto, C.; Faglia, G.; Sberveglieri, G. Nanostructured ZnO chemical gas sensors. *Ceram. Int.* **2015**, *41*, 14239–14244.

159. Khatibani, A.B. Investigation of gas sensing property of zinc oxide thin films deposited by Sol-Gel method: effects of molarity and annealing temperature. *Indian J. Phys.* **2021**, *95*, 243–252.

160. Mao, S.; Lu, G.; Chen, J. Nanocarbon-based gas sensors: progress and challenges. *J. Mater. Chem.A* **2014**, *2*, 5573–5579.

161. Onkar, S.; Nagdeote, S.; Wadatkar, A.; Kharat, P.B. Gas sensing behavior of ZnO thick film sensor towards H_2S, NH_3, LPG and CO_2. in *Proceedings of the Journal of Physics: Conference Series*; IOP Publishing, **2020**; Vol. 1644, p. 012060.

162. Arshak, K.; Gaidan, I. Development of a novel gas sensor based on oxide thick films. *Mater. Sci. Eng. B.* **2005**, *118*, 44–49.

163. Arafat, M.; Dinan, B.; Akbar, S.A.; Haseeb, A. Gas sensors based on one dimensional nanostructured metal-oxides: a review. *Sensors* **2012**, *12*, 7207–7258.

164. Guo, W.; Liu, T.; Zeng, W.; Liu, D.; Chen, Y.; Wang, Z. Gas-sensing property improvement of ZnO by hierarchical flower-like architectures. *Mater. Lett.* **2011**, *65*, 3384–3387.

165. Choi, J.-H.; Kim, H.; Sung, H.-K.; Cha, H.-Y. Investigation of stability and power consumption of an AlGaN/GaN heterostructure hydrogen gas sensor using different bias conditions. *Sensors* **2019**, *19*, 5549.

166. Vollath, D. *Nanomaterials: an introduction to synthesis, properties and applications*; Second;2nd; ed.; Wiley-VCH Verlag GmbH & Co. KGaA: Weinheim, Germany, **2013**;

167. Yin, X.M.; Li, C.C.; Zhang, M.; Hao, Q.Y.; Liu, S.; Li, Q.H.; Chen, L.B.; Wang, T.H. SnO_2 monolayer porous hollow spheres as a gas sensor. *Nanotechnology* **2009**, *20*, 455503.

168. Li, Z.; Liu, X.; Zhou, M.; Zhang, S.; Cao, S.; Lei, G.; Lou, C.; Zhang, J. Plasma-induced oxygen vacancies enabled ultrathin ZnO films for highly sensitive detection of triethylamine. *J. Hazard. Mater.* **2021**, *415*, 125757

169. Li, S.; Wu, J.; Wang, Z.M.; Jiang, Y. *Nanoscale Sensors*; Lecture Notes in Nanoscale Science and Technology; Springer International Publishing, **2014**.

170. Hjiri, M.; Bahanan, F.; Aida, M.; El Mir, L.; Neri, G. High performance CO gas sensor based on ZnO nanoparticles. *J. Inorg. Organomet. Polym. Mater.* **2020**, *30*, 4063–4071.

171. Erol, A.; Okur, S.; Comba, B.; Mermer, Ö.; Arıkan, M.Ç. Humidity sensing properties of ZnO nanoparticles synthesized by sol–gel process. *Sens. Actuators, B,* **2010**, *145*, 174–180.

172. Demontis, V.; Rocci, M.; Donarelli, M.; Maiti, R.; Zannier, V.; Beltram, F.; Sorba, L.; Roddaro, S.; Rossella, F.; Baratto, C. Conductometric sensing with individual InAs nanowires. *Sensors* **2019**, *19*, 2994.

173. Chougule, M.; Sen, S.; Patil, V. Fabrication of nanostructured ZnO thin film sensor for NO_2 monitoring. *Ceram. Int.* **2012**, *38*, 2685–2692.

174. Shrivastava, A.; Gupta, V.B.; and others Methods for the determination of limit of detection and limit of quantitation of the analytical methods. *Chronicles of young scientists* **2011**, *2*, 21–25.

175. Goebel, D.M.; Katz, I. *Fundamentals of electric propulsion: ion and Hall thrusters*; John Wiley & Sons, **2008**; Vol. 1;

176. Šćepanović, M.; Grujić-Brojčin, M.; Vojisavljević, K.; Bernik, S.; Srećković, T. Raman study of structural disorder in ZnO nanopowders. *J. Raman Spectrosc.* **2010**, *41*, 914–921,

177. Cuscó, R.; Alarcón-Lladó, E.; Ibáñez, J.; Artús, L.; Jiménez, J.; Wang, B.; Callahan, M.J. Temperature dependence of Raman scattering in ZnO. *Phys. Rev. B* **2007**, *75*, 165202,

178. Damen, T.C.; Porto, S.P.S.; Tell, B. Raman Effect in Zinc Oxide. *Phys. Rev.* **1966**, *142*, 570–574,

179. Russo, V.; Ghidelli, M.; Gondoni, P.; Casari, C.S.; Li Bassi, A. Multi-wavelength Raman scattering of nanostructured Al-doped zinc oxide. *J. Appl. Phys.* **2014**, *115,* 073508.

180. Kahouli, M.; Barhoumi, A.; Bouzid, A.; Al-Hajry, A.; Guermazi, S. Structural and optical properties of ZnO nanoparticles prepared by direct precipitation method. *Superlattices Microstruct.* **2015**, *85,* 7–23.

181. Mishra, Y.K.; Murugan, N.A.; Kotakoski, J.; Adam, J. Progress in electronics and photonics nanomaterials; *Elsevier,* **2017**.

182. Sato, K.; Ono, K.; Izuishi, T.; Kuwahara, S.; Katayama, K.; Toyoda, T.; Hayase, S.; Shen, Q. The effect of CdS on the charge separation and recombination dynamics in PbS/CdS double-layered quantum dot sensitized solar cells. *Chem. Phys.* **2016**, *478*, 159–163.

183. Chen, S.; Thind, S.S.; Chen, A. Nanostructured materials for water splitting-state of the art and future needs: A mini-review. *Electrochem. Commun.* **2016**, *63*, 10–17.

184. Ganesh, V.A.; Raut, H.K.; Nair, A.S.; Ramakrishna, S. A review on self-cleaning coatings. *J. Mater. Chem.* **2011**, *21*, 16304–16322.

185. He, L.; Tjong, S.C. Nanostructured transparent conductive films: Fabrication, characterization and applications. *Mater. Sci. Eng. R Rep* **2016**, *109*, 1–101.

186. Papadopoulos, C. Nanofabrication principles and applications*; Springer,* **2016**;

187. David, K.; Ragauskas, A.J. Switchgrass as an energy crop for biofuel production: a review of its ligno-cellulosic chemical properties. *Energy Environ. Sci.* **2010**, *3*, 1182–1190
188. He, T.; Li, J.; Wang, L.; Zhu, J.; Jiang, W. Preparation and consolidation of alumina/graphene composite powders. *Mater. Trans.* **2009**, *50*, 749–751.
189. Junghanns, J.-U.A.; Müller, R.H. Nanocrystal technology, drug delivery and clinical applications. *Int. J. Nanomed.* **2008**, *3*, 295.
190. Loh, Z.H.; Samanta, A.K.; Heng, P.W.S. Overview of milling techniques for improving the solubility of poorly water-soluble drugs. *Asian J. Pharm. Sci.* **2015**, *10*, 255–274.
191. Porwal, H.; Grasso, S.; Reece, M. Review of graphene–ceramic matrix composites. *Adv. Appl. Ceram.* **2013**, *112*, 443–454.
192. Ranu, B.; Stolle, A.; Cravotto, G.; Juaristi, E.; Su, W.; Lamaty, F.; Friscic, T.; Mack, J.; Takahiro, H.; Kraus, G.; et al. *Ball milling towards green synthesis: applications, projects, challenges*; Royal Society of Chemistry, **2014**;
193. Tadier, S.; Bolay, N.L.; Rey, C.; Combes, C. Co-grinding significance for calcium carbonate–calcium phosphate mixed cement. Part I: Effect of particle size and mixing on solid phase reactivity. *Acta Biomater.* **2011**, *7*, 1817–1826,
194. Tsai, W.-T. Microstructural characterization of calcite-based powder materials prepared by planetary ball milling. *Materials* **2013**, *6*, 3361–3372.
195. Montero, M.; Emura, M.; Cebollada, F.; González, J.; González, E.; Vicent, J. Coercivity analysis in the $C_{ox}/(SiO_2)$ 100- x nanoparticulate system. *J. Magn. Magn. Mater.* **1999**, *203*, 205–207.
196. Lam, C.; Zhang, Y.; Tang, Y.; Lee, C.; Bello, I.; Lee, S. Large-scale synthesis of ultrafine Si nanoparticles by ball milling. *J. Cryst. Growth* **2000**, *220*, 466–470.
197. Imamura, H.; Tanaka, K.; Kitazawa, I.; Sumi, T.; Sakata, Y.; Nakayama, N.; Ooshima, S. Hydrogen storage properties of nanocrystalline MgH_2 and MgH_2/Sn nanocomposite synthesized by ball milling. *J. Alloys Compd.* **2009**, *484*, 939–942.
198. Zhao, W.; Fang, M.; Wu, F.; Wu, H.; Wang, L.; Chen, G. Preparation of graphene by exfoliation of graphite using wet ball milling. *J. Mater. Chem.* **2010**, *20*, 5817–5819.
199. Ichimura, K.; Aoki, K.; Akiyama, H.; Horiuchi, S.; Nagano, S.; Horie, S. Properties of core–shell structured nanopowders of molecular crystals fabricated by dry grinding. *J. Mater. Chem.* **2010**, *20*, 4312–4320.
200. Cetinkaya, T.; Guler, M.; Akbulut, H. Enhancing electrochemical performance of silicon anodes by dispersing MWCNTs using planetary ball milling. *Microelectron. Eng.* **2013**, *108*, 169–176.
201. Ni, D.; Shen, H.; Li, H.; Ma, Y.; Zhai, T. Synthesis of high efficient Cu/TiO_2 photocatalysts by grinding and their size-dependent photocatalytic hydrogen production. *Appl. Surf. Sci.* **2017**, *409*, 241–249.
202. Ralphs, K.; Hardacre, C.; James, S.L. Application of heterogeneous catalysts prepared by mechanochemical synthesis. *Chem. Soc. Rev.* **2013**, *42*, 7701–7718.

203. Ibrahem, M.A.; Wei, H.-Y.; Tsai, M.-H.; Ho, K.-C.; Shyue, J.-J.; Chu, C.W. Solution-processed zinc oxide nanoparticles as interlayer materials for inverted organic solar cells. *Sol. Energy Mater. Sol. Cells* **2013**, *108*, 156–163.
204. Naghdi, M.; Taheran, M.; Brar, S.K.; Rouissi, T.; Verma, M.; Surampalli, R.Y.; Valero, J.R. A green method for production of nanobiochar by ball milling-optimization and characterization. *J. Cleaner Prod.* **2017**, *164*, 1394–1405.
205. Chen, X.; Zhang, C.; Kato, T.; Yang, X.; Wu, S.; Wang, R.; Nosaka, M.; Luo, J. Evolution of tribo-induced interfacial nanostructures governing superlubricity in aC: H and aC: H: Si films. *Nat. Commun.* **2017**, *8*, 1–13.
206. Bor, A.; Ichinkhorloo, B.; Uyanga, B.; Lee, J.; Choi, H. Cu/CNT nanocomposite fabrication with different raw material properties using a planetary ball milling process. *Powder Technol.* **2018**, *323*, 563–573.
207. Wang, B.; Wei, S.; Wang, Y.; Liang, Y.; Guo, L.; Xue, J.; Pan, F.; Tang, A.; Chen, X.; Xu, B. Effect of milling time on microstructure and properties of Nano-titanium polymer by high-energy ball milling, *Appl. Surf. Sci.* **2018**, *434*, 1248–1256.
208. Rasband, W.S.; and others, ImageJ. U.S. National Institutes of Health, Bethesda, Maryland, USA 1997-2016.
209. Verdoni, L.; Fink, M.; Mitchell, B. A A fractionation process of mechanochemically synthesized blue-green luminescent alkyl-passivated silicon nanoparticles. *Chem. Eng. Technol.* **2011**, *172*, 591–600.
210. Hallmann, S.; Fink, M.J.; Mitchell, B.S. Wetting properties of silicon films from alkyl-passivated particles produced by mechanochemical synthesis. *J. Colloid Interface Sci.* **2010**, *348*, 634–641.
211. Kang, I.-C.; Zhang, Q.; Yin, S.; Sato, T.; Saito, F. Novel method for preparation of high visible active N-doped TiO_2 photocatalyst with its grinding in solvent. *Appl. Catal., B* **2008**, *84*, 570–576.
212. Sandwick, T.; Rajan, K. The oxidation of titanium silicide. *J. Electron. Mater.* **1990**, *19*, 1193–1199.
213. Hedborg, E.; Winquist, F.; Sundgren, H.; Lundström, I. Charge migration on hydrophobic and hydrophilic silicon dioxide. *Thin Solid Films* **1999**, *340*, 250–256.
214. Milne, A.; Amirfazli, A. The Cassie equation: How it is meant to be used. *Adv. Colloid Interface Sci.* **2012**, *170*, 48–55.
215. Mitchell, S.; Davidson, M.; Emmison, N.; Bradley, R. Isopropyl alcohol plasma modification of polystyrene surfaces to Influencece cell attachment behaviour. *Surf. Sci.* **2004**, *561*, 110–120.
216. Tadanaga, K.; Morinaga, J.; Minami, T. Formation of superhydrophobic-superhydrophilic pattern on flowerlike alumina thin film by the sol-gel method. *J. Sol-Gel Sci. Technol.* **2000**, *19*, 211–214.
217. Drelich, J.; Chibowski, E.; Meng, D.D.; Terpilowski, K. Hydrophilic and superhydrophilic surfaces and materials,. *Soft Matter* **2011**, *7*, 9804–9828.

218. Azizian-Kalandaragh, Y.; Nouhi, S.; Amiri, M. Effect of post-annealing treatment on the wetting, optical and structural properties of Ag/Indium tin oxide thin films prepared by electron beam evaporation technique. *Mater. Express* **2015**, *5*, 137–145.
219. Sun, S.; Lee, C.; Chou, H.; Huang, J. Effects of Ag addition on phase transformation and resistivity of $TiSi_2$ thin films. *Appl. Surf. Sci.* **2011**, *257*, 2550–2554.
220. Goyal, A.; Demmenie, M.; Huang, C.-C.; Schall, P.; Dohnalova, K. Photophysical properties of ball milled silicon nanostructures. *Faraday Discuss.* **2020**, *222*, 96–107.
221. Mozaffari, S.; Li, W.; Thompson, C.; Ivanov, S.; Seifert, S.; Lee, B.; Kovarik, L.; Karim, A.M. Colloidal nanoparticle size control: experimental and kinetic modeling investigation of the ligand–metal binding role in controlling the nucleation and growth kinetics. *Nanoscale* **2017**, *9*, 13772–13785.
222. Mozaffari, S.; Tchoukov, P.; Mozaffari, A.; Atias, J.; Czarnecki, J.; Nazemifard, N. Capillary driven flow in nanochannels–Application to heavy oil rheology studies. *Colloids Surf., A* **2017**, *513*, 178–187.
223. Xu, Z.; Li, Y.; Zhang, B.; Purkait, T.; Alb, A.; Mitchell, B.S.; Grayson, S.M.; Fink, M.J. Water-soluble PEGylated silicon nanoparticles and their assembly into swellable nanoparticle aggregates. *J. Nanopart. Res.* **2015**, *17*, 56.
224. Pattekari, P.; Zheng, Z.; Zhang, X.; Levchenko, T.; Torchilin, V.; Lvov, Y. T Top-down and bottom-up approaches in production of aqueous nanocolloids of low solubility drug paclitaxel. *Phys. Chem. Chem. Phys.* **2011**, *13*, 9014–9019.
225. Zheng, Z.; Zhang, X.; Carbo, D.; Clark, C.; Nathan, C.-A.; Lvov, Y. Sonication-assisted synthesis of polyelectrolyte-coated curcumin nanoparticles. *Langmuir* **2010**, *26*, 7679–7681.
226. Lvov, Y.M.; Pattekari, P.; Zhang, X.; Torchilin, V. Converting poorly soluble materials into stable aqueous nanocolloids. *Langmuir* **2011**, *27*, 1212–1217.
227. Fernando, R.H. Nanocomposite and Nanostructured Coatings: Recent Advancements, in *Nanotechnology Applications in Coatings*; **2009**; pp. 2–21.
228. Levashov, E.A.; Shtansky, D.V. Multifunctional nanostructured films. *Russ. Chem. Rev.* **2007**, *76*, 463–470,
229. Kumar, R.; Kumar, G.; Al-Dossary, O.; Umar, ZnO nanostructured thin films: Depositions, properties and applications—A review. *Mater. Express.* **2015**, *5*, 3–23.
230. Rao, T.P.; Santhoshkumar, M.C. Effect of thickness on structural, optical and electrical properties of nanostructured ZnO thin films by spray pyrolysis. *Appl. Surf. Sci.* **2009**, *255*, 4579–4584,
231. Mao, S.; Cui, S.; Yu, K.; Wen, Z.; Lu, G.; Chen, J. Ultrafast hydrogen sensing through hybrids of semiconducting single-walled carbon nanotubes and tin oxide nanocrystals. *Nanoscale* **2012**, *4*, 1275–1279.
232. Ali, S.; Gupta, A.; Shafiei, M.; Langford, S.J. Recent Advances in Perylene Diimide-Based Active Materials in Electrical Mode Gas Sensing. *Chemosensors* **2021**, *9*, 30.

233. Ali, S.; Jameel, M.A.; Gupta, A.; Langford, S.J.; Shafiei, M. Capacitive humidity sensing performance of naphthalene diimide derivatives at ambient temperature. *Synth. Met.* **2021**, *275*, 116739.

234. Kong, J.; Franklin, N.R.; Zhou, C.; Chapline, M.G.; Peng, S.; Cho, K.; Dai, H. Nanotube Molecular Wires as Chemical Sensors. *Science* **2000**, *287*, 622–625.

235. Huang, X.-J.; Choi, Y.-K. Chemical sensors based on nanostructured materials. *Sens. Actuators, B* **2007**, *122*, 659–671.

236. Eranna, G.; Joshi, B.C.; Runthala, D.P.; Gupta, R.P. Oxide Materials for Development of Integrated Gas Sensors—A Comprehensive Review. *Crit. Rev. Solid State Mater. Sci.* **2004**, *29*, 111–188.

237. Cerjak, H. Nanomaterials: an introduction to synthesis, properties and applications. *Mater. Technol.* **2009**, *24*, 74–74.

238. Koo, W.-T.; Cho, H.-J.; Kim, D.-H.; Kim, Y.H.; Shin, H.; Penner, R.M.; Kim, I.-D. Chemiresistive hydrogen sensors: fundamentals, recent advances, and challenges. *ACS Nano* **2020**, *14*, 14284–14322.

239. Hastir, A.; Kohli, N.; Singh, R.C. Ag Doped ZnO Nanowires as Highly Sensitive Ethanol Gas Sensor. *Mater. Today:. Proc.* **2017**, *4*, 9476–9480.

240. Majhi, S.M.; Rai, P.; Yu, Y.-T. Facile Approach to Synthesize Au@ZnO Core–Shell Nanoparticles and Their Application for Highly Sensitive and Selective Gas Sensors. *ACS Appl. Mater. Interfaces* **2015**, *7*, 9462–9468.

241. Guo, J.; Zhang, J.; Zhu, M.; Ju, D.; Xu, H.; Cao, B. High-performance gas sensor based on ZnO nanowires functionalized by Au nanoparticles. *Sens. Actuators, B* **2014**, *199*, 339–345.

242. Lu, H.F.; Li, F.; Liu, G.; Chen, Z.-G.; Wang, D.-W.; Fang, H.-T.; Lu, G.Q.; Jiang, Z.H.; Cheng, H.-M. Amorphous TiO_2 nanotube arrays for low-temperature oxygen sensors. *Nanotechnology* **2008**, *19*, 405504.

243. Chaabouni, F.; Abaab, M.; Rezig, B. Metrological characteristics of ZnO oxygen sensor at room temperature. *Sens. Actuators, B* **2004**, *100*, 200–204.

244. Khosravi, Y.; Sasar, M.; Abdi, Y. Light-induced oxygen sensing using ZnO/GO based gas sensor. *Mater. Sci. Semicond. Process.* **2018**, *85*, 9–14.

245. Mukae, K.; Tsuda, K.; Nagasawa, I. Capacitance-vs-voltage characteristics of ZnO varistors. *J. Appl. Phys.* **1979**, *50*, 4475–4476.

246. Dongale, T.D.; Khot, K.V.; Mali, S.S.; Patil, P.S.; Gaikwad, P.K.; Kamat, R.K.; Bhosale, P.N. Development of Ag/ZnO/FTO thin film memristor using aqueous chemical route. *Mater. Sci. Semicond. Process.* **2015**, *40*, 523–526.

247. Choi, M.-Y.; Choi, D.; Jin, M.-J.; Kim, I.; Kim, S.-H.; Choi, J.-Y.; Lee, S.Y.; Kim, J.M.; Kim, S.-W. Mechanically Powered Transparent Flexible Charge-Generating Nanodevices with Piezoelectric ZnO Nanorods. *Adv. Mater.* **2009**, *21*, 2185–2189.

248. Liewhiran, C.; Phanichphant, S. Doctor-bladed thick films of flame-made Pd/ZnO nanoparticles for ethanol sensing. *Curr. Appl Phys.* **2008**, *8*, 336–339

249. Koshizaki, N.; Oyama, T. Sensing characteristics of ZnO-based NOx sensor. *Sens. Actuators, B* **2000**, *66*, 119–121.
250. Khan, S.B.; Faisal, M.; Rahman, M.M.; Jamal, A. Low-temperature growth of ZnO nanoparticles: Photocatalyst and acetone sensor. *Talanta* **2011**, *85*, 943–949.
251. Wagh, M.S.; Jain, G.H.; Patil, D.R.; Patil, S.A.; Patil, L.A. Modified zinc oxide thick film resistors as NH_3 gas sensor. *Sens. Actuators, B* **2006**, *115*, 128–133.
252. Ryu, H.-W.; Park, B.-S.; Akbar, S.A.; Lee, W.-S.; Hong, K.-J.; Seo, Y.-J.; Shin, D.-C.; Park, J.-S.; Choi, G.-P. ZnO sol–gel derived porous film for CO gas sensing. *Sens. Actuators, B* **2003**, *96*, 717–722.
253. Li, B.S.; Liu, Y.C.; Chu, Z.S.; Shen, D.Z.; Lu, Y.M.; Zhang, J.Y.; Fan, X.W. High quality ZnO thin films grown by plasma enhanced chemical vapor deposition. *J. Appl. Phys.* **2002**, *91*, 501–505.
254. Lou, C.; Wang, K.; Mei, H.; Xie, J.; Zheng, W.; Liu, X.; Zhang, J. ZnO nanoarrays via a thermal decomposition–deposition method for sensitive and selective NO_2 detection. *Cryst.Eng.Comm* **2021**, *23*, 3654–3663.
255. Xu, Y.; Zheng, W.; Liu, X.; Zhang, L.; Zheng, L.; Yang, C.; Pinna, N.; Zhang, J. Platinum single atoms on tin oxide ultrathin films for extremely sensitive gas detection. *Mater. Horiz.* **2020**, *7*, 1519–1527
256. Stambolova, I.; Konstantinov, K.; Vassilev, S.; Peshev, P.; Tsacheva, T. Lanthanum doped SnO_2 and ZnO thin films sensitive to ethanol and humidity. *Mater. Chem. Phys.* **2000**, *63*, 104–108.
257. Ohshima, T.; Thareja, R.K.; Yamagata, Y.; Ikegami, T.; Ebihara, K.; Narayan, J. Laser-ablated plasma for deposition of ZnO thin films on various substrates. *Sci. Technol. Adv. Mater.* **2001**, *2*, 517–523.
258. Omerovic, N.; Radovic, M.; Savic, S.M.; Katona, J. Preparation of TiO_2 and ZnO dispersions for inkjet printing of flexible sensing devices. *Process. Appl. Ceram* **2018**, *12*, 326–334.
259. Liu, H.-Y.; Kong, H.; Ma, X.-M.; Shi, W.-Z. Microstructure and electrical properties of ZnO-based varistors prepared by high-energy ball milling. *J. Mater. Sci.* **2007**, *42*, 2637–2642.
260. Takehana, M.; Nishino, T.; Sugawara, K.; Sugawara, T. Preparation of zinc oxide varistor by a wet chemical method. *Mater. Sci. Eng., B*, **1996**, *41*, 186–189.
261. Qi, Q.; Zhang, T.; Yu, Q.; Wang, R.; Zeng, Y.; Liu, L.; Yang, H. Properties of humidity sensing ZnO nanorods-base sensor fabricated by screen-printing. *Sens. Actuators, B* **2008**, *133*, 638–643,
262. Wang, C.-T.; Huang, K.-Y.; Lin, D.T.; Liao, W.-C.; Lin, H.-W.; Hu, Y.-C. A flexible proximity sensor fully fabricated by inkjet printing. *Sensors* **2010**, *10*, 5054–5062.
263. Deng, Y.; Peng, E.; Shao, Y.; Xiao, Z.; Dong, Q.; Huang, J. Scalable fabrication of efficient organolead trihalide perovskite solar cells with doctor-bladed active layers. *Energy Environ. Sci.* **2015**, *8*, 1544–1550,

264. Giri, P.; Bhattacharyya, S.; Singh, D.K.; Kesavamoorthy, R.; Panigrahi, B.; Nair, K. Correlation between microstructure and optical properties of ZnO nanoparticles synthesized by ball milling. *J. Appl. Phys.* **2007**, *102*, 093515.

265. Bruckmann, A.; Krebs, A.; Bolm, C. Organocatalytic reactions: effects of ball milling, microwave and ultrasound irradiation. *Green Chem.* **2008**, *10*, 1131–1141.

266. Mio, H.; Kano, J.; Saito, F. Scale-up method of planetary ball mill. *Chem. Eng. Sci.* **2004**, *59*, 5909–5916,

267. Baláž, P.; Achimovičová, M.; Baláž, M.; Billik, P.; Cherkezova-Zheleva, Z.; Criado, J.M.; Delogu, F.; Dutková, E.; Gaffet, E.; Gotor, F.J.; et al. Hallmarks of mechanochemistry: from nanoparticles to technology. *Chem. Soc. Rev.* **2013**, *42*, 7571–7637,

268. Huang, L.; Kramer, G.; Wieldraaijer, W.; Brands, D.; Poels, E.; Castricum, H.; Bakker, H. Methanol synthesis over Cu/ZnO catalysts prepared by ball milling. *Catal. Lett.* **1997**, *48*, 55–59.

269. Yong, H.E.; Krishnamoorthy, K.; Hyun, K.T.; Kim, S.J. Preparation of ZnO nanopaint for marine antifouling applications. *J. Ind. Eng. Chem.* **2015**, *29*, 39–42.

270. Yu, M.; Shao, D.; Lu, F.; Sun, X.; Sun, H.; Hu, T.; Wang, G.; Sawyer, S.; Qiu, H.; Lian, J. ZnO/graphene nanocomposite fabricated by high energy ball milling with greatly enhanced lithium storage capability. *Electrochem. Commun.* **2013**, *34*, 312–315,

271. Radoi, R.; ndez, P.F.; Piqueras, J.; Wiggins, M.S.; Solis, J. Luminescence properties of mechanically milled and laser irradiated ZnO. *Nanotechnology* **2003**, *14*, 794–798.

272. Xie, C.; Xiao, L.; Hu, M.; Bai, Z.; Xia, X.; Zeng, D. Fabrication and formaldehyde gas-sensing property of ZnO–MnO_2 coplanar gas sensor arrays. *Sens. Actuators, B* **2010**, *145*, 457–463.

273. Chen, H.; Liu, Y.; Xie, C.; Wu, J.; Zeng, D.; Liao, Y. A comparative study on UV light activated porous TiO_2 and ZnO film sensors for gas sensing at room temperature. *Ceram. Int.* **2012**, *38*, 503–509

274. Yu, J.H.; Choi, G.M. Selective CO gas detection of CuO- and ZnO-doped SnO_2 gas sensor. *Sens. Actuators, B* **2001**, *75*, 56–61.

275. Xiang, X.; Zhu, D.; Wang, D. Enhanced formaldehyde gas sensing properties of La-doped SnO 2 nanoparticles prepared by ball-milling solid chemical reaction method. *J. Mater. Sci.: Mater. Electron.* **2016**, *27*, 7425–7432.

276. Hu, Y.; Tan, O.K.; Cao, W.; Zhu, W. A low temperature nano-structured $SrTiO_3$ thick film oxygen gas sensor. *Ceram. Int.* **2004**, *30*, 1819–1822.

277. Wagh, M..; Patil, L..; Seth, T.; Amalnerkar, D.. Surface cupricated SnO_2–ZnO thick films as a H_2S gas sensor. *Mater. Chem. Phys.* **2004**, *84*, 228–233.

278. Chang, S.-P.; Chen, K.-J. Zinc oxide nanoparticle photodetector. *J.Nanomater.* **2012**, *2012*, 1.

279. Gimenez, A.J.; Yáñez-Limón, J.M.; Seminario, J.M. ZnO–cellulose composite for UV sensing. *IEEE Sens. J.* **2012**, *13*, 1301–1306.

280. Hsiao, Y.-J.; Fang, T.-H.; Ji, L.-W.; Yang, B.-Y. Red-shift effect and sensitive responsivity of MoS_2/ZnO flexible photodetectors. *Nanoscale Res. Lett.* **2015**, *10*, 1–5.
281. Kumar, M.; Singh, B.; Yadav, P.; Bhatt, V.; Kumar, M.; Singh, K.; Abhyankar, A.; Kumar, A.; Yun, J.-H. Effect of structural defects, surface roughness on sensing properties of Al doped ZnO thin films deposited by chemical spray pyrolysis technique. *Ceram. Int.* **2017**, *43*, 3562–3568.

282. Rambu, A.; Ursu, L.; Iftimie, N.; Nica, V.; Dobromir, M.; Iacomi, F. Study on Ni-doped ZnO films as gas sensors. *Appl. Surf. Sci.* **2013**, *280*, 598–604.
283. Fang, Z.; Yan, Z.; Tan, Y.; Liu, X.; Wang, Y. Influence of post-annealing treatment on the structure properties of ZnO films. *Appl. Surf. Sci.* **2005**, *241*, 303–308.
284. Saikia, L.; Bhuyan, D.; Saikia, M.; Malakar, B.; Dutta, D.K.; Sengupta, P. Photocatalytic performance of ZnO nanomaterials for self sensitized degradation of malachite green dye under solar light. *Appl Catal A: Gen.* **2015**, *490*, 42–49.
285. Amutha, A.; Amirthapandian, S.; Sundaravel, B.; Panigrahi, B.K.; Saravanan, K.; Thangadurai, P. Low-temperature photoluminescence behaviour of Ag decorated ZnO Nanorods. *J. Appl. Phys* **2016**, *120*, 205104
286. Zhang, W.C.; Wu, X.L.; Chen, H.T.; Zhu, J.; Huang, G.S. Excitation wavelength dependence of the visible photoluminescence from amorphous ZnO granular films. *J. Appl. Phys.* **2008**, *103*, 093718,.
287. Choi, Y.I.; Jung, H.J.; Shin, W.G.; Sohn, Y. Band gap-engineered ZnO and Ag/ZnO by ball-milling method and their photocatalytic and Fenton-like photocatalytic activities. *Appl. Surf. Sci.* **2015**, *356*, 615–625.
288. Vojisavljevic, K.; Šcepanovic, M.; Sreckovic, T.; Grujic-Brojcin, M.; Brankovic, Z.; Brankovic, G. Structural characterization of mechanically milled ZnO: influence of zirconia milling media. *J. Phys.: Condens. Matter* **2008**, *20*, 475202,
289. Singh, J.; Sharma, S.; Soni, S.; Sharma, S.; Singh, R.C. Influence of different milling media on structural, morphological and optical properties of the ZnO nanoparticles synthesized by ball milling process. *Mater. Sci. Semicond. Process.* **2019**, *98*, 29–38.
290. Jung, H.J.; Sohn, Y.; Sung, H.G.; Hyun, H.S.; Shin, W.G. Physicochemical properties of ball milled boron particles: dry vs. wet ball milling process. *Powder Technol.* **2015**, *269*, 548–553.
291. Qiao, X.; Xu, Y.; Yang, K.; Ma, J.; Li, C.; Wang, H.; Jia, L. Mo doped $BiVO_4$ gas sensor with high sensitivity and selectivity towards H_2S. *Chem. Eng. J.* **2020**, *395*, 125144.
292. Chen, Y.; Li, X.; Li, X.; Wang, J.; Tang, Z. UV activated hollow ZnO microspheres for selective ethanol sensors at low temperatures. *Sens. Actuators, B* **2016**, *232*, 158–164.
293. Ahn, M.-W.; Park, K.-S.; Heo, J.-H.; Park, J.-G.; Kim, D.-W.; Choi, K.J.; Lee, J.-H.; Hong, S.-H. Gas sensing properties of defect-controlled ZnO-nanowire gas sensor. *Appl. Phys. Lett.* **2008**, *93*, 263103,

294. Yu, L.; Guo, F.; Liu, S.; Yang, B.; Jiang, Y.; Qi, L.; Fan, X. Both oxygen vacancies defects and porosity facilitated NO_2 gas sensing response in 2D ZnO nanowalls at room temperature. *J. Alloys Compd.* **2016**, *682*, 352–356.
295. Abe, S.; Choi, U.-S.; Shimanoe, K.; Yamazoe, N. Influences of ball-milling time on gas-sensing properties of Co_3O_4–SnO_2 composites. *Sens. Actuators, B* **2005**, *107*, 516–522.
296. Viswanathan, R.; Gupta, R.B. Formation of zinc oxide nanoparticles in supercritical water. *The J. Supercrit Fluids* **2003**, *27*, 187–193.
297. Matsoukas, T.; Friedlander, S.K. Dynamics of aerosol agglomerate formation. *J. Colloid Interface Sci.* **1991**, *146*, 495–506.
298. Medina, J.; Bolaños, H.; Mosquera-Sanchez, L.P.; Rodriguez-Paez, J. Controlled synthesis of ZnO nanoparticles and evaluation of their toxicity in Mus musculus mice. *Int. Nano Lett.* **2018**, *8*, 165–179.
299. Göpel, W.; Lampe, U. Influence of defects on the electronic structure of zinc oxide surfaces. *Phys. Rev. B* **1980**, *22*, 6447–6462.
300. Aggelopoulos, C.A.; Dimitropoulos, M.; Govatsi, A.; Sygellou, L.; Tsakiroglou, C.D.; Yannopoulos, S.N. Influence of the surface-to-bulk defects ratio of ZnO and TiO_2 on their UV-mediated photocatalytic activity. *Appl. Catal., B* **2017**, *205*, 292–301.
301. Tsukazaki, A.; Ohtomo, A.; Kawasaki, M. High-mobility electronic transport in ZnO thin films. *Appl. Phys. Lett.* **2006**, *88*, 152106.
302. Xuan, J.; Zhao, G.; Sun, M.; Jia, F.; Wang, X.; Zhou, T.; Yin, G.; Liu, B. Low-temperature operating ZnO-based NO_2 sensors: a review. *RSC Adv.* **2020**, *10*, 39786–39807,
303. Yan, D.; Hu, M.; Li, S.; Liang, J.; Wu, Y.; Ma, S. Electrochemical deposition of ZnO nanostructures onto porous silicon and their enhanced gas sensing to NO_2 at room temperature. *Electrochim. Acta* **2014**, *115*, 297–305.,
304. Liang, Y.-C.; Lee, C.-M.; Lo, Y.-J. Reducing gas-sensing performance of Ce-doped SnO_2 thin films through a cosputtering method. *RSC Adv.* **2017**, *7*, 4724–4734.
305. Keskinen, H.; Tricoli, A.; Marjamäki, M.; Mäkelä, J.M.; Pratsinis, S.E. Size-selected agglomerates of SnO_2 nanoparticles as gas sensors. *J. Appl. Phys.* **2009**, *106*, 084316.
306. Tiemann, M. Porous metal oxides as gas sensors. *Chem.–Eur. J.* **2007**, *13*, 8376–8388.
307. Hong, R.; Pan, T.; Qian, J.; Li, H. Synthesis and surface modification of ZnO nanoparticles. *Chem. Eng. J.* **2006**, *119*, 71–81.
308. Ozcan, S.; Can, M.M.; Ceylan, A. Single step synthesis of nanocrystalline ZnO via wet-milling. *Mater. Lett.* **2010**, *64*, 2447–2449.
309. Faure, B.; Salazar-Alvarez, G.; Ahniyaz, A.; Villaluenga, I.; Berriozabal, G.; Miguel, Y.R.D.; Bergström, L. Dispersion and surface functionalization of oxide nanoparticles for transparent photocatalytic and UV-protecting coatings and sunscreens. *Sci. Technol. Adv. Mater.* **2013**, *14*, 023001.
310. Wang, X.; Yee, S.S.; Carey, W.P. Transition between neck-controlled and grain-boundary-controlled sensitivity of metal-oxide gas sensors. *Sens. Actuators, B* **1995**, *25*, 454–457.

311. Jacobs, C.B.; Maksov, A.B.; Muckley, E.S.; Collins, L.; Mahjouri-Samani, M.; Ievlev, A.; Rouleau, C.M.; Moon, J.-W.; Graham, D.E.; Sumpter, B.G.; et al. UV-activated ZnO films on a flexible substrate for room temperature O_2 and H_2O sensing. *Sci. Rep.* **2017**, *7*, 6053.
312. Lee, J.-H.; Kim, J.-Y.; Mirzaei, A.; Kim, H.; Kim, S. Significant enhancement of hydrogen-sensing properties of ZnO nanofibers through NiO loading. *Nanomaterials* **2018**, *8*, 902.
313. Takahashi, Y.; Kanamori, M.; Kondoh, A.; Minoura, H.; Ohya, Y. Photoconductivity of Ultrathin Zinc Oxide Films. *Jpn. J. Appl. Phys.* **1994**, *33*, 6611–6615.
314. Scolfaro, D.; Onofre, Y.; Teodoro, M.D.; Godoy, M. de Atmosphere-Dependent Photoconductivity of ZnO in the Urbach Tail. *Int. J. Photoenergy* **2018**, *2018*.
315. Kulwicki, B.M. Humidity Sensors. *J. Am. Ceram. Soc.* **1991**, *74*, 697–708.
316. Chen, Z.; Lu, C. Humidity sensors: a review of materials and mechanisms. *Sens. Lett.* **2005**, *3*, 274–295.
317. Gupta, S.P.; Pawbake, A.S.; Sathe, B.R.; Late, D.J.; Walke, P.S. S Superior humidity sensor and photodetector of mesoporous ZnO nanosheets at room temperature. *Sens. Actuators, B* **2019**, *293*, 83–92.
318. Jiao, M.; Van Duy, N.; Hoa, N.D.; Van Hieu, N.; Hjort, K.; Nguyen, H.; others Comparison of NO_2 gas-sensing properties of three different ZnO nanostructures synthesized by On-Chip low-temperature hydrothermal growth. *J. Electron. Mater.* **2018**, *47*, 785–793.
319. Karthik, T.; Maldonado, A.; Olvera, M. de la L. Manufacturing of Tin Oxide Pellets and their application for CO and C_3H_8 Gas Sensors. *in Proceedings of the 2013 10th International Conference on Electrical Engineering, Computing Science and Automatic Control (CCE)*; IEEE, 2013; pp. 402–406.
320. Moon, W.J.; Yu, J.H.; Choi, G.M. The CO and H_2 gas selectivity of CuO-doped SnO_2–ZnO composite gas sensor. *Sens. Actuators, B* **2002**, *87*, 464–470.
321. Huang, B.-R.; Lin, J.-C. A facile synthesis of ZnO nanotubes and their hydrogen sensing properties. *Appl. Surf. Sci.* **2013**, *280*, 945–949.
322. Yoon, D.H.; Yu, J.H.; Choi, G.M. CO gas sensing properties of ZnO–CuO composite. *Sens. Actuators, B: Chemical* **1998**, *46*, 15–23.
323. Phan, D.-T.; Chung, G.-S. Effects of different morphologies of ZnO films on hydrogen sensing properties. *J. Electroceramics* **2014**, *32*, 353–360.
324. Khan, R.; Ra, H.-W.; Kim, J.T.; Jang, W.S.; Sharma, D.; Im, Y.H. Nanojunction effects in multiple ZnO nanowire gas sensor. *Sens. Actuators, B* **2010**, *150*, 389–393.
325. Parellada-Monreal, L.; Mandayo, G.; Martın-Mayor, A.; Souto-Canteli, I.; Bou-Ali, M.M. Influence of the test-chamber shape on the performance of the conductometric gas sensors. *Sens. Actuators, B* **2022**, *361*, 131694.
326. Annanouch, F.-E.; Bouchet, G.; Perrier, P.; Morati, N.; Reynard-Carette, C.; Aguir, K.; Bendahan, M. How the chamber design can affect gas sensor responses. *In Proceedings of the MDPI*; **2018**; Vol. 2, p. 820.
327. Ritterskamp, P.; Kuklya, A.; Wuestkamp, M.-A.; Kerpen, K.; Weidenthaler, C.; Demuth, M. A titanium disilicide derived semiconducting catalyst for water splitting under solar

radiation—reversible storage of oxygen and hydrogen. *Angew. Chem. Int. Ed.* **2007**, *46*, 7770–7774.

328. Maeda, K.; Domen, K. Photocatalytic water splitting: recent progress and future challenges,. *The J. Phys. Chem. Lett.* **2010**, *1*, 2655–2661.
329. Flores, N.M.; Pal, U.; Galeazzi, R.; Sandoval, A. Effects of morphology, surface area, and defect content on the photocatalytic dye degradation performance of ZnO nanostructures. *RSC Adv.* **2014**, *4*, 41099–41110.
330. Spencer, M.J.; Wong, K.W.; Yarovsky, I. Density functional theory modelling of ZnO (101 0) and ZnO (21 1 0) surfaces: Structure, properties and adsorption of N_2O. *Mater. Chem. Phys.* **2010**, *119*, 505–514.
331. Nzabahimana, J.; Chang, P.; Hu, X. Porous carbon-coated ball-milled silicon as high-performance anodes for lithium-ion batteries. *J.Mater Sci*, **2019**, *54*, 4798–4810.
332. Ammar, S.; Ramesh, K.; Vengadaesvaran, B.; Ramesh, S.; Arof, A.K. Formulation and characterization of hybrid polymeric/ZnO nanocomposite coatings with remarkable anti-corrosion and hydrophobic characteristics. *J. Coat. Technol. Res.* **2016**, *13*, 921–930.